論文 / 著書情報
Article / Book Information

題目(和文)	SeaQuestスペクトロメータにおけるミューオン対のトラッキング方法の開発
Title(English)	Developments of Tracking Methods of Muon Pairs with SeaQuest Spectrometer
著者(和文)	ｻﾞﾝﾌﾄｭﾙﾌﾛﾘｱﾝ
Author(English)	Florian Sanftl
出典(和文)	学位:博士(理学), 学位授与機関:東京工業大学, 報告番号:甲第9375号, 授与年月日:2014年3月26日, 学位の種別:課程博士, 審査員:柴田　利明,旭　耕一郎,中村　隆司,久世　正弘,陣内　修
Citation(English)	Degree:Doctor (Science), Conferring organization: Tokyo Institute of Technology, Report number:甲第9375号, Conferred date:2014/3/26, Degree Type:Course doctor, Examiner:,,,,
学位種別(和文)	博士論文
Type(English)	Doctoral Thesis

Developments of Tracking Methods of Muon Pairs with SeaQuest Spectrometer

Florian Sanftl

Thesis submitted to the Department of Physics in partial fulfillment of the requirements for the degree of Doctor of Science at Tokyo Institute of Technology

February, 2014

”Non quia difficilia sunt non audemus,
sed quia non audemus difficilia sunt.”
L.A. Seneca

Abstract

The SeaQuest experiment is a fixed-target experiment located at Fermi Nation Accelerator Laboratory (Fermilab). It detects Drell-Yan muon pairs from proton-proton collisions induced by a 120 GeV beam ($\sqrt{s} = 11$ GeV). A new method which allows the track reconstruction of dimuons in high multiplicity data recorded during the first commissioning run at the SeaQuest experiment is presented in this thesis.

The SeaQuest spectrometer is a forward spectrometer optimized by a focusing magnet to be particularly sensitive to high-p_T muon pairs. A large iron block is placed inside the focusing magnet to stop hadronic background. Four tracking stations are used for track reconstruction. The first three stations consist of drift chambers, and the fourth station consists of drift tubes. Hodoscope arrays in each tracking station trigger dimuon events. A separate analyzing magnet measures the momenta of muons.

The Drell-Yan process occurs in high-energetic hadron collisions when a quark of one hadron and an antiquark of another hadron annihilate, creating a virtual photon, which then decays into a pair of oppositely charged muons. The dimuon kinematics are directly related to the antiquarks in the proton.

In spring 2012, the first 120 GeV proton beam was successfully extracted from the Fermilab Main Injector Ring to the fixed target beamline of SeaQuest. The average intensity of the protons during the 6 weeks of commissioning run was 7×10^{11} per spill.

This thesis reports developments of analysis methods for the dimuon track reconstruction based on data from the commissioning run. The track reconstruction at SeaQuest consists of two steps: the 'track finding' which combines hits in the different drift chambers to a track candidate, and the 'track fitting' which determines the momentum of a muon track based on the known map of the magnetic field of the spectrometer.

The duty factor of the delivered beam during the commissioning run was unstable and it caused large multiplicities. The average occupancies of the drift chambers were between 30% and 60% in each tracking station per event. In order to deal with these high occupancies, an innovative track finder algorithm was developed. It is capable of quickly correlating dimuon hits in the first three tracking stations and building track candidates with an efficiency above 98%. The drift chamber occupancies could be reduced to 10% by only considering drift chamber hits which can successfully be associated to muon track candidates.

The algorithm significantly improved the absolute yield of reconstructed dimuons.

It is shown that the track finder algorithm increased the yield of measured J/Ψs by a factor of 2.4, compared to the case without this track finder. The reconstructed J/Ψ-mass was $M(J/\psi) = (2.938 \pm 0.020)\,\mathrm{GeV/c^2}$, its width was $\sigma(J/\psi) = (0.205 \pm 0.019)\,\mathrm{GeV/c^2}$. These values gave an important information on the performance of the SeaQuest spectrometer.

Contents

List of Figures

List of Tables

Chapter 1

Introduction

Since the beginning of atomic physics, scattering experiments have proven to be a powerful tool to probe the inner structure of matter. Among the best examples is the discovery of the atomic nucleus, achieved in 1909 by Rutherford, Geiger and Marsden by scattering α particles off a gold foil. The increased performances of the particle accelerators over the past decades enabled to dramatically increase the energy of the projectiles and thus their spatial resolution. As a result the nucleon and its substructures were eventually resolved adopting a similar approach, though with an enormously greater experimental complexity.

By the end of the 60's, the first inclusive Deep Inelastic Scattering (DIS) $e+p \rightarrow e'+X$ experiments at SLAC showed that the structure functions of the nucleons were to a large extent independent on the squared momentum transfer Q^2. This scaling behaviour of the structure functions was eventually interpreted by Bjorken and Feynman as the evidence of the existence of point-like sub-nucleonic particles, called partons [1, 2, 3]. These objects were later identified with the quarks, spin 1/2 particles with fractional electric charge and a new degree of freedom called flavour, whose existence had been predicted by Gell-Mann and Zweig on the basis of the symmetry properties of the meson and baryon multiplets in 1964 [4]. The Quark Parton Model, developed in the late 60's, has proven to be particularly successful in the prediction of a number of "macroscopic" observables of the hadrons such as the mass, the charge and the spin. According to this model, the proton is made of three quarks, each carrying approximately a third of the proton mass. Two quarks have flavour up and charge $+\frac{2}{3}e$ and one has flavour down and charge $-\frac{1}{3}e$, thus resulting in a total charge $+e$ (i.e. the same of the electron but with opposite sign). Furthermore, in a proton with spin along a certain direction, two of the quarks have spin in the same direction and one in the opposite direction, thus resulting in a total

spin equal to 1/2.

Though this model represented a major step toward the understanding of the inner structure of the nucleon, it was soon found to be not enough appropriate for a comprehensive interpretation of the experimental data. Indeed, experimental results showed that only roughly 50% of the nucleon's momentum is carried by quarks. The missing momentum could only be explained a few years later within the framework of the quantum chromodynamics (QCD), the gauge theory of strong interactions. According to this theory, which requires the existence of the colour as an additional degree of freedom of the quarks, the missing momentum of the nucleon is carried by the gluons, the gauge bosons of the strong interaction. These particles do not show up in the electro-weak scattering processes as they carry no electro-weak charge. The first evidence for the existence of gluons was the observation of three-jet events at the electron-positron collider PETRA at DESY in 1979 [5].

In order to provide alternative ways to probe the inner structure of hadrons, investigation of lepton-pair production in hadronic interactions were intensified and began with an experiment carried out at Brookhaven National Laboratory in 1970 [6, 7]. This experiment studied the reaction $p+U \rightarrow \mu^+ + \mu^- + X$ for proton energies between 22 GeV and 29 GeV, resulting in pair masses between 1 GeV/c^2 and 6.7 GeV/c^2. The data above ≈ 3 GeV/c^2 (where the J/ψ resonance family would later be found) exhibited a rapidly decreasing continuum of muon pairs. The steeply falling nature of the cross section was explained later that year by Drell and Yan [8], who were interested in dilepton production as a possible application of the quark-parton model of hadron structure outside of deeply-inelastic scattering experiments. Their model of quark-antiquark annihilation through the electromagnetic interaction, which has become known as the Drell-Yan process, was generally successful in describing the data and would only improve as our understanding of the strong interaction improved.

The Drell-Yan process still remains an active area of experimental and theoretical research some forty years later. It has played a key role in developing the mathematical technology of perturbative Quantum Chromodynamics (QCD), being one of the first processes to be calculated to next-to-leading order $O(\alpha_s)$, and remains one of the few processes to be calculated to next-to-next-to-leading $O(\alpha_s^2)$. Experimentally it has provided a wealth of information about nucleon structure; its confirmation of the quark-parton model and its verification of the quark charge assignments being two notable early applications. The number of colors was also validated.

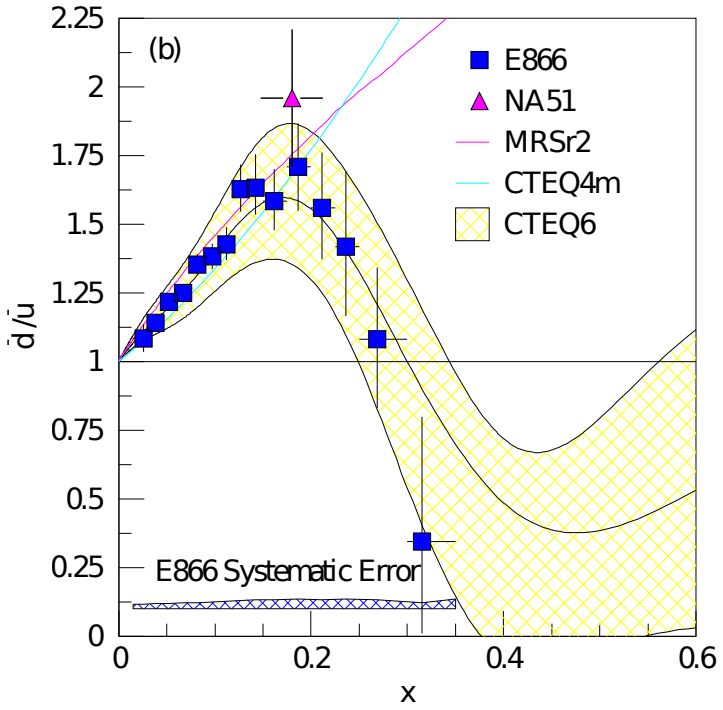

Figure 1.1: The blue squares show the $\bar{d}(x)/\bar{u}(x)$ ratio extracted by E866/NuSea [9]. The magenta triangle is the NA51 [10] measurement of $\bar{d}/\bar{u}$. The central curve in the cross filled band shows the $\bar{d}/\bar{u}$ ratio from the CTEQ6m fit [11], which included the E866/NuSea data, and the band represents the uncertainty from the fit. The curves labeled CTEQ4M [12] and MRS(r2) [13] show the parameterizations of $\bar{d}(x)/\bar{u}(x)$ which included the NA51 point and the NMC integral but not the E866/NuSea data.

One out of several complications in hadronic interactions is that we cannot be certain which of the partons (the quark, antiquark and gluon constituents) in the hadron are participating in the interaction. We can however determine the probability of finding a given parton carrying a fraction x (called Bjoerken-x) of the interacting hadron's momentum, which we in general denote by $f_{q/A}(x)$ for a parton of type q in a hadron of type A. Calculations of various physical processes in the Standard Model thus depend on prior knowledge of these parton distribution functions (PDF's).

While proton structure functions have been measured with deep inelastic scattering over five orders of magnitude in both the fractional momentum of the parton, x, and the virtuality of the incident photon, Q^2, the factorizable, non-perturbative parton distributions must be determined by phenomenological fits [11, 14, 15, 16]. Perturbative Quantum Chromodynamics (QCD) quantitatively describes the Q^2 evolution of the parton distributions, but the origins of the parton distributions themselves have not proved amenable to QCD treatment, although many models exist in the lit-

erature. Measurements of those distributions provide vital information on nucleon structure which is used to constrain and refine the phenomenology.

In many cases new data have tested underlying assumptions of the phenomenology, the phenomenology had to be modified. For example, no known symmetry requires the equality of the anti-down $\bar{d}_p(x)$ and anti-up $\bar{u}_p(x)$ quark distributions in the proton. Until 1991, this equality was a common assumption. The first evidence to the contrary was the NMC observation [17, 18] that the integral of $\bar{d}(x) - \bar{u}(x)$ is non-zero. NA51 [10] used the Drell-Yan process to confirm the inequality of $\bar{d}(x)$ and $\bar{u}(x)$. Fermilab E866/NuSea [19, 9] measured the x dependence of $\bar{d}(x)/\bar{u}(x)$ and $\bar{d}(x) - \bar{u}(x)$ from $0.015 < x < 0.35$. The sea and valence distributions changed substantially from previous parameterizations, as shown in Figure 1.1 when these data were included in the CTEQ5 [12] and MRST [20] global fits. Fermilab E866/NuSea observed a large asymmetry in the sea distributions at moderate x; however, with x increasing, the sea appears to become more flavor symmetric – a sign of a possible change in the mechanism generating the sea. At the same time, however, the statistical uncertainty of the data grew significantly.

In order to improve the precision of the E866/NuSea experiment, the SeaQuest experiment at Fermi National Accelerator Laboratory aims to study $\bar{d}(x)/\bar{u}(x)$ at larger x and to answer a number of questions relating to the parton structure of nuclei and the nucleon at higher x. The lower beam momentum of the Main Injector (120 GeV) provides an excellent opportunity to study these distributions at larger x. For fixed x, the Drell-Yan cross section is inversely proportional to the square of the center-of-mass energy, s. At the same time, the primary background, J/ψ production, which limited the instantaneous luminosity in the E866/NuSea experiment, scales with s. Therefor a more intense proton beam can be used at SeaQuest. The combination of these effects yield a factor of 50 increase in the number of Drell-Yan events for the same amount of beam time. SeaQuest is expected to determine the ratio $\bar{d}(x)/\bar{u}(x)$ for $0.1 < x < 0.45$.

In spring 2012, the first 120 GeV proton beam was successfully extracted from the Fermilab Main Injector Ring to the fixed target beamline of SeaQuest. The average intensity of the protons during the 6 weeks of commissioning run was 7×10^{11} per spill. This thesis reports developments of analysis methods for the dimuon track reconstruction based on data from the commissioning run. The track reconstruction at SeaQuest consists of two steps: the "track finding" which combines hits in the different drift chambers to a track candidate, and the "track fitting" which determines the momentum of a muon track based on the known map of the magnetic field of the

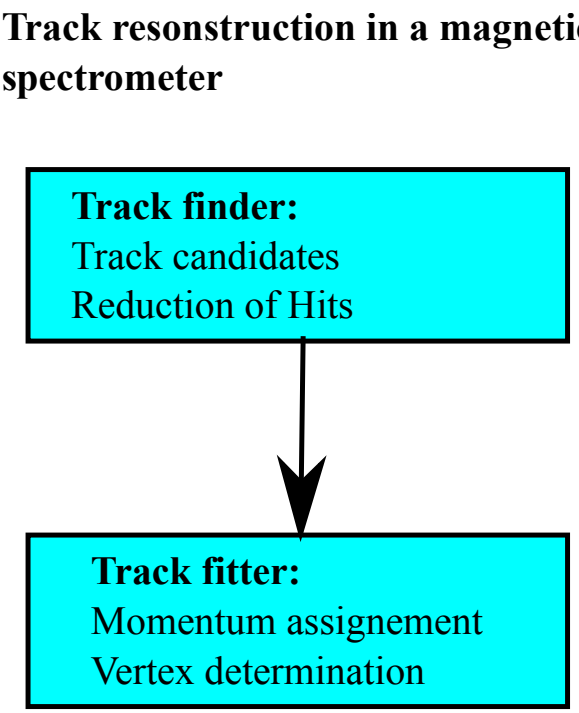

Figure 1.2: Track reconstruction consists out of two steps: track finding which finds track candidates and track fitting which is responsible for the momentum assignment.

spectrometer. Figure 1.2 shows the principle of track reconstruction. I stayed half time of the doctor course at Fermilab, in order to prepare the drift chambers and the drift chamber read-out electronics for the commissioning run. My analysis work during the doctor course focused on the development of a track finder algorithm. I independently developed such kind of pattern recognition algorithm which allows to judge if hits belong to a muon track or not in a fast and efficient manner. Combining my track finder algorithm with a track fitter, I established a new method to increase the yield of reconstructed dimuons. I determined precisely the kinematics of dimuons, such as the dimuon invariant mass, which are essential for the SeaQuest experiment.

Outline of the thesis

This thesis is organized as follows. We will introduce a method of analyzing dimuon pairs in the SeaQuest spectrometer. The theoretical framework and motivation for the SeaQuest experiment is described in Chapter 2. A phenomenological and historical perspective is adopted for the description of the Drell-Yan processes. A detailed treatment of the formalism concerning the inner structure of the proton is presented as well. In Chapter 3 the main components of the SeaQuest experimental apparatus

are presented. We will focus on the description of the main features of the spectrometer, tracking and trigger, data acquisition and read-out hardware. In Chapter 4 we present the main steps of track reconstruction at SeaQuest. Therefore, we focus on the description of a novel track finder algorithm and the track fitting methods at SeaQuest. After a brief overview of the main steps of the underlying data analysis in Chapter 5, we show and discuss the details of the essential data handling. In Chapter 6 the results of the invariant mass and other kinematic variables are presented. Final conclusions and a brief summary are reported in Chapter 7.

Chapter 2

The Phenomenology on the Nucleon Internal Structure

2.1 ep Scattering

2.1.1 Deep-Inelastic Scattering (DIS)

A successful tool to gain information about the inner structure of the nucleon is the deep-inelastic scattering (DIS) process which is described in this section. Inclusive measurement of deep-inelastic scattering was the first method with which point-like partons were identified inside the nucleon. In the deep-inelastic scattering process a lepton scatters off a nucleon via the exchange of a virtual boson. Details on this type of reactions can be found in [21, 22, 23].

The exchange of a single virtual photon, as shown in Figure 2.1, is the dominant process. After the scattering the nucleon breaks up and forms a final hadronic state X. The maximum possible momentum transfer is determined by the centre-of-mass energy $\sqrt{s}$. In inclusive measurement only the scattered lepton is detected whereas additional hadrons of the final state X are detected in semi-inclusive measurement. In contrast to inclusive and semi-inclusive DIS the state X is fully reconstructed in exclusive measurement. The momentum transfer $q = k - k'$ is space-like so we use $Q^2 = -q^2$. The squared momentum transfer to the target, Q^2, is a measure of the spatial resolution in the scattering process. In DIS processes, Q^2 is large enough to resolve the constituents of the nucleon (cf. Figure 2.4). The energy loss for the electron is expressed as $\nu = P \cdot q / m_N$ in the laboratory frame.

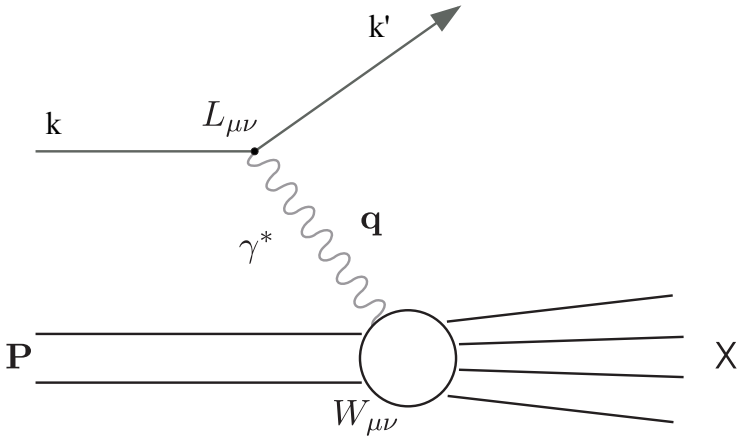

Figure 2.1: Lowest order DIS process in the one-photon exchange.

The invariant matrix element of the process is given by

$$i\mathcal{M}(eN \to eX) = \bar{u}(k',\lambda')(-ie\gamma_\mu)u(k,\lambda)\left(\frac{-ig_{\mu\nu}}{q^2}\right)\int d^4x\, e^{iqx}\langle X|J^\nu(x)|P,\lambda\rangle, \tag{2.1.1}$$

where $J^\nu(x)$ is the quark electromagentic current

$$J^\nu(x) = \sum_f Q_f \bar{q}_f\, \gamma^\nu q_f. \tag{2.1.2}$$

Here, Q_f is the electromagnetic charge of quark flavor q in units of the elementary charge $|e|$. The hadronic matrix element $\langle X|J^\nu|P\rangle$ cannot be calculated by perturbation theory as the QCD coupling is large at the scale of the nucleon mass. To obtain the cross section from this matrix element, it must however be squared and summed over all possible final states X. Using the optical theorem we can write the result as a product

$$d\sigma \propto L_{\mu\nu}W^{\mu\nu}, \tag{2.1.3}$$

where the leptonic tensor $L_{\mu\nu}$ is calculable using pure QED:

$$\begin{aligned} L_{\mu\nu} &= 2(k_\mu k'_\nu + k'_\mu k_\nu - g_{\mu\nu}(k'\cdot k - m_e^2) + i\,\varepsilon_{\mu\nu\rho\sigma}\, s_e^\rho q^\sigma) \\ &= 2(L^{(S)}_{\mu\nu} + iL^{(A)}_{\mu\nu}) \end{aligned} \tag{2.1.4}$$

and the hadronic part $W^{\mu\nu}$ can be decomposed as follows

$$W^{\mu\nu}(P,q)_{\lambda,\lambda'} = \frac{1}{4\pi}\int d^4x\, e^{iqx}\langle P,\lambda'|[J^\mu(x),J^\nu(0)]|P,\lambda\rangle. \tag{2.1.5}$$

As the nucleon is a spin-$\frac{1}{2}$ particle with polarisation s, we can define the density matrix [23]

$$\rho = \frac{1}{2}\left(1 + \frac{\vec{\sigma}\cdot\vec{s}}{m_N}\right) \tag{2.1.6}$$

and combine it with Equation (2.1.5) to

$$W^{\mu\nu}(P,q,s) = \mathrm{Tr}(\rho W^{\mu\nu}) = W^{\mu\nu}_{(S)} + iW^{\mu\nu}_{(A)}. \tag{2.1.7}$$

$W^{\mu\nu}_{(S)}$ is the symmetric, spin independent part of $W^{\mu\nu}$, whereas $W^{\mu\nu}_{(A)}$ is the anti-symmetric part containing all spin-dependent information of the nucleon. The complex inner structure of the nucleon prevents the exact calculation of the hadronic tensor. Only a parametrization in terms of structure functions is possible. A further advantage of the decomposition of $W^{\mu\nu}$ in

$$W^{\mu\nu}_{(S)} = \left(-g_{\mu\nu} + \frac{q^\mu q^\nu}{q^2}\right)F_1(x,Q^2) + \frac{1}{P\cdot q}\left(P^\mu - \frac{P\cdot q}{q^2}q^\mu\right)\left(P^\nu - \frac{P\cdot q}{q^2}q^\nu\right)F_2(x,Q^2), \tag{2.1.8}$$

$$W^{\mu\nu}_{(A)} = \frac{1}{P\cdot q}\varepsilon^{\mu\nu\rho\sigma}q_\rho\left(s_\sigma g_1(x,Q^2) + \left(s_\sigma - \frac{s\cdot q}{P\cdot q}P_\sigma\right)g_2(x,Q^2)\right) \tag{2.1.9}$$

is that it fulfills additional symmetry requirements as Lorentz covariance, gauge invariance, and parity conservation of the electromagnetic interaction. In Equations (2.1.8) and (2.1.9), we have introduced the variable x. It is called 'Bjorken scaling variable' and is defined as

$$x = \frac{-t}{s+u} = \frac{Q^2}{2k\cdot P - 2k'\cdot P} = \frac{Q^2}{2P\cdot q} = \frac{Q^2}{2m_N\nu}. \tag{2.1.10}$$

It satisifies $0 \le x \le 1$ because $s = (P+q)^2 \ge m_N^2$. It can be interpreted as a measure for the in-elasticity of the scattering process, where $x = 1$ corresponds to the fully elastic limit. The functions F_1, F_2 and g_1, g_2 are called the structure functions of the nucleon. From the Lorentz structure of the leptonic tensor $L_{\mu\nu}$ we can see that F_1 and F_2 can be determined from unpolarized DIS experiments while in order to measure g_1 and g_2 polarized particles are necessary. Figure 2.2 shows the latest results of DIS measurements on g_1 and F_2.

Using the relative energy transfer

$$y = \frac{\nu}{E_e} = \frac{p\cdot q}{p\cdot k}, \tag{2.1.11}$$

the final unpolarised cross section can be written in a very compact form:

$$\frac{d^2\sigma}{dxdy}(eN \to eX) = \frac{4\pi\alpha^2}{Q^4} s[xy^2 F_1(x,Q^2) + (1-y)F_2(x,Q^2)] \tag{2.1.12}$$

If both the incident lepton beam and the target protons are longitudinally polarized, the antisymmetric (spin-dependent) parts of the leptonic and hadronic tensors contribute to the cross section. In this case both the symmetric and anti-symmetric part of the cross section are non-vanishing, so the only way to isolate the spin-dependent component is measuring the difference of the cross sections obtained with two opposite target or beam spin states. More details on the calculation of polarized and unpolarized DIS cross sections can be found in Reference [24], for instance. An overview over all relevant kinematic variables in DIS can be found in Table 2.1.

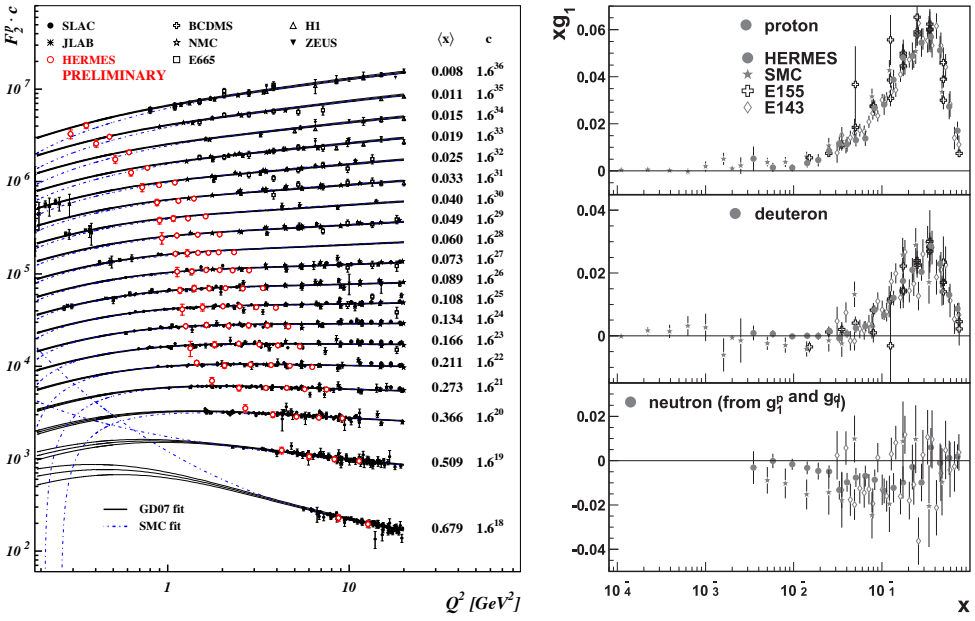

Figure 2.2: Left: The world data of F_2^p is compared to phenomenological parameterizations. Latest HERMES results covering the low-x region are included (red circles). Source: [25]. **Right**: The spin-dependent structure function xg_1 of the proton, deuteron, and neutron measured as function of x in DIS of polarized leptons. Source: [26]

2.1.2 The Quark Parton Model

The Quark Parton Model (QPM) was developed by Bjorken and Feynman in the late 1960's [1, 2, 3]. The QPM is conveniently formulated in a reference frame where the nucleon moves with very high momentum (infinite-momentum frame or

Variable	Description
$k = (E, \vec{k}),\ k' = (E', \vec{k}')$	4-Momentum of Incoming and Outgoing Lepton
$P \overset{\text{lab}}{=} (m_N, \vec{0})$	4-Momentum of the Target nucleon
$\phi,\ \theta$	Polar and Azimuthal Scattering Angles
$q = (\nu, \vec{q})$	4-Momentum of the Virtual Photon
$Q^2 = -q^2 \overset{\text{lab}}{\cong} 4EE'\sin^2(\theta/2)$	Negative Squared 4-Momentum Transfer
$\nu = \frac{P\cdot q}{m_N} = E - E'$	Energy Transfer from the Incoming Lepton to the Target Nucleon
$x = \frac{Q^2}{2P\cdot q} \overset{\text{lab}}{\cong} \frac{Q^2}{2m_N\nu}$	Bjorken Variable
$y = \frac{P\cdot q}{P\cdot k} \overset{\text{lab}}{\cong} \frac{\nu}{E}$	Fractional Energy of the Virtual Photon
$W^2 = (P+q)^2 \overset{\text{lab}}{\cong} m_N^2 + 2m_N\nu - Q^2$	Squared Invariant Mass of the Hadronic Final State
$P_h = (E_h, \vec{P}_h)$	4-Momentum of a Final State Hadron
$z = \frac{P\cdot P_h}{P\cdot k} \overset{\text{lab}}{\cong} \frac{E_h}{\nu}$	Fractional Energy of the Final State Hadron
$P_{h\perp} = \frac{\lvert\vec{P}_h\times\vec{q}\rvert}{\lvert\vec{q}\rvert}$	Transverse Momentum of the Hadron
ϕ_h	Azimuthal Angle of the Hadron w.r.t. Scattering Plane

Table 2.1: Summary of the most important kinematic variables used in DIS.

Breit frame), such that the transverse momentum components and the rest mass of the constituents and the nucleon itself can be neglected. In this special frame the scattering can be viewed as the absorption of a virtual photon by one of the collinearly moving partons inside the nucleon. The struck parton, which carries a fraction $p = \xi P$ of the total momentum of the nucleon, recoils with its original momentum reversed, as shown in Figure 2.3. After the absorption of the virtual photon, the mass-shell relation for the struck parton yields:

$$(\xi P + q)^2 = (\xi P)^2 + 2\xi P \cdot q - Q^2 = 0, \tag{2.1.13}$$

where $q = (\nu, \vec{q})$ is the four-momentum of the virtual photon and $Q^2 = -q^2$. Being a Lorentz invariant quantity, Equation (2.1.13) also holds in the laboratory frame, where $P = (m_N, \vec{0})$ (e.g. for a fixed target experiment):

$$(\xi m_N)^2 + 2\xi m_N \nu - Q^2 = 0. \tag{2.1.14}$$

In the scaling limit $Q^2 \gg m_N^2$, ξ can be identified with the definition of the Bjorken x variable (cf. Equation (2.1.10)). In the QPM the Bjorken x variable can thus be interpreted as the fractional momentum of the nucleon carried by the struck quark, and the DIS process consists of the incoherent sum of elastic scattering off the partons carrying a momentum fraction x of the nucleon momentum. Thus we use x instead of ξ. The limit $Q^2 \to \infty$, $\nu \to \infty$ and $x = fixed$ is called Bjorken limit (which is equivalent to the expressions Bjorken scaling or scale invariance). This means that for the full nucleon, built up from partons of type q with distributions $q(x)$, we can write the cross section as a sum of incoherent single parton scatterings (cf. Figure 2.3):

$$\sigma(eN \to eX) = \int_0^1 dx \sum_q q(x)\, \sigma(e\, q(xP) \to e q(p')). \tag{2.1.15}$$

The model, however, requires that the interaction between the individual partons is weak at short distance. This circumstance is satisfied if the scattering occurs on sufficiently short time scales, i.e. much shorter that the typical time scales of the interactions between partons. In this approximation, known as Impulse Approximation, the partons can be regarded as a gas of quasi-free particles.

The QPM the nucleon is described in terms of the parton distribution functions (DF) $q(x)$, which represent the probability density to find in the nucleon a quark of flavor q with fractional momentum x. The quantity $q(x)\,dx$ thus represents the

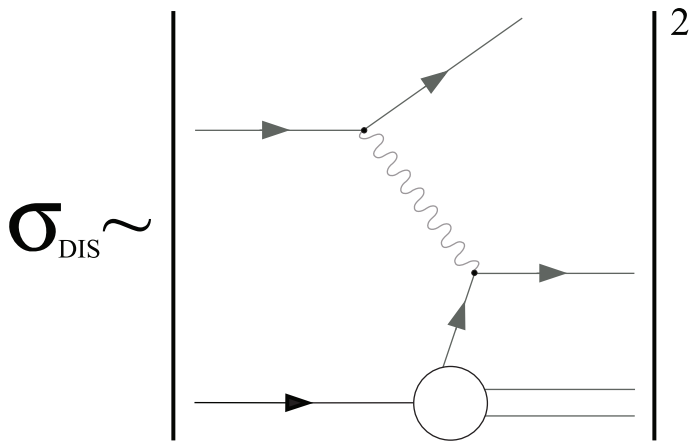

Figure 2.3: DIS in the parton model (laboratory frame!). The proton target is a cloud of partons and the lepton scatters elastically from one of the partons by exchanging a virtual photon.

number of quarks with flavor q with fractional momentum in the range $[x, x+dx]$. In the helicity base, the DF $q(x)$ can be split up in functions for quarks with parallel $(+)$ and anti-parallel $(-)$ orientation of the spin with respect to the nucleon spin:

$$q(x) = q^+(x) + q^-(x). \tag{2.1.16}$$

It is possible to define some constraints by the number of valence quarks of given flavour N_q.

$$\int_0^1 dx\,[q(x) - \bar{q}(x)] = N_q. \tag{2.1.17}$$

Thus summing over all possible momentum fractions yields the full nucleon momentum

$$\sum_{q,\bar{q},g} \int_0^1 dx\, x\, q(x) = 1, \tag{2.1.18}$$

if gluon is also taken into account. The polarized or helicity PDF is then defined as

$$\Delta q(x) = q^+(x) - q^-(x). \tag{2.1.19}$$

The spin-independent and spin-dependent structure functions F_1, F_2 and g_1 (cf. previous Subsection) can now be interpreted within the QPM as the charge-weighted sums over the quark flavors q (including antiquarks) of the corresponding parton

distribution functions:

$$F_1(x) = \frac{1}{2}\sum_q e_q^2 q(x) \tag{2.1.20}$$

$$g_1(x) = \frac{1}{2}\sum_q e_q^2 \Delta q(x) \tag{2.1.21}$$

$$g_2(x) = 0, \tag{2.1.22}$$

where e_q is the fractional charge carried by the quarks. Since the structure function g_2 is related to the transverse degrees of freedom of the quarks within the nucleon, it has no interpretation and vanishes in the QPM where all the partons are assumed to move collinearly to the nucleon. The structure functions $F_1(x)$ and $F_2(x)$ are connected via the Callan-Gross [27] relation by

$$F_2(x) = 2xF_1(x). \tag{2.1.23}$$

In general the structure functions vary with x and Q^2. In the QPM, however, they are independent of Q^2. This leads to the famous Bjorken scaling. The tree level process in Figure 2.3, of course, has to be corrected by higher order processes. This allows for a dependence on Q^2, which is however relatively mild, of the order of $\ln Q^2$. These "scaling violations" were a direct test of QCD. A Q^2-independence of the structure functions would imply that the electromagnetic probe (incoming lepton) "sees" the same proton structure no matter how big the spatial resolution is (cf. Figure 2.4).

2.1.3 Quantum Chromodynamics

The violation of Bjorken scaling can be explained if quarks interact with each other in the nucleon. In late 1970s, a field theory of Quantum Chromodynamics (QCD) was developed whose basic fields are quarks interacting via electrically neutral vector gluons. QCD is the non-Abelian gauge theory of the strong interaction and part of the Standard Model. Quarks couple to the strong interaction through three different colors. In contrast to Quantum Electrodynamics where the photons have no electrical charge and cannot couple to each other, the field quanta of the strong interaction, i.e., the gluons, do carry color charge. This causes a scale or energy

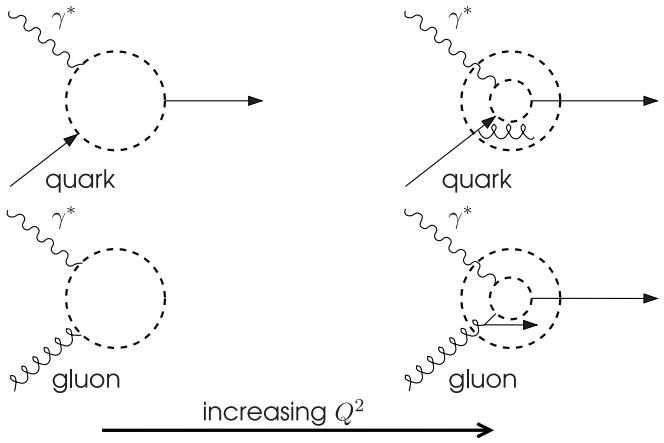

Figure 2.4: Improving resolution for increasing Q^2.

dependence of the strong coupling constant α_S:

$$\alpha_S(Q^2) = \frac{12\pi}{(33 - n_f)\ln(Q^2/\Lambda_{\mathrm{QCD}^2})} \tag{2.1.24}$$

The QCD scale parameter Λ_{QCD} depends on the number of quark flavours n_f and the renormalisation scheme. It is of the order of a couple of hundred MeV. Equation (2.1.24) is only valid for $Q^2 \gg \Lambda_{\mathrm{QCD}}$ and shows that the coupling decreases with increasing Q^2 and reaches zero for $Q^2 \to \infty$, i.e. in the Bjorken limit explained in the previous Subsection. This feature, which only appears in non-Abelian gauge theories, is called asymptotic freedom. It explains the success of the description of experimental results with the QPM in which the quarks are treated as free partons. For $\alpha_s \ll 1$ perturbative QCD is applicable and only lower order diagrams have to be taken into account. But the coupling constant is not necessarily smaller than 1 for small Q^2 so that perturbation theory fails. In the so-called confinement region ($Q^2 \lesssim 1\,\mathrm{GeV}^2$), where α_S is of the order of 1 or larger, phenomenological models or QCD calculations on the lattice are used to describe the experimental data.

Due to the fact that quarks and gluons interact, gluons dress the quarks in the nucleon with a cloud of gluons and virtual quark-antiquark pairs, so-called sea quarks. With increasing Q^2 the wavelength of the virtual photon decreases and the resolution of the external probing current increases. A quark which is not resolved at low Q^2 can therefore be resolved at larger Q^2 as a quark with lower momentum plus gluons (see Figure 2.4, top-panel). Hence, there is a depletion of high momentum partons and an increase in the low momentum parton distribution as Q^2 increases. This behavior can be seen in Figure 2.2 where the structure function F_2, i.e., the sum of the distribution functions of the different quark and antiquark flavors weighted

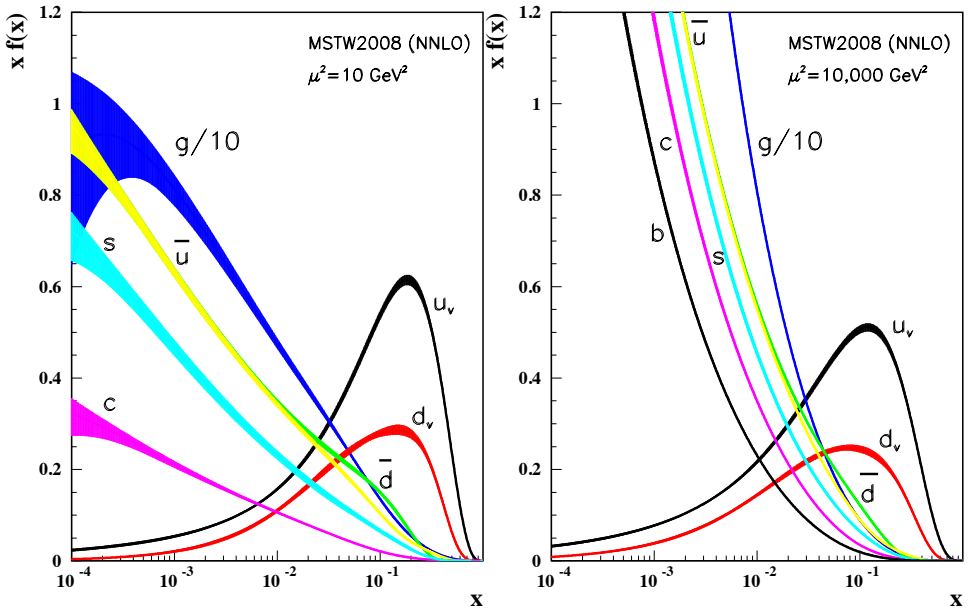

Figure 2.5: Distributions of x times the unpolarized parton distributions and their associated uncertainties using the NNLO MSTW2008 parameterization [32] at a scales of $Q^2 = 10\,\mathrm{GeV}^2$ (left) and $Q^2 = 100\,\mathrm{GeV}^2$ (right).

by x is plotted as a function Q^2 for different values of x. In addition, there is an enhancement of partons at small x due to resolved gluons. At low Q^2 a photon does not interact with the electrically neutral gluon. With sufficient large Q^2 the gluon can be resolved into a quark-antiquark pair and the photon can interact with one of them (see Figure 2.4, bottom-panel).

In leading order perturbative QCD, the structure functions have the same form as in the QPM (Equations (2.1.20)–(2.1.23)):

$$F_1(x,Q^2) = \frac{1}{2}\sum_q e_q^2 q(x,Q^2) \tag{2.1.25}$$

$$g_1(x,Q^2) = \frac{1}{2}\sum_q e_q^2 \Delta q(x,Q^2) \tag{2.1.26}$$

The Callan-Gross relation in Equation (2.1.23) also holds in the so-called QCD improved QPM. Their logarithmic Q^2 behaviour is described by the Dokshitzer-Gribov-Lipatov-Altarelli-Parisi (DGLAP) equations [28, 29, 30, 31].

By combining the data from different experiments (fixed target experiments and collider experiments, like HERA at DESY or the TEVATRON at Fermilab),

it is possible to extract unpolarized parton distribution functions (PDFs). Early parameterizations of the PDF's relied on fits to the structure functions measured in DIS experiments which are primarily sensitive to the light quark distributions ($u(x)$ and $d(x)$). More modern parameterizations, such as those performed by the CTEQ [12, 11], MRST [13, 20, 32] and GRV [16] collaborations use several different physical processes to extract complementary information about the parton distributions. The lepton-charge asymmetry observed in $W^{\pm}$ production provides additional information on the light quark distributions, while jet production and prompt photon measurements are used to constrain the gluon distributions. The Drell-Yan process for dilepton production, which involves quark-antiquark annihilation, provides constraints on the light antiquark distributions ($\bar{u}(x)$ and $\bar{d}(x)$) in the nucleon sea. An example of the result of a NNLO (Next to next to the leading order) global analysis [32] can be seen in Figure 2.5 at scales of $Q^2 = 10\,\mathrm{GeV}^2$ and $Q^2 = 100\,\mathrm{GeV}^2$.

2.1.4 The NMC Experiment and the Gottfried Sum Rule

An experiment performed by the New Muon Collaboration (NMC) at CERN measured the cross section ratio for deep inelastic scattering of muons from hydrogen and deuterium [17, 18]. Their measurement of F_2^n/F_2^p over the kinematic range of $0.004 < x < 0.8$ is shown in Figure 2.6. These data points are the result of measurements combining both the 90 GeV and 280 GeV incident muon energy and adjusting the data for the small Q^2 dependence to a fixed Q^2 of $4\,\mathrm{GeV}^2$.

The NMC measurement was used together with a parameterization of the absolute deuteron structure function, F_2^d, to obtain

$$F_2^n - F_2^p = 2F_2^d \frac{1 - F_n^2/F_p^2}{1 + F_n^2 - F_p^2}\,. \tag{2.1.27}$$

The solid points in Figure 2.7 show the derived values of $F_n^2 - F_p^2$ as a function of x. Also shown in this figure is $\int_x^1 \left(F_n^2 - F_p^2\right) dx/x$ for the same x range of the data as well as the extrapolated result (S_G) over all values of x ($0 \leq x \leq 1$). This extrapolated result is

$$S_G = \int_0^1 \left[F_2^p - F_2^n\right] \frac{dx}{x} = 0.235 \pm 0.026\,. \tag{2.1.28}$$

This result by NMC can be compared to the traditional Gottfried Sum Rule (GSR) [33] result of $1/3$. To understand this discrepancy between the NMC mea-

surement and the traditional expectation of the Gottfried Sum Rule, it is important to look at the assumptions that lead to the traditional expectation. Beginning with the Gottfried sum as written in Equation (2.1.28) and then using Equation (2.1.23), we obtain

$$S_G = \int_0^1 \sum_i e_i^2 \left[q_i^p(x) + \bar{q}_i^p(x) - q_i^n(x) - \bar{q}_i^n(x) \right] dx. \tag{2.1.29}$$

By assuming charge symmetry (i.e. $u_p(x) = d_n(x), \bar{d}_p(x) = \bar{u}_n(x)$ etc.) to express the neutron PDF's as proton PDF's and ignore the heavier quark (e.g. $s, \bar{s}, \ldots$) terms one yileds

$$S_G = \int_0^1 \frac{1}{3} \left[u(x) + \bar{u}(x) - d(x) - \bar{d(x)} \right] dx, \tag{2.1.30}$$

which can be rewritten as

$$S_G = \int_0^1 \frac{1}{3} \left[u(x) - \bar{u}(x) \right] dx - \int_0^1 \frac{1}{3} \left[d(x) - \bar{d}(x) \right] dx + \int_0^1 \frac{2}{3} \left[\bar{u}(x) - \bar{d}(x) \right] dx. \tag{2.1.31}$$

The first two integrals are the definition of the valence quarks, which for a proton is two up valence quarks and one down valence quark. Thus, Equation (2.1.31) is reduced to

$$S_G = \frac{1}{3} + \int_0^1 \frac{2}{3} \left[\bar{u}(x) - \bar{d}(x) \right] dx. \tag{2.1.32}$$

Assuming that $\int_0^1 \bar{d}(x)dx = \int_0^1 \bar{u}(x)dx$, then one arrives at the traditional result of $1/3$.

To reconcile the NMC measurement and the traditional expectation, one of the three assumptions made above must be incorrect: the first assumption is that the NMC measurement was correctly extrapolated to zero; second, that charge symmetry is valid; and third, that $\int_0^1 \bar{d}(x)dx = \int_0^1 \bar{u}(x)dx$.

The small-x extrapolation was checked by Fermilab E665 [34], which made the same measurement as NMC. The x coverage at E665 was $10^{-6} \leq x \leq 0.3$. Over the overlapping kinematic range, the results agree well. While E665 seems to support the NMC extrapolation, it also highlights the difficulty of making and interpreting DIS measurements at small x values.

Charge symmetry is generally assumed to be well respected in strong interactions. Extensive experimental searches for charge symmetry violation effects have shown that charge symmetry holds to the order of the proton-neutron mass difference [35, 36]. Therefore, charge symmetry cannot explain the discrepancy between the NMC measurement and the traditional Gottfried Sum result.

The only remaining assumption is $\int_0^1 \bar{d}(x)dx = \int_0^1 \bar{u}(x)dx$. If this assumption is

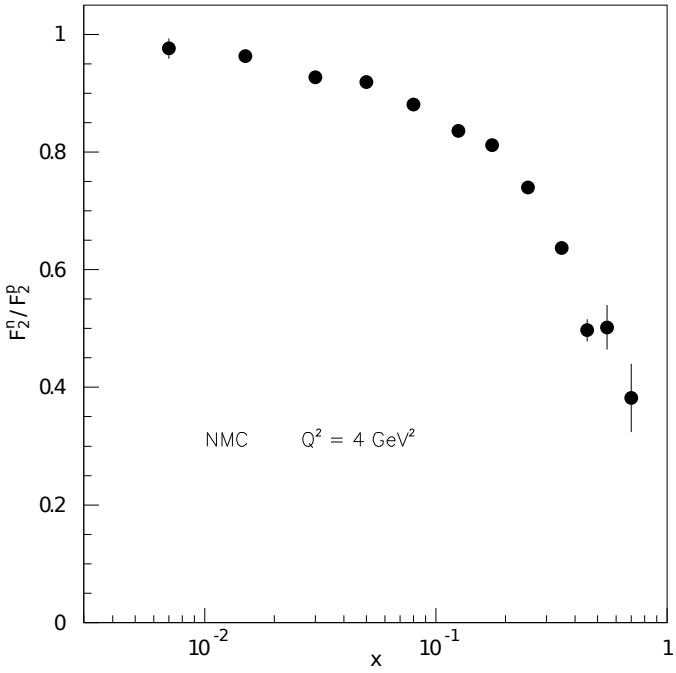

Figure 2.6: The ratio F_2^n/F_2^p at scale of $Q^2 = 4\,\mathrm{GeV}^2$ measured by the NMC experiment. Only the statisitical uncertainty is shown.

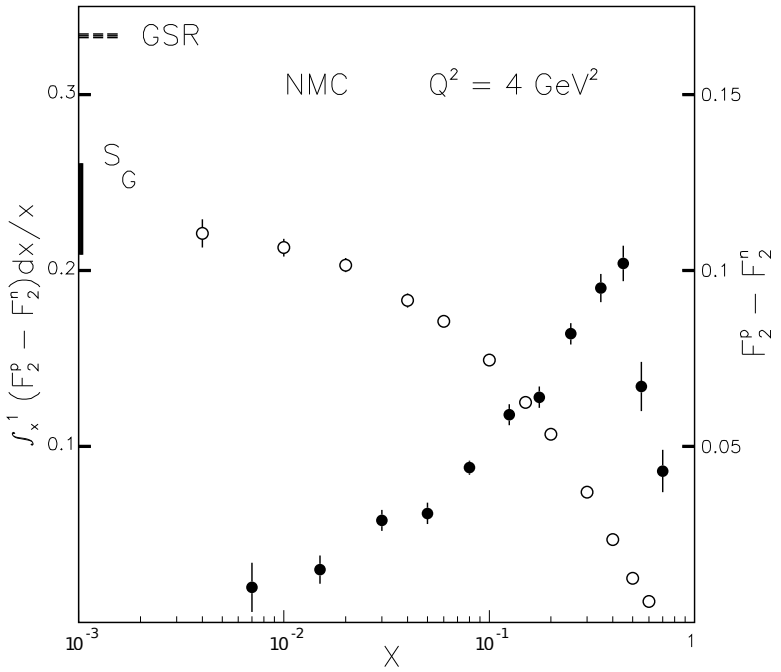

Figure 2.7: The difference $F_2^p - F_2^n$ (solid symbols and the scale to the right) and $\int_x^1 \left(F_2^p - F_2^n\right) dx/x$ (open symbols and the scale to the left) at $Q^2 = 4\,\mathrm{GeV}^2$ as a function of x. The extrapolated integral result, S_G is indicated by the bar. The traditional Gottfried Sum Rule expectation, GSR is also shown.

the only cause for the discrepancy between the NMC measurement and the traditional Gottfried Sum result, it would imply

$$\int_0^1 \left[\bar{u}(x) - \bar{d}(x)\right] dx = 0.148 \pm 0.039\,. \tag{2.1.33}$$

The NMC measurement and the above analysis were the first indications that there were more anti-down quarks in the proton than anti-up quarks.

2.2 The Drell-Yan Process

2.2.1 Cross Section for the Drell-Yan Process

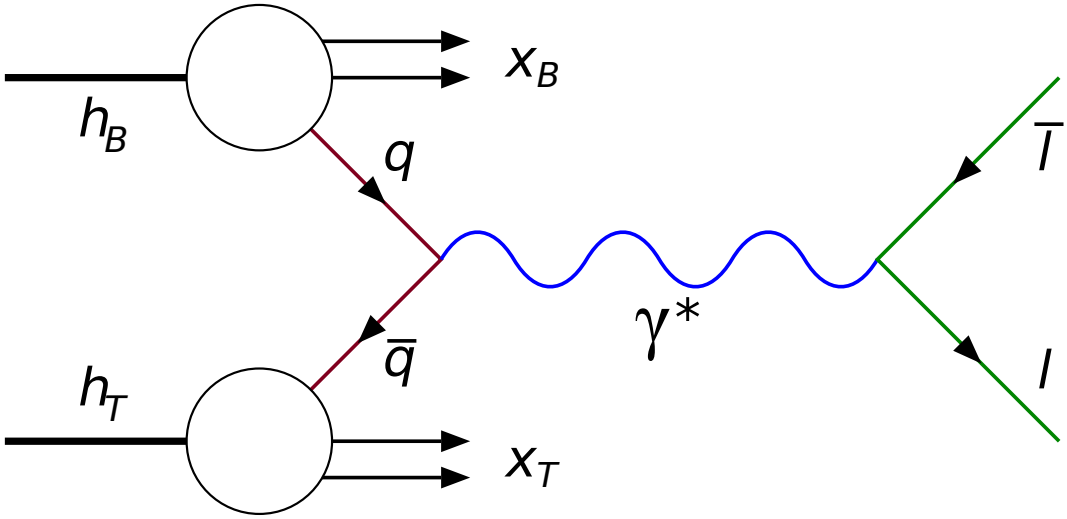

Figure 2.8: Feynman diagram for the leading order Drell-Yan process.

In the Drell-Yan process, a virtual photon is produced through the annihilation of a quark (or antiquark) from the beam (target) with an antiquark (or quark) in the from the target (beam). This results in a time-like ($Q^2 > 0$) intermediate virtual photon, which decays into an oppositely charged lepton pair (see Figure 2.8):

$$q\bar{q} \to \gamma^* \to l^+ l^- \tag{2.2.1}$$

The production of massive dileptons through quark-antiquark annihilation can be expressed in terms of a hard, short-distance interaction term representing the cross section, $\sigma_{q\bar{q}}$ (illustrated in Figure 2.8) and the parton probability densities within

the interacting hadrons. The hard scattering cross section is given by

$$\sigma_{q\bar{q}} = \frac{4\pi\alpha^2}{3M_{\gamma^*}^2}\frac{1}{3}e_i^2, \tag{2.2.2}$$

where the cross section is reduced by the final factor of $1/3$ since the color-charge of the quark and antiquark must match, e_i is the fractional charge of the quark and $M_{\gamma^*}^2$ is the dilepton mass. In order to obtain the hadron-hadron cross section, it is necessary to sum over the available quark flavors and account for the parton distributions. To leading order in the strong coupling constant, α_S, the Drell-Yan cross section is then

$$\begin{aligned}\frac{d^2\sigma}{dx_1dx_2} &= \frac{4\pi\alpha^2}{9M_{\gamma^*}^2}\sum_i \left[f_i(x_1,Q^2)\bar{f}_i(x_2,Q^2) + \bar{f}_i(x_1,Q^2)f_i(x_2,Q^2)\right] \\ &= \frac{4\pi\alpha^2}{9x_1x_2s}\sum_i \left[f_i(x_1,Q^2)\bar{f}_i(x_2,Q^2) + \bar{f}_i(x_1,Q^2)f_i(x_2,Q^2)\right] .\end{aligned} \tag{2.2.3}$$

The sum is over quark flavors, $i \in \{u,d,s,\ldots\}$. The parton distributions functions (PDFs) are given by $f_i(x,Q^2)$, where x is Bjorken variable and Q^2 is the QCD scale at which the parton distribution is probed. In the case of Drell-Yan scattering, $Q^2 = M_{\gamma^*}^2$. (In general, $M_{\gamma^*}^2$ are used when discussing an invariant mass measured by an experiment and Q^2 refers to the QCD scale.) The subscripts 1 and 2 denote the interacting hadrons which, in a fixed target experiment, are conventionally take as 1 for the beam hadron and 2 for the target hadron. The squared total energy of the beam-target system, for a fixed target experiment, is $s = 2m_2E_1 + m_1^2 + m_2^2$ where E_1 the energy of the beam hadron and m_1 (m_2) the rest masses of the beam (target) hadron. In the case of nuclear targets, it is assumed that the reaction takes place on a component nucleon, $m_2 = M_n$, where M_n is the nucleon mass, and the momentum fraction, x_2 refers to the fractional momentum of the parton relative to the interacting nucleon.

The sensitivity of the Drell-Yan process to the antiquark distributions of the target and beam is clear from examining Equation (2.2.3). At large values of x, the parton distributions are dominated by the valence distributions and at small x by the sea distributions. Thus, in the limit of large x_1 and small x_2, the cross section is dominated by the first term – the annihilation of beam quarks with target antiquarks – providing direct sensitivity to the antiquark sea of the target. This limit is exactly the kinematics selected by a dipole-based spectrometer's acceptance in a fixed-target environment where all particles are boosted in forward direction.

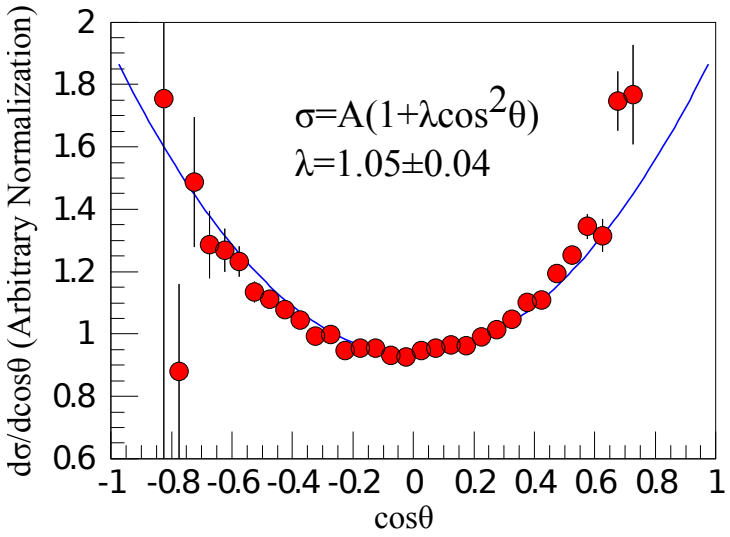

Figure 2.9: The $1+\cos^2\theta$ dependence of the Drell-Yan cross section as measured by the E866/NuSea experiment [37]. The red data points are fitted with the function $A(1+\lambda\cos^2\theta)$.

This fixed target setup suppresses large x_2 and small x_1 since it automatically picks $x_F > 0$. which corresponds to the forward direction of the dimuon boost.

Detailed derivations of this cross section can be found in the literature [38, 39, 40]. The leading order Drell-Yan mechanism also predicts that the spin of the virtual photon are aligned. It provides a cross section that has a $(1+\cos^2\theta)$ dependence, where θ is the polar angle of the lepton in the rest frame of the virtual photon [8], in agreement with data as shown in Figure 2.9. Additional features of the angular distributions and their deviations from $(1+\cos^2\theta)$ are discussed in Section 2.4.

2.2.2 Kinematics of the Drell-Yan Process

Experimentally, one measures the momenta of the outgoing lepton and antilepton, allowing for the reconstruction of the virtual photon's mass, $M^2_{\gamma^*}$, longitudinal momenta, $p_l^{\parallel} = p_l$ and transverse momenta, $p_{\perp}^{\parallel} = p_{\perp}$. The transition from Eq. (2.2.2) to Eq. (2.2.3) can also be explained in terms of a center-of-mass (CMS) transformation. Eq. (2.2.2) is then the Drell-Yan cross section in the partonic CMS, whereas Equation (2.2.3) is the cross section in the hadronic CMS. It is then more convenient to introduce the variables

$$\tau = M^2_{\gamma^*}/s \tag{2.2.4}$$

and the rapidity

$$y = \frac{1}{2}\ln\left(\frac{E+p_l}{E-p_l}\right), \tag{2.2.5}$$

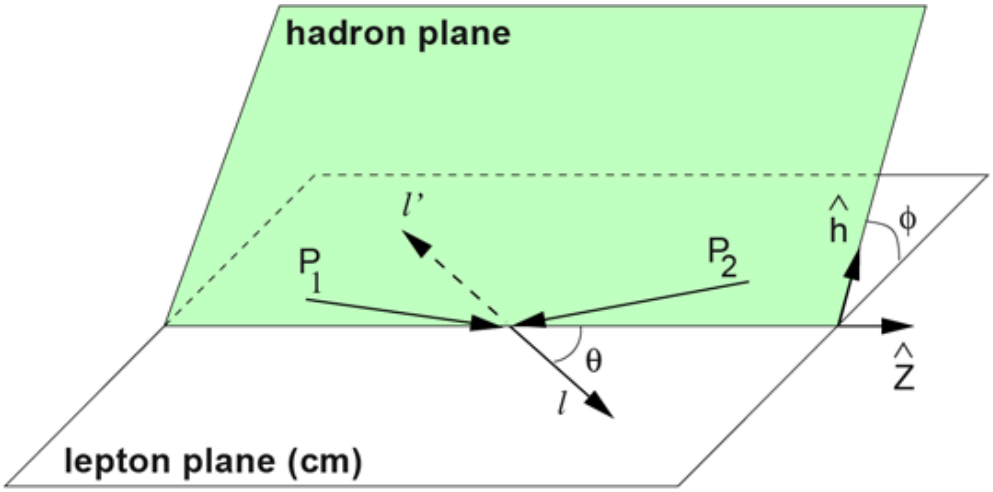

Figure 2.10: The definition of the Collins-Soper frame.

where s is the CMS energy of the interacting hadrons and E is the virtual photon's energy. From these, the momentum fraction x_1 and x_2 of the interacting partons are given by

$$x_{1,2} = \left(\tau + \frac{p_\perp^2}{s}\right)^{1/2} e^{\pm y} \tag{2.2.6}$$

and Feynman-x is then defined as follows

$$x_F \equiv \frac{2p_l}{\sqrt{s}} \approx x_1 - x_2. \tag{2.2.7}$$

In the limit of vanishing transverse momenta $p_\perp \to 0$ and large $\sqrt{s}$, this is equivalent to $M_{\gamma^*}^2 = x_1 x_2 s$ and $x_F = 2p_l/\sqrt{s} = x_1 - x_2$. For a detailed discussion on the differences, see [39].

The variables y, τ and $p_\perp$ are invariant under Lorentz transformations (LI). In order to completely specify the final state of the interaction, we need three more LI variables. These other variables are the polar decay angle θ_d, and the azimuthal production and decay angles ϕ_γ and ϕ_μ respectively. These variables are most naturally defined with respect to the $q\bar{q}$ annihilation axis. However, when $p_\perp$ is non-zero, it is more convenient to masure the angular variables with respect to the Collins-Soper frame [41], which is shown schematically in Figure 2.10. In this frame, the z-axis is taken to be parallel to the bisector of the angle between the interacting hadrons in the rest frame of the muon pair.

2.2.3 How the Di-Lepton Spectra can be interpreted

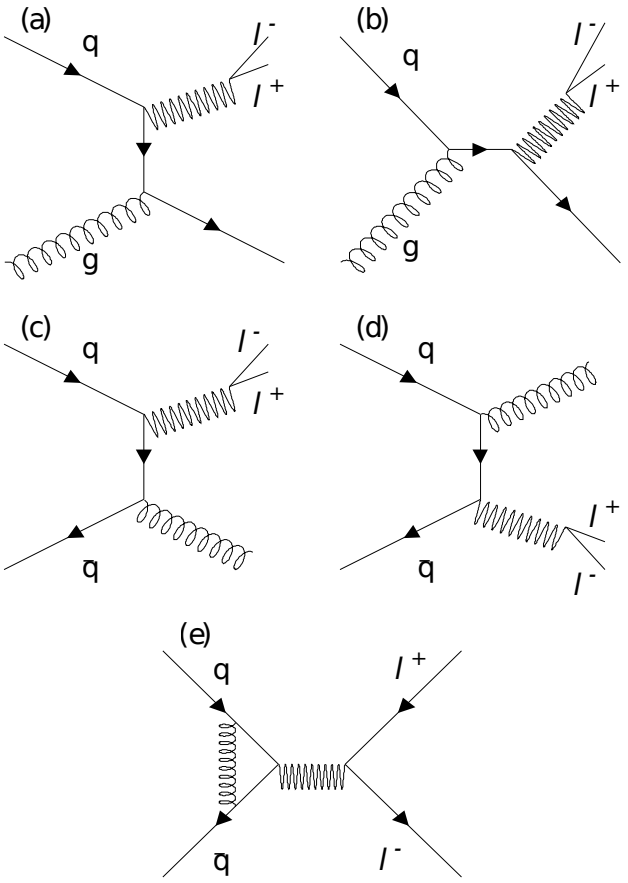

Figure 2.11: Feynman diagram for the terms of next-to-leading (NLO)order in α_S for the Drell-Yan process.

The interpretation of the observed dilepton spectra in terms of parton distributions relies on the factorization of the Drell-Yan cross section into an infrared safe, short range hard scattering and the parton distributions. It further requires that these parton distributions have the same meaning as DIS parton distributions (which is shown in the next paragraph). In a twist expansion, the cross section can be expressed in terms of powers of $1/(QR)$ where Q^2 is the hard scale and $R \approx \mathcal{O}(1/\Lambda_{\mathrm{QCD}})$ represents a non-perturbative scale:

$$\sigma_{\text{Drell-Yan}} = \sigma_{\text{Hard}} + \sum_n \mathscr{F}_{n=1}[1/(QR)^n], \tag{2.2.8}$$

where σ_{Hard} represents the convolution of the hard scattering quark-antiquark cross section with the PDFs. In leading order in α_S, σ_{Hard} is given by Eq. (2.2.3) but more generally it includes higher powers of α_S.

In Ref. [42] it has been shown that if the structure functions in Eq. (2.2.3) have the same definition as those in DIS, namely, if one employs the DIS factorization scheme given in Eq. (2.2.8), then the NLO part is calculable and becomes a multiplicative factor to the expression (2.2.3). The NLO QCD processes that contribute to Drell-Yan scattering are depicted in 2.11. These processes lead to a modification of the Drell-Yan cross section by introducing the so-called K-factor:

$$\frac{d\sigma}{dx_1 dx_2}(NLO) = K_{NLO}\frac{d\sigma}{dx_1 dx_2}(LO). \tag{2.2.9}$$

With PDFs defined in the DIS factorization scheme, the K_{NLO}-factor is given approximately by

$$K_{NLO} \approx 1 + \frac{\alpha_S}{2\pi}\left(1 + \frac{4}{3}\pi^2\right) \tag{2.2.10}$$

and assumes a value between 1.5 and 2 based on discrepancies between measured and calculated Drell-Yan cross sections. The consideration of NNLO, as well as NLO diagrams, also leads to a simple factorization of the cross-section and an approximate factor of two for K. The factorization scheme dependence of the K-factor is described in [43].

2.3 The Light antiquark Flavour Asymmetry of the Proton: $\bar{d}(x)/\bar{u}(x)$

The PDF's of antiquarks cannot be measured directly in experiments. However, the ratio $\bar{d}(x)/\bar{u}(x)$ or the difference $\bar{d}(x) - \bar{u}(x)$ of antiquark PDF's can be extracted from experimental observables. For example, the ratio $\bar{d}(x)/\bar{u}(x)$ in the proton can be determined by measuring the ratio of proton-induced Drell-Yan on deuterium to that on hydrogen. It is common to refer to the antiquark PDF's as the nucleon sea. Both Fermilab E866/NuSea [19, 44, 9] and CERN NA51 [10] used this method to determine $\bar{d}(x)/\bar{u}(x)$. In order to extract this from the measured observable - the cross section ratio - nuclear effects in deuterium were ignored. Its cross section was treated as the sum of the free proton and free neutron cross sections, yielding:

$$\sigma^{pp} \propto \frac{4}{9}u(x_1)\bar{u}(x_2) + \frac{1}{9}d(x_1)\bar{d}(x_2)\,, \tag{2.3.1}$$

$$\sigma^{pn} \propto \frac{4}{9}u(x_1)\bar{d}(x_2) + \frac{1}{9}d(x_1)\bar{u}(x_2)\,, \tag{2.3.2}$$

where charge symmetry was used to equate $\bar{d}_p(x)$ to $\bar{u}_n(x)$ and $\bar{u}_p(x)$ to $\bar{d}_n(x)$. By combining Equations (2.3.2) and (2.3.1), the ratio of the σ^{pd}/σ^{pp} yields

$$\frac{\sigma^{pd}}{2\sigma^{pp}} = \frac{1}{2}\frac{\sigma^{pp}+\sigma^{pn}}{\sigma^{pp}}. \tag{2.3.3}$$

In order to illustrate the sensitivity of Drell-Yan to this ratio, the above ratio of cross sections can be expresses as

$$\left.\frac{\sigma^{pd}}{2\sigma^{pp}}\right|_{x_1 \gg x_2} \approx \frac{1}{2}\left[\frac{1+\frac{d(x_1)}{4u(x_2)}}{1+\frac{d(x_1)}{4u(x_1)}\frac{\bar{d}(x_2)}{\bar{u}(x_2)}}\right]\left[1+\frac{\bar{d}(x_2)}{\bar{u}(x_2)}\right], \tag{2.3.4}$$

after ignoring the strange and heavier quark contribution and taking the limit that $x_1 \gg x_2$ (i.e. the fixed-target kinematics selected by the SeaQuestspectrometer, implying the beam antiquark-target quark contribution is small). Using that $d(x) \ll 4u(x)$, Equation (2.3.5) simplifies even further to

$$\left.\frac{\sigma^{pd}}{2\sigma^{pp}}\right|_{x_1 \gg x_2} \approx \frac{1}{2}\left[1+\frac{\bar{d}(x_2)}{\bar{u}(x_2)}\right]. \tag{2.3.5}$$

The actual extraction of $\bar{d}(x)/\bar{u}(x)$ performed by E866/NuSea (and is also going to be adapted by SeaQuest) used Equation (2.3.5) together with full next-to-leading order (NLO) cross section convolutions. The $\bar{d}(x)/\bar{u}(x)$ extractions were also verified through next-to-leading order global fits to the measured cross section ratios by CTEQ [11], MRST [20] and GRV [16].

2.3.1 Measurements of $\bar{d}(x)/\bar{u}(x)$ in the Past

The NA51 Experiment at CERN

The first dedicated measurement of the $\bar{d}(x)/\bar{u}(x)$ asymmetry using Drell-Yan scattering was made by the CERN NA51 experiment [10]. The acceptance of the NA51 toroid-based detector was such that the average rapidity $\langle y \rangle = 0$ and $x_1 = x_2 = 0.18$. Thus, the measurement was not reported as a function of x, but only at the average of x_2. The asymmetry extracted by NA51 was

$$A_{DY} = 2\frac{\sigma^{pp}}{\sigma^{pd}} - 1 = \frac{\sigma^{pp}-\sigma^{pn}}{\sigma^{pp}+\sigma^{pn}} = -0.09 \pm 0.02\,(\text{stat.}) \pm 0.025\,(\text{syst.}), \tag{2.3.6}$$

with the second equality only valid if nuclear effects are ignored. From this, the NA51 collaboration extracted

$$\left.\frac{\bar{u}(x)}{\bar{d}(x)}\right|_{x=0.18} = 0.51 \pm 0.04\,(\text{stat.}) \pm 0.05\,(\text{syst.})\,, \tag{2.3.7}$$

which is a clear signal for isospin symmetry violation in the sea antiquark distributions in accordance with the NMC result.

The E866/NuSea Experiment at Fermilab

The Fermilab E866/NuSea experiment used the Drell-Yan process to measure the x-dependence of the $\bar{d}/\bar{u}$ ratio. The spectrometer of the E866/NuSea experiment was composed of three dipole magnets. The first two magnets served to focus large transverse momentum, p_T, dimuons into the spectrometer. The third magnet provided a momentum measurement of the individual muons. The experiment used 800 GeV protons extracted from the Fermilab Tevatron incident on hydrogen and deuterium targets. The remainder of the beam which did not interact in the targets was intercepted by a copper beam dump contained within the first magnet. Additionally, the entire aperture of the first dipole was filled with copper, carbon and borated polyethylene, absorbing essentially all particles other than muons produced in the interaction of the beam with the targets or beam dump. E866/NuSea recorded 360,000 Drell-Yan events, approximately two thirds from a deuterium target and the remainder from a hydrogen target. The ratio of Drell-Yan cross sections, $\sigma^{pd}/2\sigma^{pp}$ (shown in Figure 2.12), measured by E866/NuSea as well as the extracted ratio $\bar{d}(x)/\bar{u}(x)$ is shown in Figure 2.13. When these measured cross section ratios were included in global parton distribution fits [11, 20, 16], the perception of the sea quark distributions in the nucleon was completely changed.

The E866/NuSea data present an interesting picture of the sea quark distributions of the nucleon that may shed some light on the origins of the sea quarks. At moderate values of x the data show greater than 60% excess of $\bar{d}$ over $\bar{u}$, but as x grows larger, this excess disappears and the sea appears to be symmetric again. A striking feature in Figure 2.13 is the return to a symmetric sea which is seen as $x \to 0.3$. The E866/NuSea data become less precise as x increases beyond 0.25 and the exact trend of $\bar{d}/\bar{u}$ is not clear. In determining the antiquark content of the proton sea, the parton distribution fits have simply parameterized the E866 data with a convenient algebraic form. While the chosen form reproduces the Drell-Yan data well, the statistical uncertainty on the data still allows for up to a 50% variation at

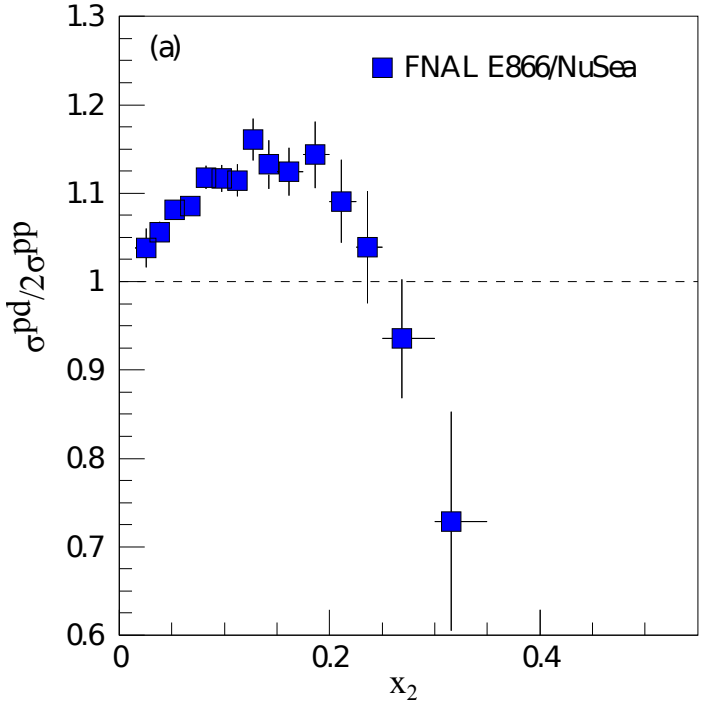

Figure 2.12: The blue squares show the ratio of the proton-deuterium to twice the proton-proton Drell-Yan cross sections versus x_2 as measured by Fermilab E866/NuSea [9].

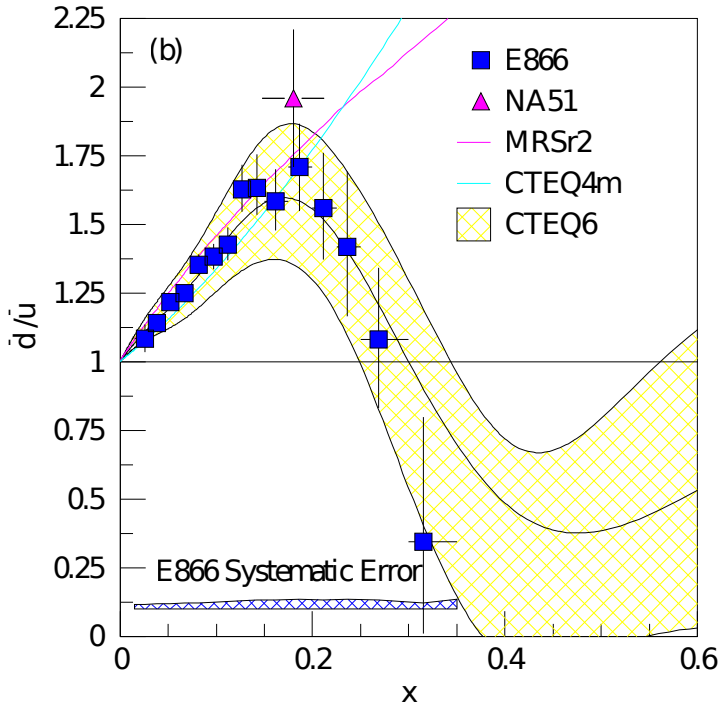

Figure 2.13: The blue squares show the $\bar{d}(x)/\bar{u}(x)$ ratio extracted by E866/NuSea [9]. The magenta triangle is the NA51 [10] measurement of $\bar{d}/\bar{u}$. The central curve in the cross filled band shows the $\bar{d}/\bar{u}$ ratio from the CTEQ6m fit [11], which included the E866/NuSea data, and the band represents the uncertainty from the fit. The curves labeled CTEQ4M [12] and MRS(r2) [13] show the parameterizations of $\bar{d}(x)/\bar{u}(x)$ which included the NA51 point and the NMC integral but not the E866/NuSea data.

$x = 0.3$ compared with only a few percent uncertainty at $x = 0.04$.

2.3.2 Models for the Flavor Asymmetry

In the following lines, models which are eventually able to explain the observed $\bar{d}/\bar{u}$ asymmetries are presented. It is important to note that none of the models can reproduce the asymmetries shown in 2.13 so far. For the discussion of potential models, the difference $\bar{d} - \bar{u}$ is very suitable. The $\bar{d} - \bar{u}$ difference, shown in Figure 2.14, is a pure flavor non-singlet quantity: its integral is Q^2 independent [45] and its Q^2 evolution at leading order does not depend on the gluon distribution in the proton. Early expectations were that Pauli blocking due to the extra valence u quark in the proton would lead to a suppression of $g \to u\bar{u}$ which would contribute significantly to differences in the light sea [46]. In perturbative QCD, differences between the $\bar{d}(x)$ and $\bar{u}(x)$ distributions arise only at second order and are calculated to be very small [47, 48, 49]. The large differences seen in Figures 2.12 ,2.13 and 2.14 must be non-perturbative in nature and can possibly be explained in terms of collective degrees of freedom of QCD at low energy.

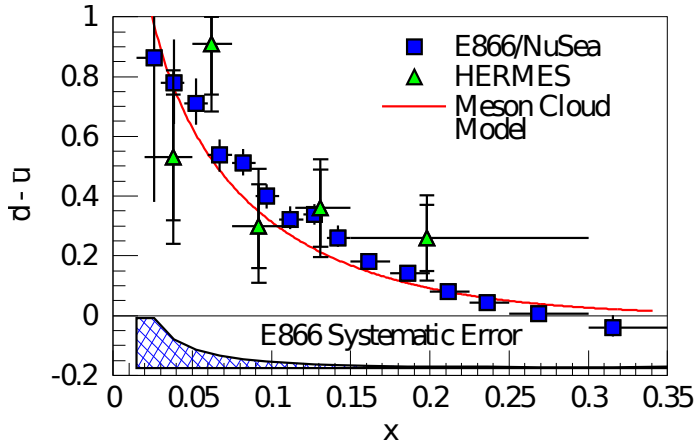

Figure 2.14: The $\bar{d} - \bar{u}$ distribution as extracted by E866/NuSea (blue squares) using Drell-Yan [9] and by HERMES (green triangles) using semi-inclusive DIS [50]. Also shown are a pion model calculation of Peng et al. [44] based on the procedure of Kumano [51].

The three most important non-perturbative approaches that can explain large differences in $\bar{d} - \bar{u}$ are:

1. hadronic models of the meson cloud of the nucleon
2. chiral quark models which couple mesons directly to constituent quarks [52, 53] and

3. instanton models [54, 55].

An interesting feature is that in each of these models the flavor and spin distributions of the proton are linked. As these non-perturbative models are considered, it is important to remember that they must be combined with perturbative sources to generate the entire quark sea of the proton. All these models can explain a large asymmetry, but not the return to a symmetric sea which is seen as $x \to 0.3$. In the following, only the pion cloud model is discussed in detail, since it is the only one at the moment which reproduces the measured $\bar{d} - \bar{u}$ satisfyingly well (see the red line in Figure 2.14).

The pion cloud model has a tantalizing simplicity and does explain the basic features of the data. The basic assumption is to expand the proton wave function containing virtual pion Fock states. The physical proton contains many virtual meson-baryon components, and the valence antiquark in the meson can contribute to the antiquark distributions in the proton sea:

$$|p\rangle_{phys} = Z^{1/2}|p\rangle_{bare} + f_{\pi^0 p}|\pi^0 p\rangle + f_{\pi^+ n}|\pi^+\rangle|n\rangle + f_{\pi^- \Delta^{++}}|\pi^-\rangle|\Delta^{++}\rangle + \ldots, \tag{2.3.8}$$

where $Z^{1/2}$ is the renormalization constant for the wave function, f_{MB} stands for the amplitude of Fock component containing a meson M (=$\pi, \rho, \ldots$) and a baryon B (=$p, n, \Delta, \ldots$) and $|p\rangle_{bare}$ is the bare baryon state. Note that the pion cloud provides the largest contribution because of its small mass. Since the probability of the $\pi^+ - n$ Fock component is larger than that of the $\pi^- \Delta^{++}$ state in the proton p, a surplus of d quarks is naturally explained in the meson cloud model.

The difficulty in this approach is finding justification to truncate the hadronic expansion [56]. Most calculations include contributions for $N\pi$ and $\Delta\pi$ states (see e.g. [57]). The pion-nucleon and pion-delta coupling constants ($g_{\pi NN}$ and $g_{\pi N\Delta}$) are well known, so the primary difference among calculations is the treatment of the πNN and $\pi N\Delta$ vertex factors. Using vertex functions (dipole vertex functions with cut offs, Λ, of $\Lambda_{\pi NN} = 1.0\,\mathrm{GeV}$ and $\Lambda_{\pi N\Delta} = 0.8\,\mathrm{GeV}$) reasonable agreement with the data [9] is found as shown in the solid red curve in Figure 2.14. The resulting probabilities for the $|N\pi >$ and $|\Delta\pi >$ admixture lead to a prediction for the difference in total spin carried by the u quarks (Δu) and the d quarks (Δd), $\Delta u - \Delta d = G_A$ of approximately 1.5 [44], providing a part of the reduction from the quark model value of $5/3$.

As mentioned earlier, none of these models consistently incorporate the flavor

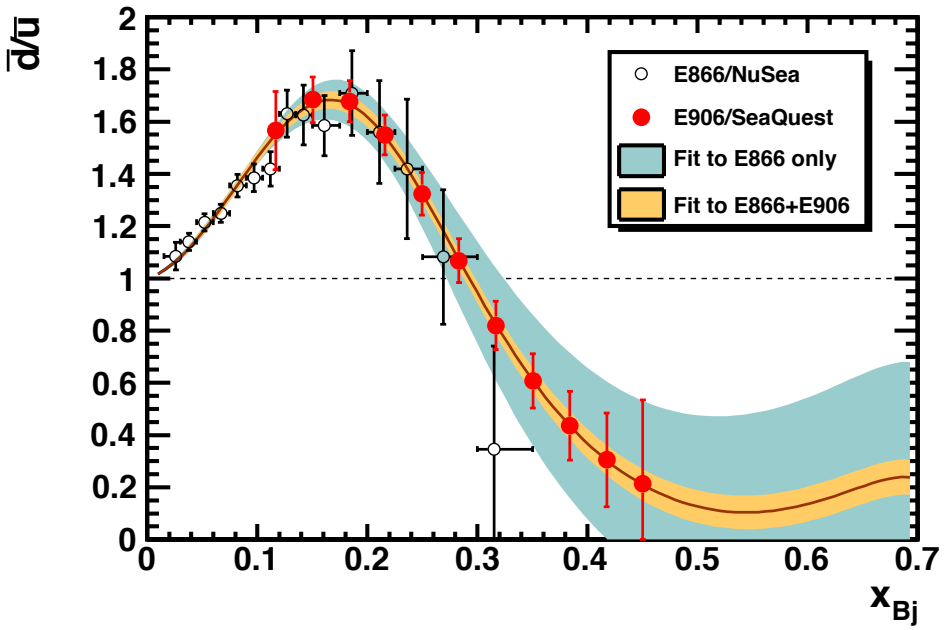

Figure 2.15: Expected accuracy of $\bar{d}/\bar{u}$ measurement by SeaQuest experiment. The data from E866/NuSea are also shown. The fits have been determined in NLO with the PDF set provided by MSTW2008 [32]. In each bin in x the expected average kinematics evaluated by GEANT Monte Carlo have been evaluated and used as a scale for the NLO fit [59]. The blue band shows the uncertainty of the fit based on E866 data points only, the yellow band shows the uncertainty of a combined fit of both E866 data points and expected SeaQuest data points.

symmetric sea. Consequently all the models substantially overpredict the ratio of $\bar{d}(x)/\bar{u}(x)$ for $x > 0.23$. Unfortunately the statistical uncertainty on the E866 data becomes large in this region. The pion models tend to level off at a predicted non-perturbative $\bar{d}(x)/\bar{u}(x)$ between 1.5 and 5 (depending on the baryons and mesons included in the calculations) until $x > 0.5$ where the ratio begins to decrease slowly to unity. One possible interpretation of the E886 results is that the perturbative gluon mechanism begins to establish its dominance over the non-perturbative mechanisms at a lower value of x than previously expected, indicating a larger gluon component in the proton. The gluon distribution at high x is, at present, poorly constrained, with uncertainties of $30-40\%$ at $x = 0.4$ [11, 58].

2.3.3 Motivation for the SeaQuest Experiment

E906/SeaQuest experiment at Fermilab was planned after the E866/NuSea experiment at Fermilab. The E866 experiment measured the target x dependence of $\bar{d}(x)/\bar{u}(x)$ at $0.015 < x < 0.35$. From the result of E866 experiment, Figure 2.15 , the ratio of $\bar{d}(x)/\bar{u}(x)$ is as large as 1.7. Also, the ratio seems to be smaller than 1 at high $x > 0.3$ although it is not yet conclusive due to the limited statistical accuracy. These are indication of new characteristics of the proton structure, since no theoretical models can reproduce this behavior at all. Although there are some theoretical models for the ratio of $\bar{d}(x)/\bar{u}(x)$ (see details in the previous subsection). But all the models predict that the ratio is always larger than 1 in the complete Bjorken x range. So, it is very important to measure the ratio at high Bjorken x. Therefore, the SeaQuest is designed and optimized to measure the ratio $\bar{d}/\bar{u}$ at $0.1 < x < 0.45$ with high precision. This x region was selected so that the uncertainties on the $\bar{d}(x)/\bar{u}(x)$ can be less than 0.2.

SeaQuest uses a 120 GeV proton beam from the Main Injector at Fermilab to measure the ratio of $\bar{d}(x)/\bar{u}(x)$ at a high Bjorken x, while the E866 experiment used a 800 GeV proton beam from the Tevatron accelerator at Fermilab. In the following paragraph the two main benefits of using a lower beam energy are discussed.

First, for the lower beam energy used at SeaQuest, the Drell-Yan cross section for fixed x_1 and x_2, is proportional to $1/E_{Beam}$ where E_{Beam} is the incident beam energy as shown in Eq. (2.2.3). A 120 GeV Main Injector experiment has a 7 times larger cross section compared with the previous E866 experiment which used the 800 GeV beam.

Second, practical limitations in the acceptable luminosity for these experiments are radiation protection limits and the single muon rates in the detectors. To the extent that the radiation dose scales as beam power (beam energy times beam intensity), one can take approximately 7 times the luminosity for the same beam power at 120 GeV relative to the 800 GeV case. In the E866 experiment at 800 GeV, J/ψ events from the beam dump were the most significant contribution to the muon singles rates. At 120 GeV the total J/ψ production cross section is smaller by an order of magnitude when compared with 800 GeV.

The combination of these two effects is expected to increase the number of recorded events by a factor 50 at high x_2 in comparison with the previous Drell-Yan experiment. SeaQuest is the only proton-nucleon Drell-Yan experiment in the world taking data at the moment.

In Figure 2.15, the expected improvement in the determination of $\bar{d}/\bar{u}$ at SeaQuest

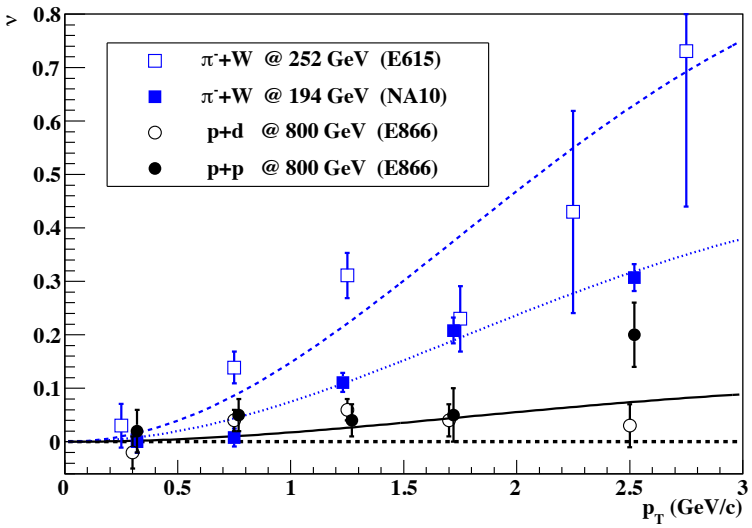

Figure 2.16: Overview of past Drell-Yan measuremenst of ν performed bt by CERN NA10 [60, 61], Fermilab E615 [62] and proton induced Drell-Yan by Fermilab E866/NuSea [63]. The lines are fits to are scale-dependent QCD-contribution to the asymmetry (for details see original paper).

compared to the E866 measurement can be seen. The fits have been determined in NLO with the PDF set provided by MSTW2008 [32]. In each bin in x the expected average kinematics evaluated by GEANT Monte Carlo have been evaluated and used as a scale for each bin in the NLO fit [59].

2.4 Angular Distributions of Muon Pairs

In leading order, ignoring transverse momenta k_T of the interacting partons, the Drell-Yan angular distribution is naively expected to have the form $(1+\cos^2\theta)$ (cf. Figure 2.9). More generally, Collins and Soper [41] have shown that the expression for the angular distribution is

$$\frac{d\sigma}{d\Omega} \propto 1 + \lambda \cos^2\theta + \mu \sin 2\theta \cos\phi + \frac{\nu}{2} \sin^2\theta \cos^2\phi, \tag{2.4.1}$$

where θ is the polar angle of the positive lepton in the rest frame of the virtual photon and ϕ is the azimuthal angle. The additional terms arise from the k_T of the interacting partons and higher order graphs in α_S. After consideration of the intrinsic k_T of the partons, care must be taken in precisely defining the z-axis of rest frame of the virtual photon. The most common choices for this definition are the u-channel frame where the z-axis points anti-parallel to the target nucleon direction;

the Gottfried-Jackson frame (t-channel) [64] has the z-axis pointing parallel to the beam nucleon and the Collins-Soper [41] frame where the z-axis bisects the angle between the u-channel and Gottfried-Jackson z-axes, in an attempt to minimize the effects of k_T on the observed angular distributions. The transformation between λ, μ and ν in the three frames is shown in [62].

In NLO, a relationship between λ and ν of the general angular distribution in Eq. (2.4.1) was derived by Lam and Tung [65]. In analogy to the Callan-Gross relationship of DIS [27] (cf. Eq. (2.1.23)), the Lam-Tung relation states that

$$1 - \lambda = 2\nu \tag{2.4.2}$$

Unlike the Callan-Gross relation, the Lam-Tung relation is expected to be largely unaffected by QCD [65].

The validity of the Lam-Tung relation has been studied with both pion-induced Drell-Yan by CERN NA10 [60, 61] and Fermilab E615 [62] and proton induced Drell-Yan by Fermilab E866/NuSea [63]. A summery of the measurements on the ν coefficient can be seen in Figure 2.16. Pionic Drell-Yan experiments have observed a violation of the Lam-Tung relation. This violation is most prominent at high transverse momentum of the di-lepton, p_T , where ν rises without a corresponding decrease in λ. The violation appears to be independent of the target nucleus [60]. In contrast, the Fermilab E866 proton induced Drell-Yan data are consistent with the Lam-Tung relation, even at high-pT [63].

An explanation proposed by Boer [67] is based on the existence of a chiral-odd, T-odd distribution function, $h_1^{\perp}(x,k_T)$, with an intrinsic transverse momentum dependence of Boer and Mulders [68]. This distribution function is an analog of the Collins fragmentation function [69]. It represents the correlation of the parton's transverse spin and k_T in an unpolarized nucleon. Boer argues that the presence of the $h_1^{\perp}(x,k_T)$ distribution function induces a $\cos 2\phi$ dependence to the Drell-Yan cross section and fits the observed NA10 [61] data to a crude model of this distribution function. Within a quark spectator-antiquark model, it has been shown that the observed $\cos 2\phi$ distribution can be reproduced with nonzero $h_1^{\perp}(x,k_T)$ in both the pion and target nucleon [70].

When considering any of these explanations for the violation of the Lam-Tung relation in pion-induced Drell-Yan, it is important to remember that these results must be reconciled with the apparent absence of a violation in proton-induced Drell-Yan. One significant difference is that the valence antiquark in the pion-induced case allows the experiment to probe the quark distributions of the target, while in

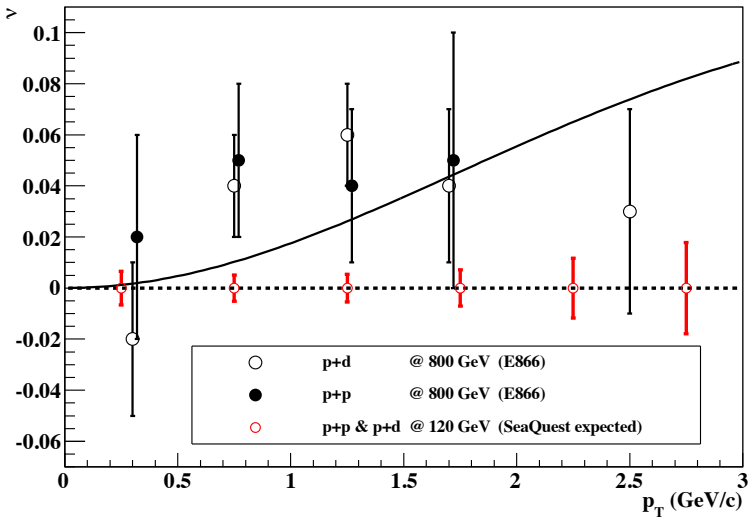

Figure 2.17: A comparison between the E866/NuSea measurement on the ν vs p_T and the expected accuracy on the same measurement at SeaQuest [66].

the proton induced case, only the target antiquark distributions are probed. Alternatively, the possible interpretation as a higher-twist effect might have a kinematic dependence on $\sqrt{s}$. The pionic data had $\sqrt{s} = 11\,\text{GeV}$ and $16\,\text{GeV}$ while the proton data had $\sqrt{s} = 39\,\text{GeV}$. Such an effect should clearly be seen then in the SeaQuest experiment with proton-induced Drell-Yan at $\sqrt{s} = 15\,\text{GeV}$. The expected accuracy of the future measurement of the ν of SeaQuest is shown in Figure 2.17 [66].

2.5 Required Experimental Acceptance

In order to achieve the physics goals of the SeaQuest experiment presented in this chapter a few requirements on the acceptance need to be done. First, the spectrometer must be capable to record Drell-Yan dimuons in the range between $4.0\,\text{GeV/c}^2$ and $7.0\,\text{GeV/c}^2$. This mass range is exactly between the two main sources of background: the J/ψ resonance at $3.1\,\text{GeV/c}^2$ and the Υ-resonance at $9.5\,\text{GeV/c}^2$. The SeaQuest spectrometer's mass resolution is designed to identify these two resonance peaks. Figure 2.18 shows the accepted Drell-Yan range as yellow band. The mass spectrum in the Figure 2.18 was produced by a GEANT4 based Drell-Yan only Monte-Carlo simulation which takes the SeaQuest acceptance into account.

Second, the SeaQuest spectrometer must select high values x_{Beam} and low values x_{Target} (cf. Equation (2.3.5)). Figure 2.19 shows the two-dimensional distribution of x_{Target} vs. x_{Beam}. The hyperbolic curves shown in the figure correspond to the

mass of J/ψ and Υ. The linear function in the figure is the line of $x_{\mathrm{Beam}} = x_{\mathrm{Target}}$. A significant fraction of events satisfies the condition $x_{\mathrm{Beam}} > x_{\mathrm{Target}}$.

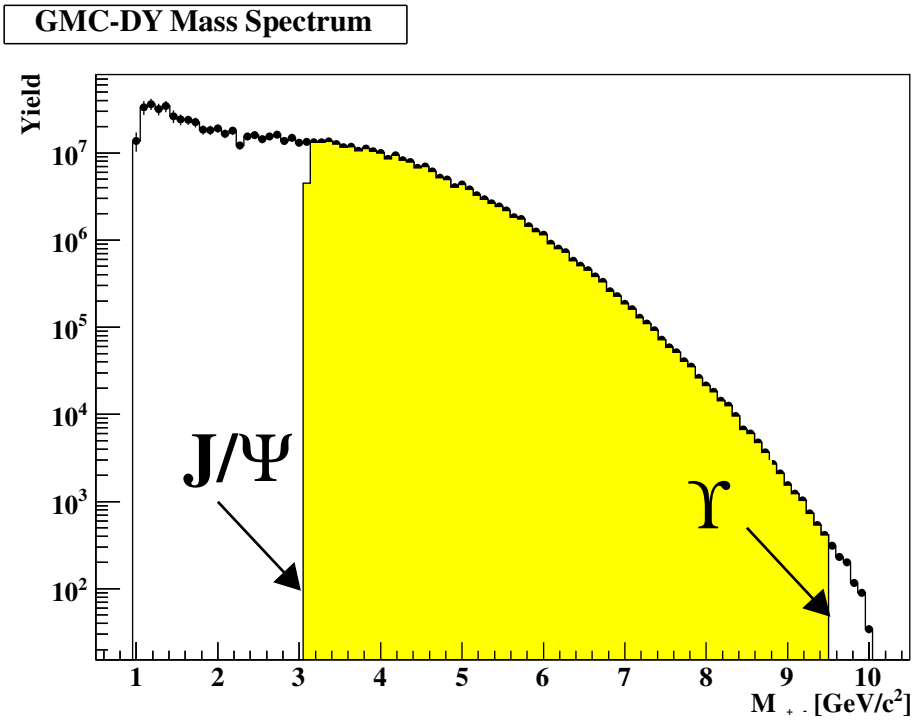

Figure 2.18: The dimuon mass distribution generated by a GEANT4 Monte-Carlo. The spectrum is a continuous Drell-Yan mass spectrum. Thus, the positions of the J/ψ and Υ resonances are indicated by the tips of the arrows. The yellow band shows the mass range of the the Drell-Yan dimuons which will be used for the physics program of SeaQuest.

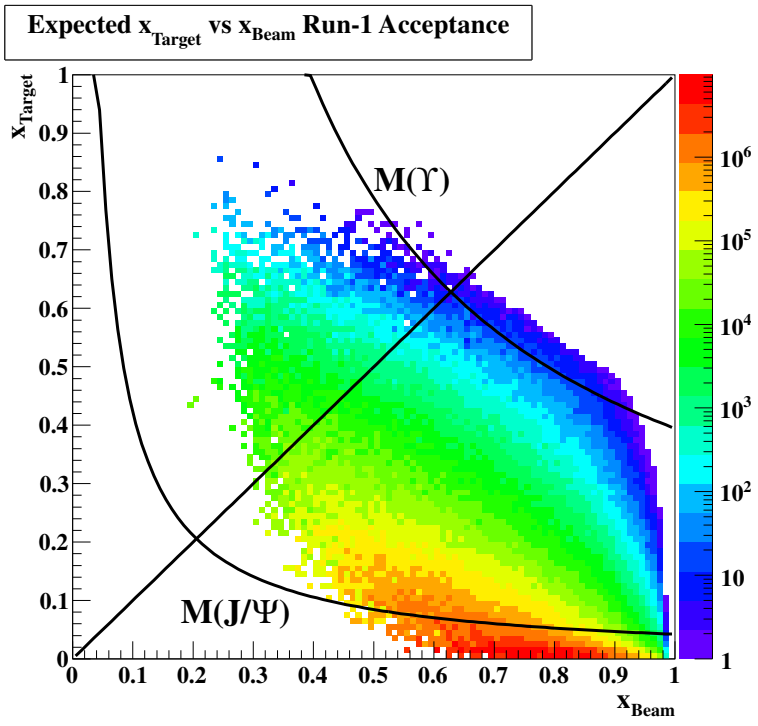

Figure 2.19: Kinematic plane x_{Target} vs. $x_{\text{Beam}}$of the SeaQuest experiment. The hyperbolic curves which correspond to masses of J/Ψ and Υ. The linear function is the line of $x_{\text{Beam}} = x_{\text{Target}}$.

Chapter 3

The SeaQuest Experiment

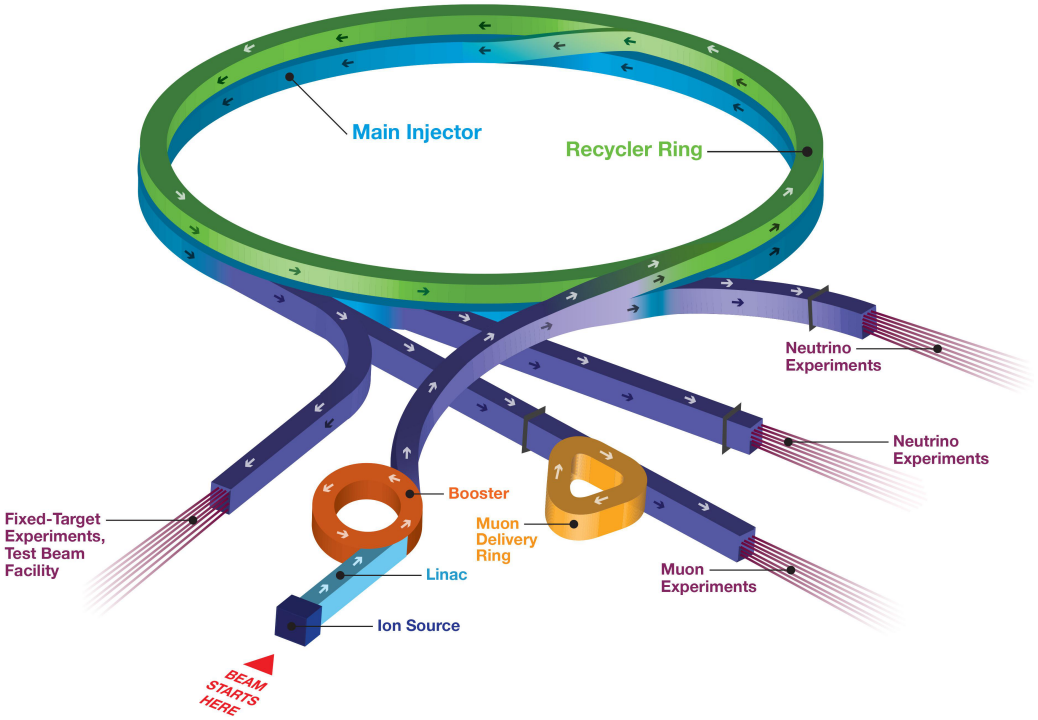

Figure 3.1: The Fermilab Main Injector Complex.

The SeaQuest experiment is located in the Neutrino-Muon (NM) fixed-target beam-line at Fermilab. SeaQuest is a fixed-target experiment. Neutrino oscillation experiments are also fixed target experiments. At Fermilab the collider experiments of CDF and D0 were carried out until September 2011. The Fermilab accelerator chain, which includes the Tevatron and fixed-target beamline, is depicted in Figure 3.1. For SeaQuest, the proton beam is extracted from the Main Injector to a volume of target material. The proton beam interacting with the target material produces

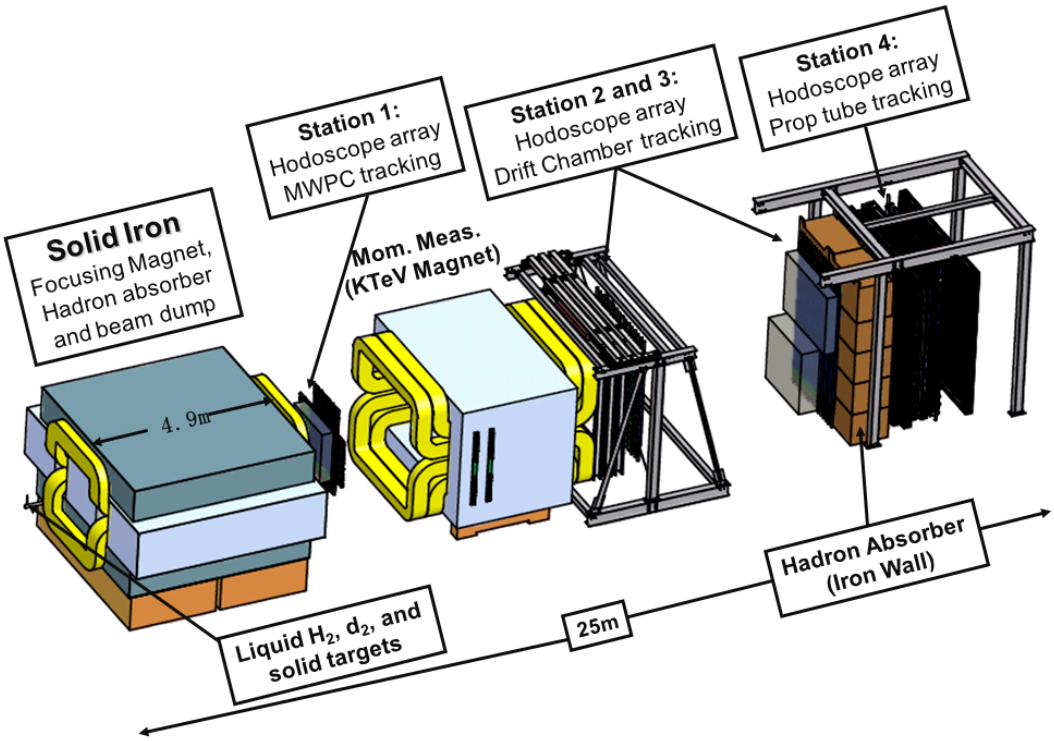

Figure 3.2: The SeaQuest charged particle spectrometer in its Run 1 configuration in 2012. Illustration from [71].

different daughter particles, which are selectively filtered dependent on the purpose of study.

The SeaQuest Spectrometer, as depicted in Figure 3.2, employs four Chambers for tracking and an Analyzer Magnet to measure the momenta and trajectories of charged particles from proton-nucleon collisions. The spectrometer measures momenta by recording the bend of a charged particle as it passed through a known magnetic field. One can find the initial trajectory of a given charged particle through the spectrometer by measuring the positions of a track in the two upstream drift chambers. The final trajectory of a charged particle is given through measuring the position of a track in the downstream drift chambers as well. One can then extract the momentum of the charged particle by taking the quotient of the p_T-kick from the magnetic field with the change in track direction.

The SeaQuest spectrometer was designed to detect oppositely-charged muon pairs while minimizing sensitivity to everything else. The coordinate system of the spectrometer was defined in the following way: the z-axis of the spectrometer was parallel to the nominal direction of the beam; the x-axis laid parallel to the floor of the experimental hall, pointing to the left when facing the downstream of

the beam; the y-axis then forms the right-handed Cartesian coordinate system by pointing upward. The origin of the coordinate system, $(x,y,z) = (0,0,0)$,was chosen as the center of the upstream face of FMAG, the upstream dipole magnet.

3.1 The Fermilab Main Injector Beam

An important element for the beam is the Main Injector where protons can be accelerated to energies up to 120 GeV. This acceleration occurred over a span of 55 seconds and is called the 'off-spill' period. The period after acceleration, in which the protons are continuously delivered to the NM beamline, is called the 'on-spill' period. The on-spill period lasts for approximately 5 seconds in every minute during the 2012 commissioning run.

The Main Injector is operated at a 53.1 MHz radio-frequency (RF) and can hold up to 588 RF buckets in its ring. The booster fills $1/7$ of the ring, or 84 RF buckets, at a time. Therefore, seven booster batches are required to fill the ring. It is important to note that depending on the run condition, the accelerator operations department can choose to leave out certain RF buckets, and even entire booster batches, empty for the purpose of achieving an appropriate tune. This gives the proton beam a micro-structure in addition to the spill macro-structure described in the previous paragraph. Essentially, the protons arrive in $1-2$ns pulses spaced by 18.9 ns, where each pulse is known as an RF Bucket. The design intensity of protons delivered to the NM beamline is 2×10^{12} protons/second and therefor 1×10^{13} protons per spill. The typical intensity which was used for the commissioning run in April and May 2012 at SeaQuest were between 1×10^{10} and 1×10^{12} protons per spill. Details of the micro structure of the beam can be found in Figure 3.3.

The proton beam was focused to a transverse width of less than 250 μm before striking the target. The beam spot on the target was approximately 6 mm wide by 1 mm high during the experiment. A two-way split divided the proton beam between the NM4 hall and the test beam facility within the fixed target extraction lines. The position, size and intensity of the beam were constantly monitored at various points along the beam line by several detectors. Several beamline detectors and monitors were used in order to monitor the beam intensity, position, and beam-spot size. The beam intensity was monitored by an ion chamber located in the NM3 sector (NM3IC). Both the size and the position of the beam were monitored by segmented wire ion chambers (SWICs) and Beam-Position Monitors (BPMs), the ones closest to the spectrometer were located in the NM2 (NMWC1 and NMWC2, NM2HBPM

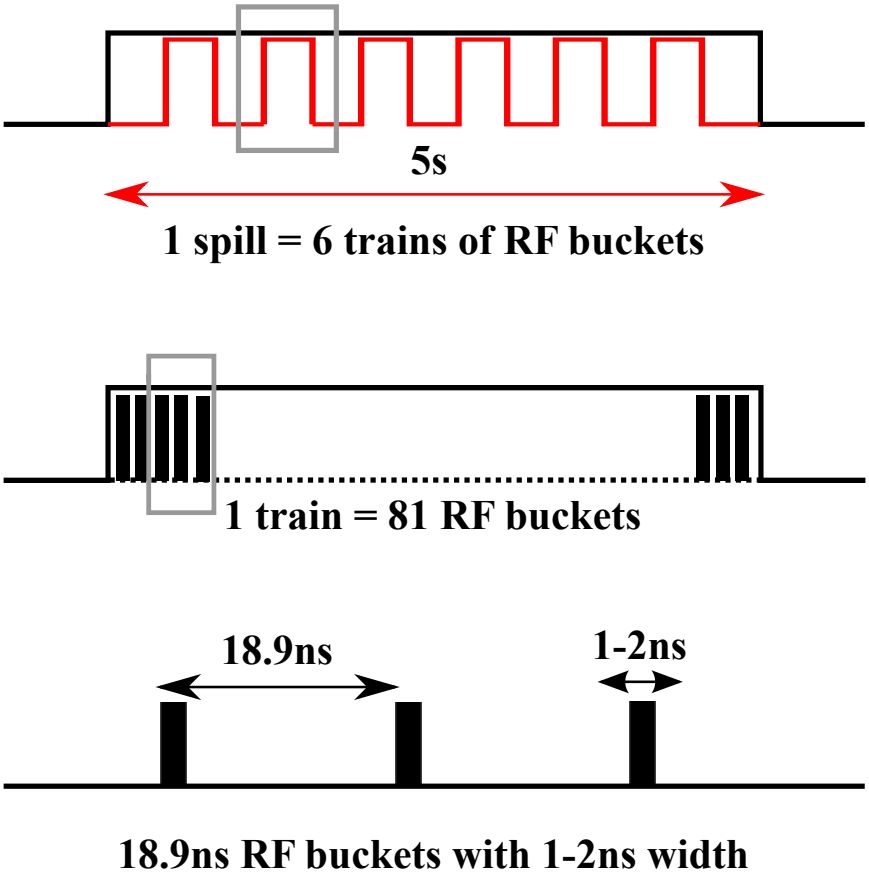

Figure 3.3: The micro structure of the Main Injector Beam arriving at the SeaQuest experiment

and NM2VPM).

3.2 Targets

The targets used in the SeaQuest experiment consist of 50.8 cm (20 inch) long liquid hydrogen and deuterium targets, three nuclear targets (carbon, calcium, and tungsten) and a dummy (empty) liquid target cell which is used for normalization purposes. The nuclear targets are used to investigate the nuclear dependence of the Drell-Yan process and the partonic energy loss in nuclei. The dimension of the six targets corresponds to 15% the of the interaction length L_I of the material. The geometrical dimensions of the target cells was optimized to minimize secondary reactions inside the target. 10^{13} protons are delivered to the target every minute in a 5 s slow extraction spill.

The different targets are mounted on a movable table so that they can be exchanged between the spills of the beam. The exchange process takes only 30 sec-

onds. This 30 seconds interval allows an exchange between every spill, since the interval between spills is 55 seconds. The beamtime assignment for the between different targets will be such that the hydrogen targets will be in the beam 35% of the time, deuterium 26%, the dummy liquid cell 4%, and the nuclear targets 35% (evenly split between three different nuclear targets).

A set of four switches on the target table are engaged by a stationary roller mounted in front of the table. The positions of these switches correspond to the beam striking the center of each of the targets, plus a fourth position where the target does not exist. When engaged, each switch completed a circuit which can be read out by the DAQ, recording which target is in the beam. The switches are also tied into the beam interlock system which requires that one of the four switches to be engaged for the beam to be allowed to enter the target area. This ensures that the beam would not be able to hit the sides of the target flasks and cause a radiation hazard.

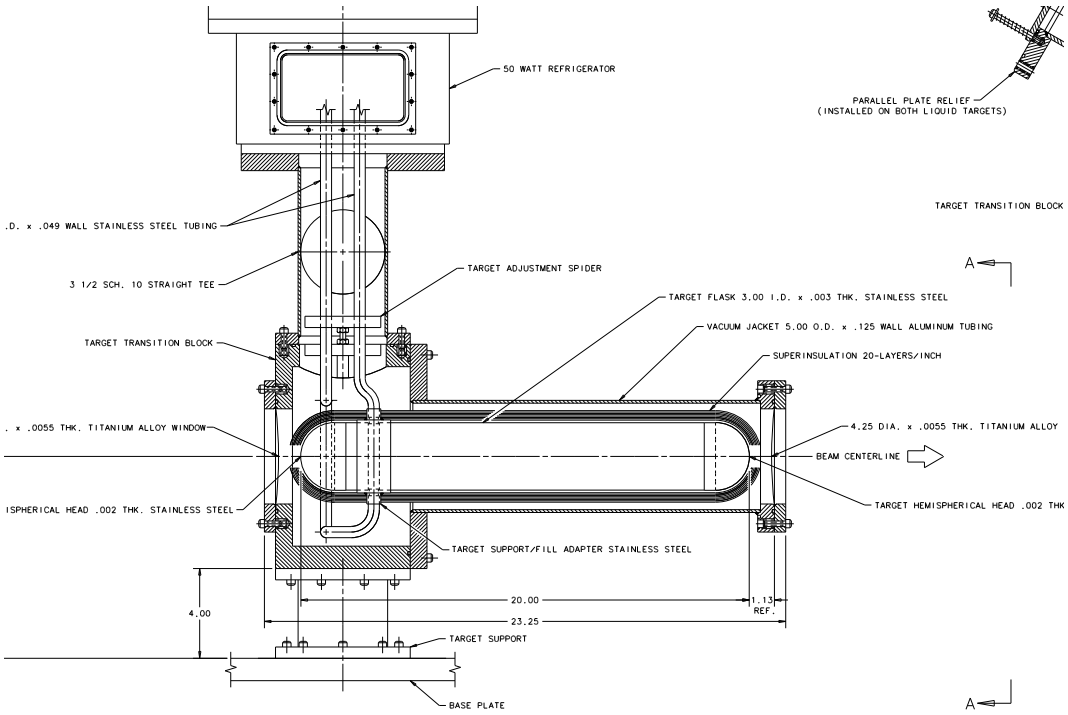

Figure 3.4: Cross section of one of the three identical SeaQuest target flasks.

3.3 The Spectrometer Magnets: FMAG and KMAG

The first dipole magnet located most upstream is called “FMAG” (see Figure 3.6) whose aperture is 1.22 m in the x-direction and 66 cm in the y-direction. It is the

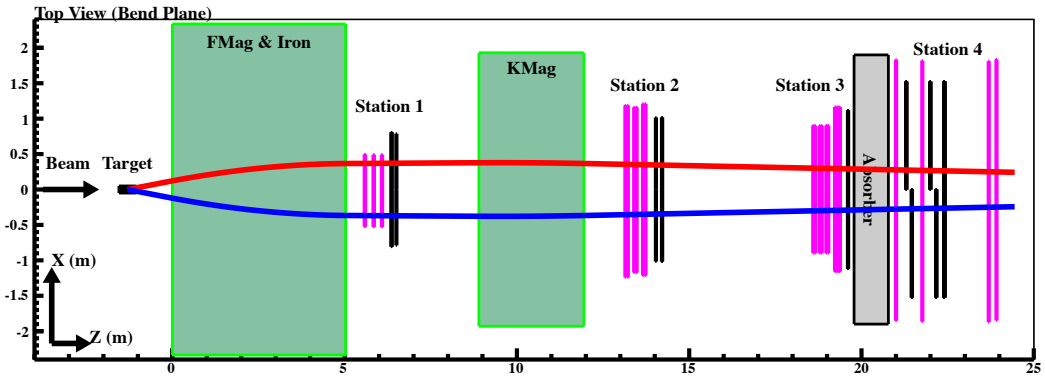

Figure 3.5: Cross section of one of the three identical SeaQuest target flasks.

electromagnetic di-pole magnet closest to the target. It focuses high transverse momentum muons into the apparatus' acceptance and bends low momentum muons out of the acceptance. The primary beam will stop in the beam dump inside FMAG. The beam dump is an iron block.

The second magnet is called "KMAG" (cf. Figure 3.7). It is the actual analyzer magnet used for the momentum measurement of charged muon tracks. It is an electromagnetic dipole that creates a field oriented in the +y-direction (vertical upward direction).

FMAG was set to 2000 Amperes and KMAG to 1600 Amperes during the commissioning period in 2012, delivering a transverse-momentum kick to relativistic charged particles in the x-z plane of 2.91GeV/c and 402 MeV/c, respectively. Both FMAG and KMAG bend muons in the $\pm$x-direction (horizontal direction) as shown in 3.5. A summary of the design values of the magnets can be found in Table 3.1.

3.4 Beam Dump and Hadron Absorber Wall

In order to prevent damage to the downstream detectors from the beam, the target is followed by a large, water-cooled beam dump whose upstream face is located at $z = 0$ m. The beam dump is made of solid iron and is 5 m in length. It is an equivalent of $\approx$ 35 nuclear interaction lengths of iron [72]. Its aperture is 2.86 m $\times$ 1.29 m. Inside the iron, there is a hole. Its diameter is 5 cm and it is 25 cm deep.

A hadron absorber wall is located between Station 3 and Station 4. The purpose of this wall is to identify muons at the rear of the apparatus. The only particles which can penetrate the absorber wall are muons. The absorber wall consists of 98 cm thick iron. This is an equivalent of $\approx$ 6 nuclear interaction lengths L_I of iron

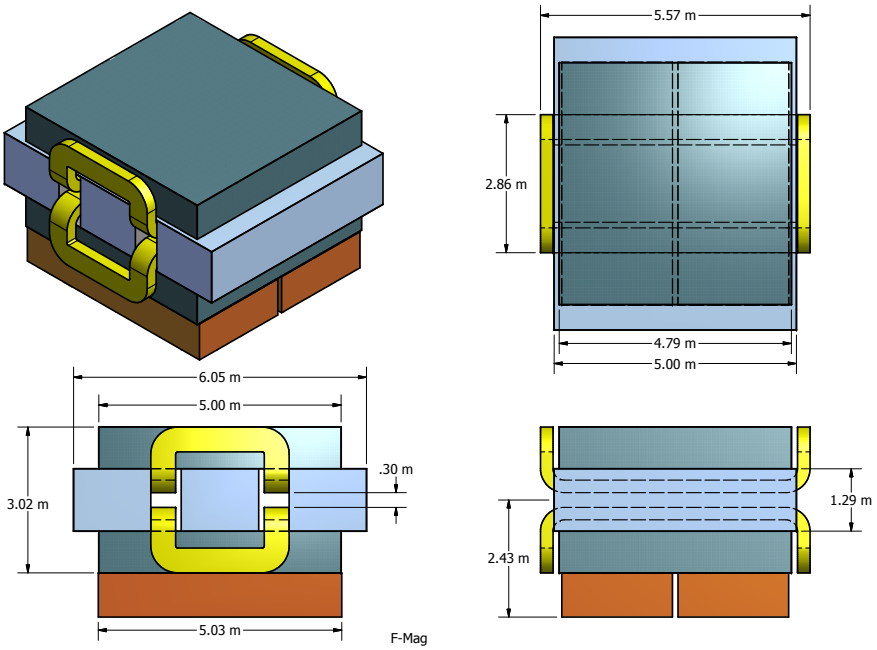

Figure 3.6: Summary of the geometrical dimensions of FMAG [71]. FMAG focuses high-p_T muns into the acceptance of the SeaQuest spectrometer. The solid iron filling the dipole magnet can be clearly seen. The SeaQuest track reconstruction has to account for the energy loss and multiple scattering occurring in the iron block.

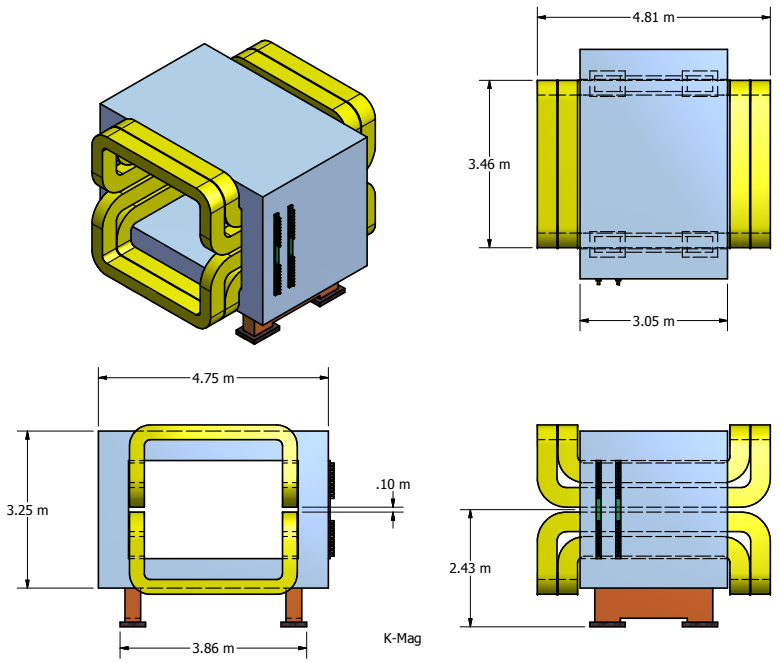

Figure 3.7: Summary of the geometrical dimensions of KMAG [71]. KMAG is the analyzer magnet at SeaQuest, determining the momenta of the muon tracks.

Property	FMAG	KMAG
Length	189”	211”
Width	95”	147”
Height	198”	198”
Horizontal Aperture	48”(123 cm)	63”(160 cm)
Vertical Aperture	26”(66 cm)	70”(178 cm)
Field Integral	8.14 Tm	3.0 Tm
Ampere-Turns	670,000	800,000
Current	2,400 A	4,200 A
Power	580 kW	400 kW
Inlet Power Temperature	38°	38°
Temperature Rise	38°	38°
Water Flow	90 gal/min	60 gal/min
Weight:		
Pole Inserts	9.5 t	10 t
Coils	19 t	40 t
Return Yoke	420 t	300 t
Total	450 t	350 t

Table 3.1: Summary of the design parameters of the upstream magnet FMAG and the downstream magnet KMAG.

[72].

Between the downstream face of FMAG and Station 1, a 2 cm thick wall of borated polyethylene is placed. This polyethylene acts as a moderator to slow down fast neutrons to thermal energies. It is thus used as a neutron shielding material in areas of low and intermediate neutron flux close to the target and beam dump region.

3.5 Detector Stations

Four detector stations are responsible for triggering on dimuon events and tracking the muons which traversed the spectrometer. The first three detector stations consisted of hodoscope- and drift chamber-planes, while station-4 consisted of hodoscope- and proportional-tube planes. The fast response time of the hodoscopes was utilized to trigger on events with the expected dimuon signature, at which point the slower responding drift chambers could be read out. The proportional-tubes and hodoscopes at station-4 were used to provide some position information to the trigger, and discriminate against any hadrons which made it through the absorber wall.

3.5.1 Scintillator Hodoscopes

Hodoscope planes were located at each of the four detector stations and were used to trigger on dimuon events. Each hodoscope plane was split into two half-planes (top and bottom, or left and right) of parallel scintillator paddles attached to photomultiplier tubes by plexiglass light guides. Station 1, 2 and 4 each had two hodoscope planes, with their paddles oriented in the x and y directions respectively. Station 3 had only one hodoscope plane, with its paddles oriented perpendicular to the floor. The hodoscope planes were named according to the tracking station they belonged to, preceded by “T” or “B” (“L” or “R”). H indicates horizontal paddles which measure Y position while V indicates vertical paddles which measure X position. For example, T, B, L and R stand for top, bottom, left and right. “H1T hodoscope” (“H1L hodoscope”) referre to the Station-1 hodoscope plane in which 23 (23) scintillator detectors were positioned horizontally on the top (left w.r.t. the beam direction) side. The detailed specifications of the eight hodoscope planes are given in Table 3.2. A precise alignment of the hodoscopes was achieved by examining the distributions of positions of muon tracks at each hodoscope plane when a given hodoscope in that plane was fired.

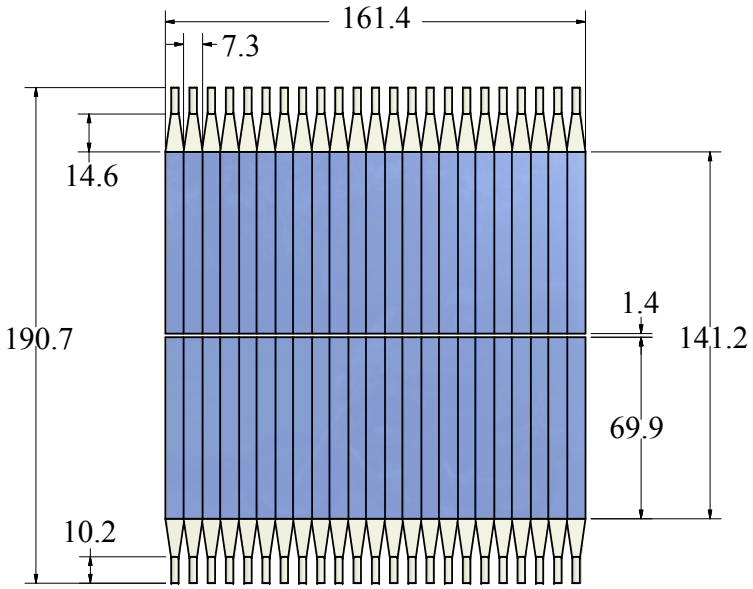

Hodoscope Array 1X

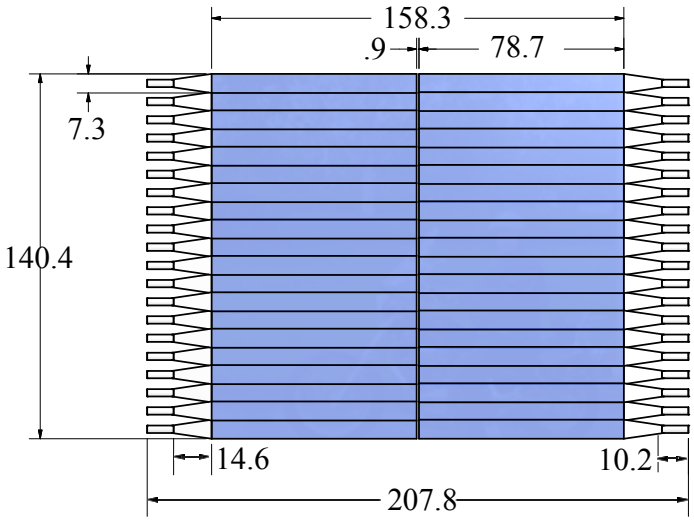

Hodoscope Array 1Y

Figure 3.8: Overview of the Station 1 Hodoscope paddle-arrays used in the SeaQuest experiment, X1 and Y1. During Run 1, only the X-hodoscopes were used for the trigger. Illustration from [71].

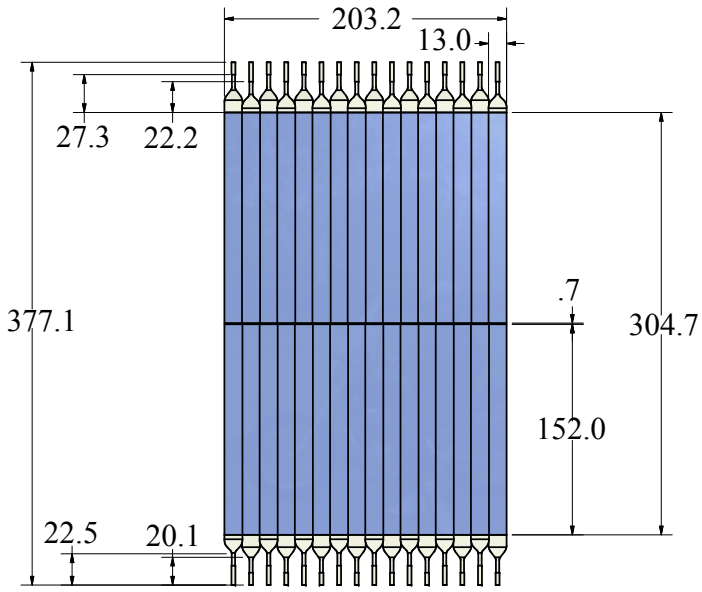

Hodoscope Array 2X

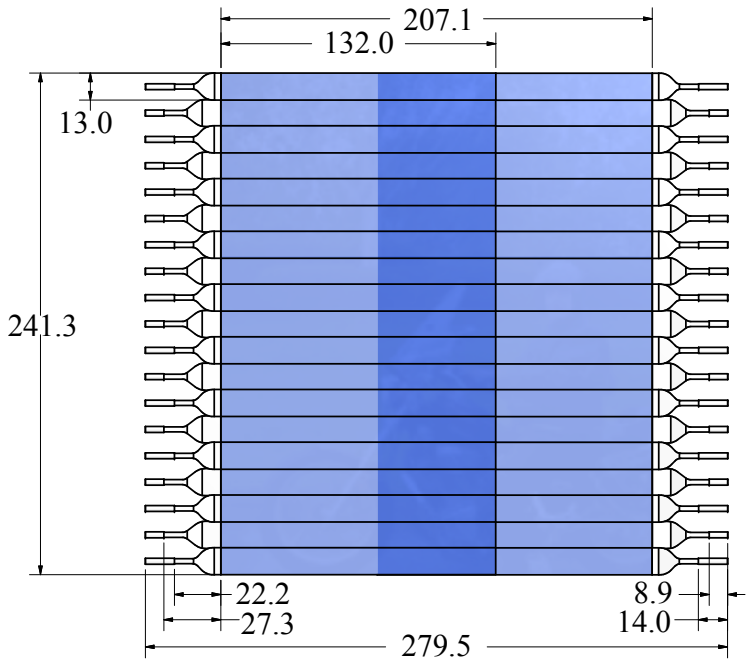

Hodoscope Array 2Y

Figure 3.9: Overview of the Station 2 Hodoscope paddle-arrays used in the SeaQuest experiment, 2X and 2Y. During Run 1, only the X-hodoscopes were used for the trigger. Illustration from [71].

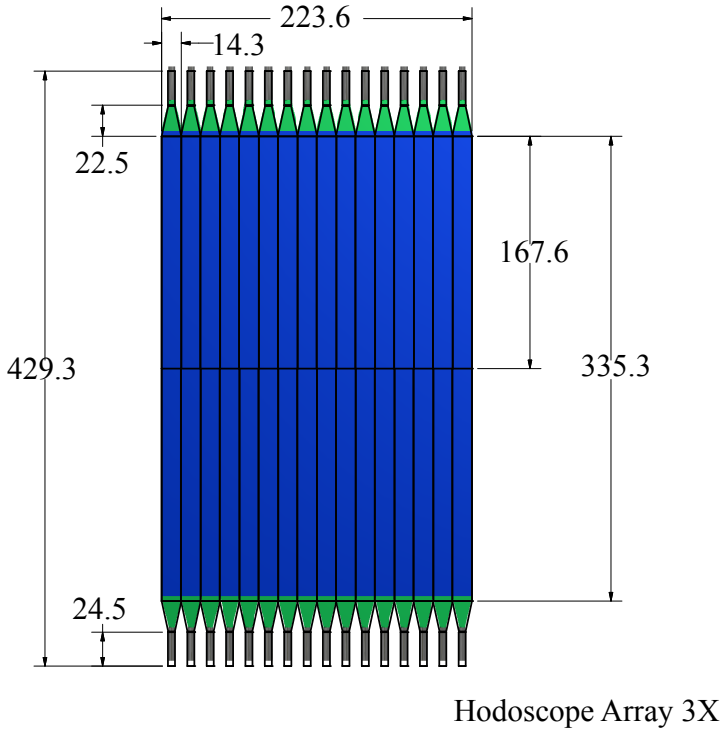

Figure 3.10: Overview of the Station 3 Hodoscope paddle-arrays used in the SeaQuest experiment, 3X. During Run 1, only the X-hodoscopes were used for the trigger. Illustration from [71].

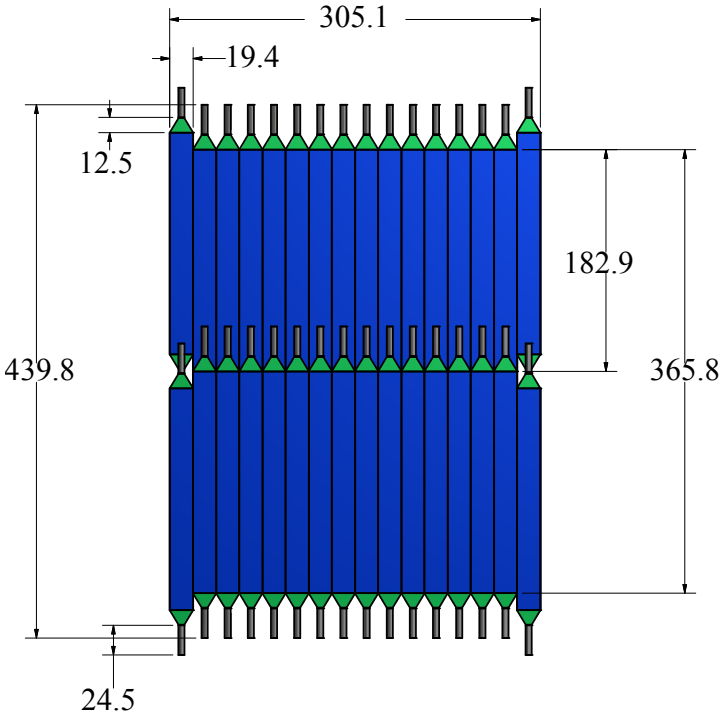

Figure 3.11: Overview of the Station 4 Hodoscope paddle-arrays used in the SeaQuest experiment, 4X and 4Y. During Run 1, only the X-hodoscopes were used for the trigger. Illustration from [71].

Detector	width [cm]	overlap [cm]	# of paddles	$x \times y$ [cm] $\times$ [cm]	z-position [cm]
H1T	7.3475	0.3175	23	162.008×69.85	636.27
H1B	7.3475	0.3175	23	162.008×69.85	636.27
H1L	6.9775	0.3175	20	78.74×133.518	650.24
H1R	7.3075	0.3175	20	78.74×140.117	650.24
H2T	13.0375	0.3175	16	203.838×120.65	1421.13
H2B	12.8875	0.3175	16	201.438×120.65	1421.13
H2L	13.0675	0.3175	19	101.6×242.568	1403.35
H2R	12.9375	0.3175	19	101.6×240.098	1403.35
H3T	14.5175	0.3175	16	227.518×167.64	1960.88
H3B	14.5175	0.3175	16	227.518×167.64	1960.88
H4T	19.33	0.317499	16	304.518×182.88	2240.28
H4B	19.33	0.317499	16	304.518×182.88	2240.28
H4Y1L	23.16	0.317501	16	152.4×365.797	2129.79
H4Y1R	23.16	0.317501	16	152.4×365.797	2146.3
H4Y2L	23.16	0.317501	16	152.4×365.797	2199.64
H4Y2R	23.16	0.317501	16	152.4×365.797	2216.78

Table 3.2: Overview of the hodoscope characteristics

3.5.2 Tracking Chambers

Each of the first three detector stations contained six drift-chamber planes, arranged in three pairs of planes with parallel wire orientations (referred to as "views"). Wires were oriented vertically in the "X" planes, and at an angle of $+14^\circ$ and -14° with respect to the X axis in the "V" and "U" planes, respectively. The wires in the second plane in each pair were offset by half the cell size of the drift chamber. The plane in each pair closest to the target was denoted as the "unprimed" plane, while the plane in the pair furthest from the target was denoted as the "primed" plane, as UU'XX'VV' for example. These planes provide information on the x- and y-intercept of the muon tracks at the detector station with redundant information about the y-position. Station 3 is split in a top half, denoted as Station 3 Plus, and a bottom half, denoted as Station-3 Minus.

Stations 1, 2 and 3 Minus were already used in the earlier E866 experiment. In order to prepare them for operation in the SeaQuest experiment, they were completely refurbished in the years 2010–2012, and new read-out electronics were attached to them. The drift chamber Station 3 Plus was newly constructed by the Japanese SeaQuest collaboration and was shipped form Japan to Fermilab. For the

second run of SeaQuest experiment Stations 3 Minus has been replaced by a new drift chamber. Station 1 will also be replaced with a new chamber.

During Run1 operation the drift chambers of Station 1, 2 and Plus were operated with a gas mixture of P08 (argonne:methane (80% : 20%)), while Station 3 Minus was operated with argonne : CO_2 (80% : 20%), mixed by volume at a constant temperature.

The anode wires at Station-1 were gold-plated tungsten wires. Stations 2 and 3 Minus used silver-coated beryllium-copper wires as anodes. All of the anodes are 25 μm in diameter. The cathode wires are all 62.5 μm silver-coated beryllium-copper wires. Typical drift velocities were $\approx 50\,\mu$m/ns. In Station3 Plus, the diameter of the sense wires was 30 μm, and they were made from gold-coated tungsten. All of the diameters of the cathode wires, the field wires and the guard wires were 80 μm and are made from Beryllium-Copper as well. The drift chambers were operated at voltages between 1700 and 2200 volts. Detailed Drift chamber specifications can be found in Table 3.3.

In Figures 3.13 - 3.16 the $|\vec{E}|$ and voltage distributions for the nominal voltages are shown. The field maps were evaluated with the Garfield software package, which is designed to simulate the properties of gaseous detectors [73].

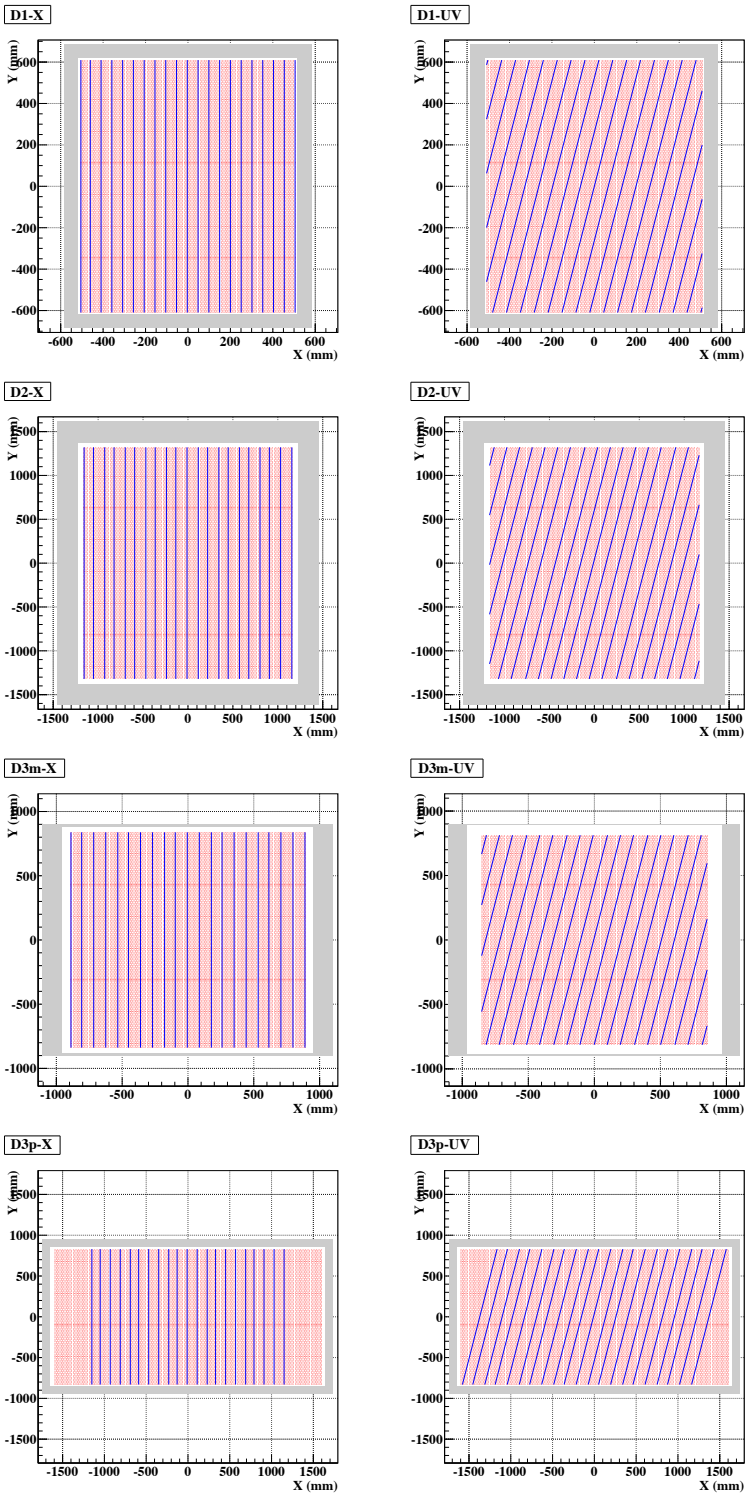

Figure 3.12: Overview of the four different drift chambers used in the SeaQuest experiment. From top to bottom it is Station 1, 2, 3 Plus and 3 Minus. Left column shows the X-planes, right column the tilted UV-planes. The figures show the absolute coordinates in the $x-y$ plane of the SeaQuest spectrometer.

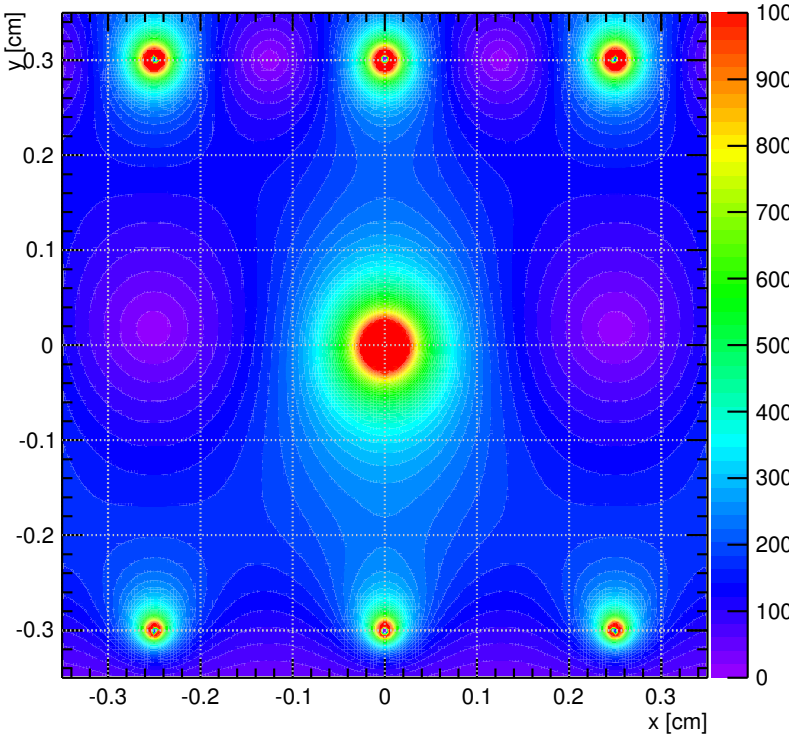

Figure 3.13: Field map in one cell in Station1. Contours of E are shown when the sense wires are at 0 V, and the cathode wires are -1.95 kV. Note, that the voltage values are the design values.

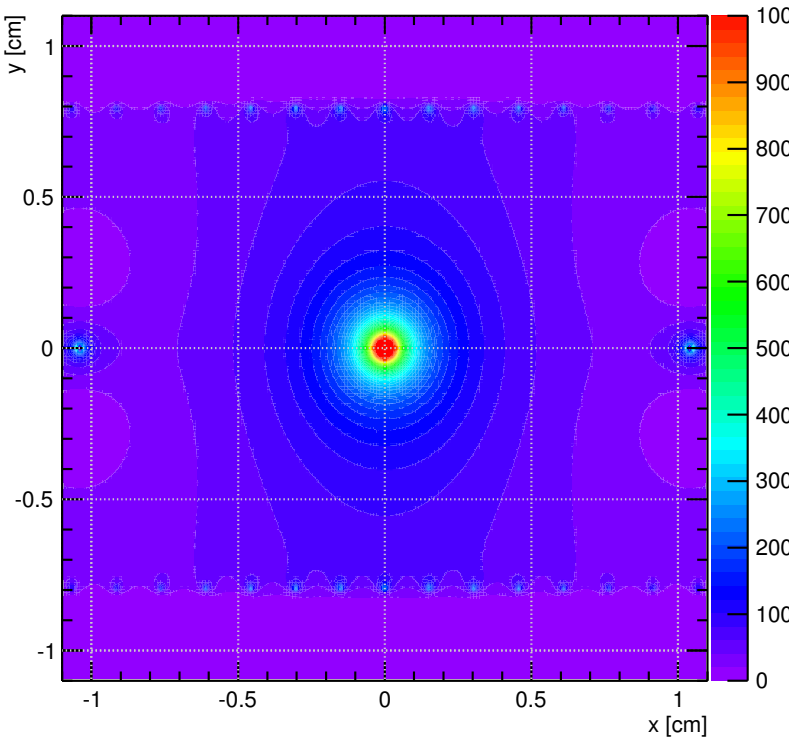

Figure 3.14: Field map in one cell in Station2. Contours of E are shown when the sense wires are at 0 V, and the cathode wires are at -2.5 kV and the guard wires are at -2.5 kV. Note, that the voltage values are the design values.

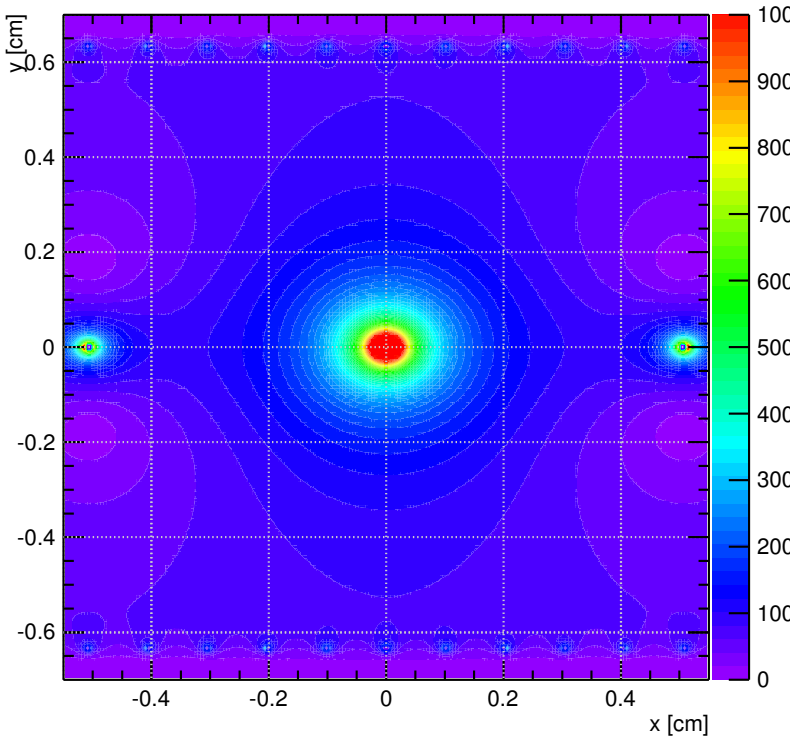

Figure 3.15: Field map in one cell in Station3 Minus. Contours of E are shown when the sense wires are at 0 V, and the cathode wires are at -2.0 kV and the guard wires are at -2.0 kV. Note, that the voltage values are the design values.

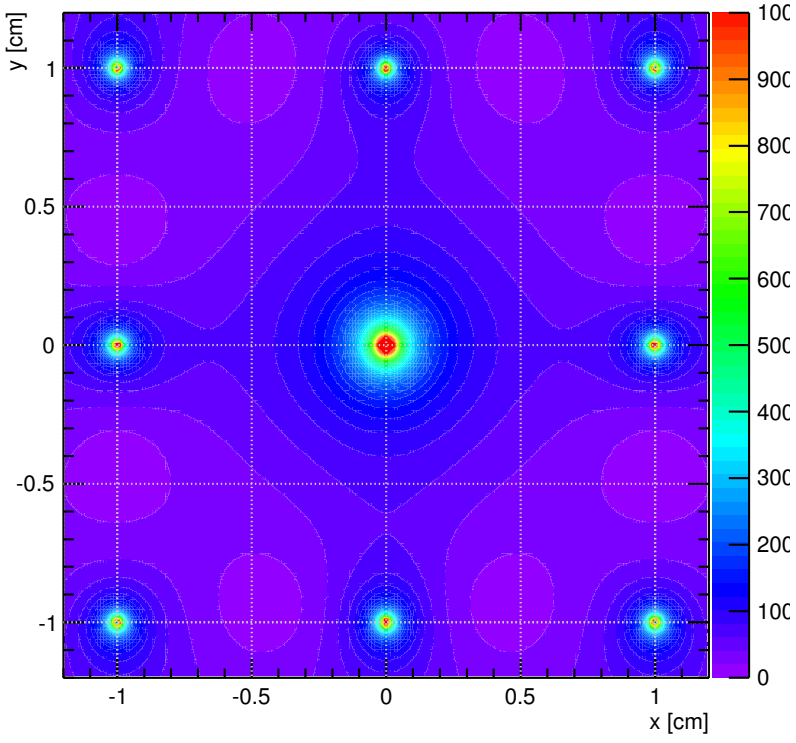

Figure 3.16: Field map in one cell in Station3 Plus. Contours of E are shown when the sense wires are at 0 V, and the cathode wires are at -2.6 kV and the guard wires are at -1.4 kV. Note, that the voltage values are the design values.

Detector	Voltage [kV]	cell size [cm]	# of wires	tilt angle [rad]	$x \times y$ [cm] $\times$ [cm]	z-position [cm]
D1U	1.55	0.635	201	0.244974	101.6×121.92	558.533
D1Up	1.55	0.635	201	0.244974	101.6×121.92	559.168
D1X	1.65	0.635	160	0	101.6×121.92	584.238
D1Xp	1.65	0.635	160	0	101.6×121.92	584.873
D1V	1.65	0.635	201	-0.244974	101.6×121.92	608.134
D1Vp	1.65	0.635	201	-0.244974	101.6×121.92	608.769
D2V	1,925	2.021	128	-0.244974	242.57×269.24	1314.87
D2Vp	1.925	2.021	128	-0.244974	242.57×269.24	1321.86
D2Xp	1.925	2.083	112	0	233.172×269.24	1340.36
D2X	1.925	2.083	112	0	233.172×269.24	1347.35
D2U	1.925	2.021	128	0.244974	242.57×269.24	1366.09
D2Up	1.925	2.021	128	0.244974	242.57×269.24	1373.08
D3pVp	2.4	2	134	0.244974	232×160	1923.2
D3pV	2.4	2	134	0.244974	232×160	1925.2
D3pXp	2.4	2	116	0	232×160	1929.2
D3pX	2.4	2	116	0	232×160	1931.2
D3pUp	2.4	2	134	-0.244974	232×160	1935.2
D3pU	2.4	2	134	-0.244974	232×160	1937.2
D3mU	1.975	0.986	208	-0.244974	180×167.64	1859.99
D3mUp	1.975	0.986	208	-0.244974	180×167.64	1865.39
D3mX	1.950	1.016	176	0	180×167.64	1879.05
D3mXp	1.950	1.016	176	0	180×167.64	1884.45
D3mV	1.925	0.986	208	-0.244974	180×167.64	1898.09
D3mVp	1.975	0.986	208	-0.244974	180×167.64	1903.48

Table 3.3: Overview of the characteristics of all drift chambers in the SeaQuest spectrometer.

3.5.3 Proportional Tubes

The detectors at Station-4 provided muon discrimination capabilities. Located downstream of the hadron absorber wall, station-4 consisted of two hodoscope planes and three proportional-tube planes. Each of the proportional-tube planes had two layers of 5.08 cm wide cells. Adjacent layers were offset by half a cell size in order to cover the dead region between adjacent cells. During the commissioning run, the proportional-tubes were operated using the same gas mixture as used in the drift chambers. Detailed specifications of the proportional-tubes are found in Table 3.4.

Detector	Voltage [kV]	tube radius [cm]	# of tubes	tilt angle [rad]	$x \times y$ [cm] $\times$ [cm]	z-position [cm]
ST4Ha	1.95	5.08	8	0	368.3×40.838	2102.14
ST4Va	1.95	5.08	8	π	40.768×368.3	2178.48
ST4Hb	1.95	5.08	8	0	368.3×40.7913	2393.4
ST4Vb	1.95	5.08	8	π	40.8147×368.3	2371.55

Table 3.4: Overview of the Proportional tube characteristics.

3.6 Data Acquisition System

The SeaQuest data acquisition (DAQ) system used CODA ("CEBAF On-line Data Acquisition") [74] developed by the Jefferson Lab Data Acquisition Group.

CODA is a tool kit composed of a set of software and hardware packages from which a data acquisition system can be constructed. It will manage the acquisition, monitoring and storage of data of nuclear physics experiments. The DAQ includes front-end Fastbus and VME digitization devices (ADCs, TDCs and scalers), the VME interface to Fastbus, single-board VME computers running the VxWorks operating system, Ethernet networks, Unix or Linux workstations. The custom software components of CODA are:

- a readout controller (ROC) which runs on the front-end crates to facilitate the communication between CODA and the detectors.
- an event builder (EB) which caches incoming buffers of events from the different controllers then merges the data streams in such a way that data which was taken concurrently in time appears together.
- an event recorder (ER) to write the data built by EB to the disk.
- an event transfer (ET) system which allows distributed access to the data stream from user processes and inserts additional data into the data stream every few seconds from the control system.
- a graphical user interface (Run Control) to set experimental configuration, control runs, and monitor CODA components.

A recorded CODA file consists of the following major components:

- Header file including a time stamp and other run information like run number, pre-scale factors and event number.

- CODA physics events from the detectors.
- CODA scaler events: the DAQ reads the scaler values every $1-4$ seconds and feeds them into the main data stream. Since counted by stand-alone units, the scaler values are not effected by the DAQ dead time; therefore, they can be used to correct the DAQ dead time.
- EPICS [75] data from the slow control software used at Fermilab, e.g., the spectrometer magnet settings, beam parameters etc.

3.7 The Readout System

During the commissioning run, the SeaQuest-DAQ had three areas of responsibility: event readout, data archiving and online analysis. The backbone of the event readout was the Common Online Data Acquisition System (CODA), which is developed and maintained by Jefferson National Laboratory. Upon receipt of a signal from the level-2 trigger logic-module, a busy signal was raised which inhibited further triggers from being accepted. Simultaneously, the first word of the event was inserted onto the transport bus. Signals were sent to the TDC readouts on the drift chambers and the Latch cards on the hodoscopes. When signaled, the TDC's and Latch cards began digitizing their signals for insertion onto the bus. Each hodoscope and proportional-tube hit resulted in the insertion of an identifying word on the bus. The TDC's would also start a timer which would be terminated by the amplified signal from the drift chamber. This provided a measurement of the drift time in the chamber, which was inserted onto the transport bus along with the element ID of the struck wire.

At this point, the data stream on the transport bus is fed into the Versa Module Eurocard (VME) based archiving system. During the 5s spill cycle, data was first transported to hard-disk storage. Upon completion of the spill, the data are then formatted and sent down the VME pipeline to the CODA archiving system. Here, a decoder is called which is responsible to pipe the data from hard-disk to a MySQL database system. Being read from the MySQL Database, a fraction of the event data and all of the spill information (number of triggers fired, SEM counts, target position, etc...) were sent to the online monitoring systems.

The online monitoring system consisted of a database system interfaced to several graphical tools. The database system allows us to monitor the status of various components of the beamline and spectrometer. Graphical displays of the luminos-

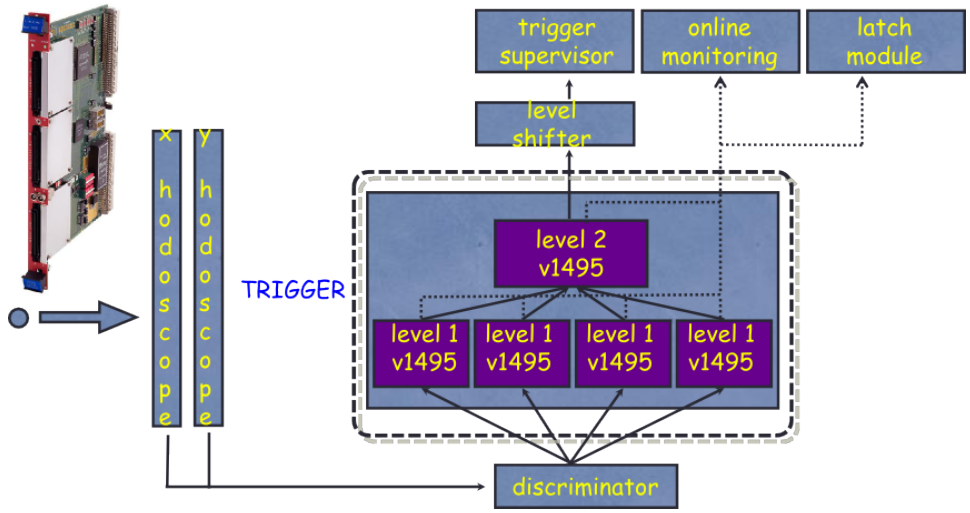

Figure 3.17: The trigger system at SeaQuest is composed of 5 CAEN V1495 FPGA modules. This system sends trigger signals to the trigger supervisor, internal TDC data to CODA for online monitoring, and duplicate all output to the latch module.

ity, magnet voltages, livetimes, etc. gave an overall indication of the health of the spectrometer. The histograms generated by online display code were accessible in real time by making use of the ROOT framework [76]. This allowed us to monitor the detector planes, watching for and correcting any inefficiencies or troubles in detector performance which might develop.

3.8 Trigger

The hardware trigger system examines the scintillator hodoscope hits to identify patterns characteristic of high mass muon pairs produced in the target or the beam dump. It is conceptually similar to the system that was developed for E866/NuSea. However, it is enhanced substantially compared with the previous system, primarily to improve its ability to reject random coincidences that appear to form a candidate high p_T muon track. During the commissioning run however, no cut was applied to the p_T of the triggered dimuon.

The online trigger system at SeaQuest consists of five CAEN v1495 FPGA (Field Programmable Gate Arrays) VME-bus modules [77] (see Figure 3.17). Elec-

tronically, the hardware trigger consists of a single decision stage, implemented as a two-step parallel pipeline. The first step is called 'level-1' trigger, the second step is referred to as 'level-2' trigger. Figure 3.18 shows a block diagram of the FPGA logic.

In the first step, four different level-1 triggers are used. Each of the four level-1 triggers records the hit signals from either the X- (Y-) measuring hodoscopes in the top or bottom of the SeaQuest spectrometer. The registered hit patterns are tested against a preselected set of hit patterns (called "trigger roads") which correspond to a muon from a di- or single-muon event originating from the beam dump traversing the spectrometer. For the commissioning, these hit patterns were optimized for dimuons from J/ψ-events, based on Monte Carlo simulations.

During the commissioning run of SeaQuest, only the X-hodoscopes were used for the trigger. Thus, the two level-1 stages of the Y-measuring hodoscopes were unused. The FPGA level-1 trigger logic identifies three-out-of-four X1-X2-X3-X4 coincidences, which are characteristic of high p_T single muons produced in the beam dump. Each time they observe a candidate track, they output a logical bit indicating its charge, the side of the spectrometer (left or right) where it is located. In general, X1-X2-X4 triple coincidences suffice since the spectrometer analyzing magnet of the spectrometer is located between Stations 1 and 2. Adding the extra constraint that the appropriate channel of X3 must have a hit can help reject apparent tracks that actually consist of a random coincidence between hits in Stations 1 and 2 due to one muon and a hit in Station 4 due to another muon.

The second step in the trigger pipeline combine the x tracking results from the first step to identify events with candidate high p_{Tx} muons present. The candidate muons will be characterized according to their charge, the side of the spectrometer on which they are located, and a rough measure of their p_T. Events are also tagged that appear to have two muons with opposite charges present on the same side of the spectrometer. In parallel with the first step of the main trigger sequence, OR's of all the scintillators on each side of each plane are generated and routed to a so-called "Track Correlator" to generate simple cosmic ray and noise triggers for diagnostic purposes.

The level-2 step in the trigger pipeline generates the actual triggers, handles the experiment busy logic, and strobes the read-out electronics. This step is performed with one v1495 FPGA logic module, which is the module for the Track Correlator. Five sets of Physics triggers (referred at Matrix Modules) were used in the trigger system.

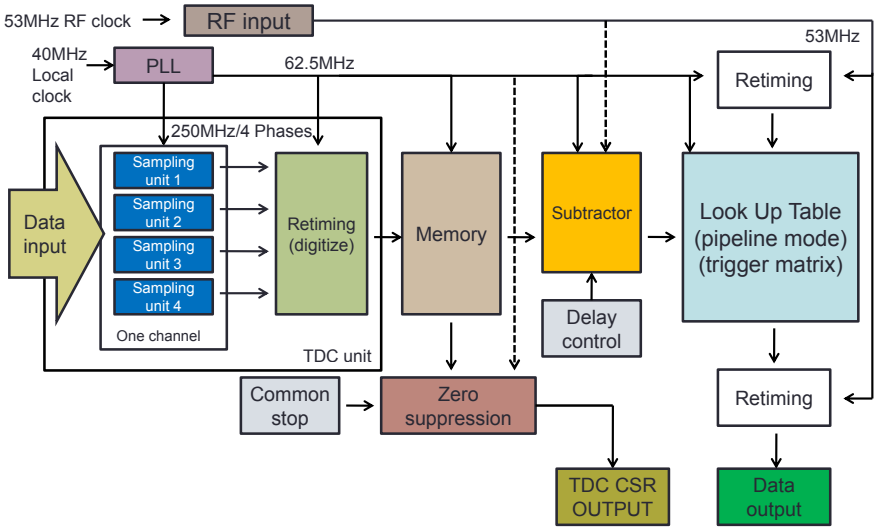

Figure 3.18: The block diagram of the FPGA triggers. The SeaQuest trigger is synchronized with the Main Injector 53 MHz-RF-clock. The trigger-internal clock is 40 MHz.

The primary physics trigger Matrix-1 (“FPGA1”) trigger selected oppositely-charged muons which traversed opposite sides of the spectrometer (top and bottom), while Matrix-2 (“FPGA2”) triggers selected single charged muons which traversed either top-side or the bottom-side of the spectrometer. Matrix-1 and Matrix-2 were the main physics triggers used during the commissioning run.

Matrix-3 (“FPGA-3”) and Matrix-4 (“FPGA-4”) trigger on single muon tracks either on the top-side or bottom-side of the detector. Matrix-5 (“FPGA-5”) trigger selected muons of any charge which traversed on opposite sides of the spectrometer (top and bottom). The main porpuse of theses triggers were mainly of diagnostic purposes. Data triggered with trigger FPGA-5 are aimed to be used to extract the combinatorial background.

Since the FPGA based triggers are under continuous development, two additional NIM-based triggers are used for the trigger system of SeaQuest. The first NIM trigger is NIM-1 and triggers X1-X2-X3-X4 coincidences between top- and bottom-half of the detector. Nim-2 triggers X3-X4 coincidences between top- and bottom-side of the SeaQuest spectrometer. Table 3.5 shows an overview of all different trigger types.

Trigger Type	Trigger Condition	Sign	Roads	Road origin	$\#\mu$
FPGA-1	Top and Bottom (3 out of 4)	opposite	J/ψ	Beam dump	2
FPGA-2	Top or Bottom (3 out of 4)	plus or minus	J/ψ	Beam dump	1
FPGA-3	Top only (3 out of 4)	plus or minus	J/ψ	Beam dump	1
FPGA-4	Bottom only (3 out of 4)	plus or minus	J/ψ	Beam dump	1
FPGA-5	Top and Bottom (3 out of 4)	any sign	J/ψ	Beam dump	2
NIM-1	Top and Bottom (4 out of 4)	n.a.	n.a.	n.a.	n.a.
NIM-3	Top and Bottom (X3-X4 only)	n.a.	n.a.	n.a.	n.a.

Table 3.5: A summary of the different trigger types used during the commissioning run at SeaQuest. 5 different FPGA triggers were used. Their roads were generated from J/ψs originating from the beam dump. For diagnostic purposes, also two NIM-based triggers were used.

3.9 The Drift Chamber Front End Electronics

The ASDQ card

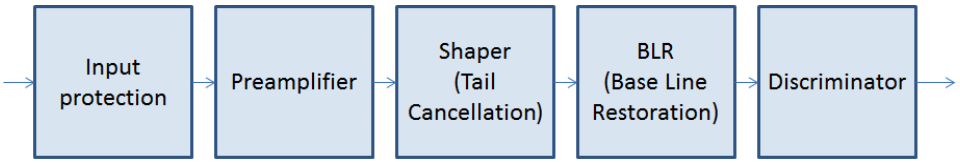

Figure 3.19: Diagram showing the signal path from the raw signal generated in the drift chamber via all stages in the ASQD card. For details, see the text.

The most important component of the read-out electronics of the drift chambers at SeaQuest is the so called "ASDQ" read-out card. "ASDQ" is an acronym for amplification, shaper, discriminator, and charge integration (Q option). All of these features are encoded in the "ASDQ chip" that was designed and developed for the central outer tracker of the CDF experiment at Fermilab [78]. The ASDQ chip provides following features:

- **Preamplifier**: This step is responsible for amplification of the raw signals

from the drift chambers. It converts the charge input into a voltage output while minimizing the noise.

- **Ion tail cancellation**: In this step, the ion tail of the amplified signal is eliminated. In addition, one more amplification is done.
- **Baseline restoration (BLR)**: The signal is being brought back to nominal zero in this step. This is the last stage where the analogue signal can be readout before being discriminated by a discriminator. The amplification factor to the raw signal's current is $\approx 17\,\mathrm{mV/fC}$.
- **Discriminator**: When the amplified signal is exceeding the adjustable threshold, a pair of differential signals is output. The threshold can be changed from 0 to 10 mV for the BLR signal.
- **Charge encoding option**: This option integrates signal amplified signal over the time. This integral is proportional to the total charge of the raw signal. This option is however not used in the SeaQuest experiment.

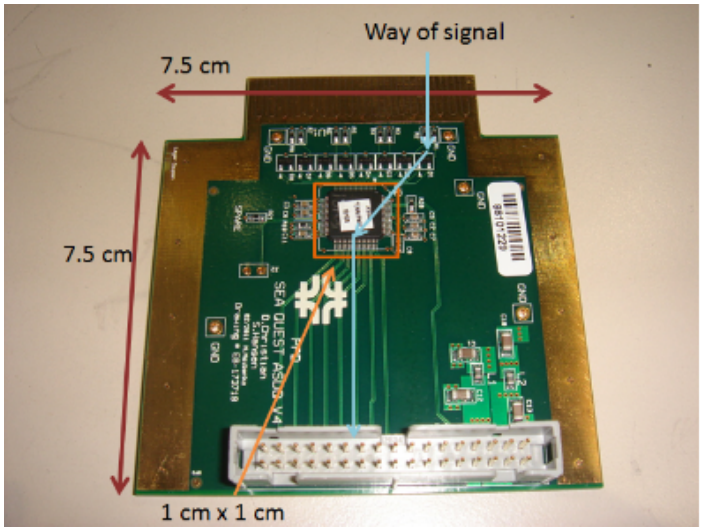

Figure 3.20: The ASDQ card. The area of the ASDQ card is 7.5cm $\times$ 7.5 cm. The ASDQ chip is placed on the center of the card, indicated with an orange square.

At the input-side of the ASDQ card, an input protection is mounted, which is designed to buffer the preamplifier from large external positive and negative spikes. Figure 3.19 shows the signal path of the raw signal through the ASDQ card. Figure 3.20 shows a picture of the ASDQ card. The $1\,\mathrm{cm} \times 1\,\mathrm{cm}$ ASDQ chip is marked with an orange square on the center of the card. The surrounding gold edge provides as

a common ground level of the card. The edges of the ASDQ card are connected to the frame of the chambers as shown in Figure 3.21. One ASDQ card has 8 readout channels which are connected to the sense wires respectively. Altogether, about 700 ASDQ cards are used for all the drift chambers at SeaQuest.

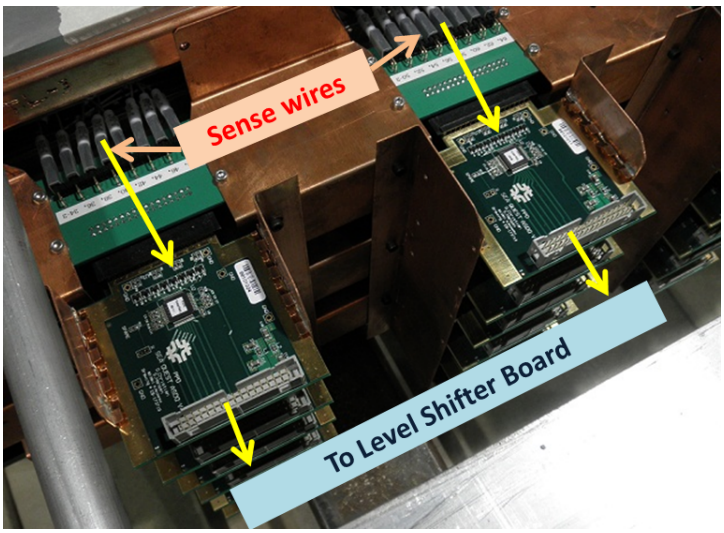

Figure 3.21: ASDQ cards are placed on the Station 3 Plus drift chamber. 8 sense wires are connected to one ASDQ card. The edge of the ASDQ card is connected to the frame of the chamber which serves as common ground to the electronics. Yellow arrows indicate the signal path starting from the sense wires.

The Level Shifter Board

Level shifter board (LS board) is a specialized multi-purpose board to supply low voltages ($+3\,\mathrm{V}$ and $-3\,\mathrm{V}$) to the ASDQ cards. It is responsible for converting the differential signals from the ASDQ cards to standard LVDS signals. One LS board can operate 8 ASDQ cards. Thus, about 100 LS boards for all the drift chambers are in use at SeaQuest. Several LS boards can be daisy-chained by telephone connectors. By a standard telnet connection via an Ethernet cable, the following features of the LS boards can be set

- **Threshold level adjustment**: the threshold value of the ASDQ cards can be set. The threshold level is a 12-bits value $(0-4096)$ which corresponds to $0-10\,\mathrm{mV}$ in the analogue signal.

- **Internal pulser**: The LS board can send quasi-signals resembling a raw signal to an ASDQ card. The frequency and the height of the internal pulse can be set. In addition, the LS board allows to control which channels of the

ASDQ are addressed. The following settings can be chosen: a pulse to all even channels, a pulse to all odd channels, and a pulse to all channels of an ASDQ card.

- **Low voltage monitor**: It is possible to monitor all low voltage values on the ASDQ card and the ASDQ chip. It is mainly for diagnostic purposes.

3.10 Chamber Performance Requirements

The following paragraphs are completely based on assumptions, calculations and derivations presented in detail in [79] and [80]. The purpose of this section to derive minimum requirements of the tracking chamber operation. It will be shown that the most crucial properties w.r.t. the track reconstruction can be derived from very basic chamber properties, like e.g. position resolution.

3.10.1 Single Plane Efficiency

In this section it should be demonstrated how the single-plane efficiency $\varepsilon_{s.p.}$ relates to the overall spectrometer efficiency to reconstruct a full muon track ε_{μ} and dimuon $\varepsilon_{di\mu}$. Two scenarios are compared. The first one is called '6-of-6-plane tracking' which requires exactly one hit from all 6 layers of all three stations (top or bottom). The second one is called '5-of-6-plane tracking', and requires just five out of six layers per station to detect a muon. The following Table 3.6 summarizes and compares the two scenarios.

	6-of-6-plane tracking			5-of-6-plane tracking		
$\varepsilon_{s.p.}$	$\varepsilon_{s.p.}$	ε_{μ}	$\varepsilon_{di\mu}$	$\varepsilon_{s.p.}$	ε_{μ}	$\varepsilon_{di\mu}$
0.99	0.94	0.83	0.70	1.00	1.00	1.00
0.95	0.74	0.40	0.16	0.97	0.90	0.82
0.90	0.53	0.15	0.02	0.89	0.69	0.48

Table 3.6: Oveview of different scenarios of the single-plane detection efficiency $\varepsilon_{s.p.}$. The muon and dimoun reconstruction efficiencies ε_{μ} and $\varepsilon_{di\mu}$.

It is obvious that that the minimum single-plane efficiency $\varepsilon_{s.p.}$ should not be below ≤ 0.95 when assuming the '5-of-6-plane tracking'.

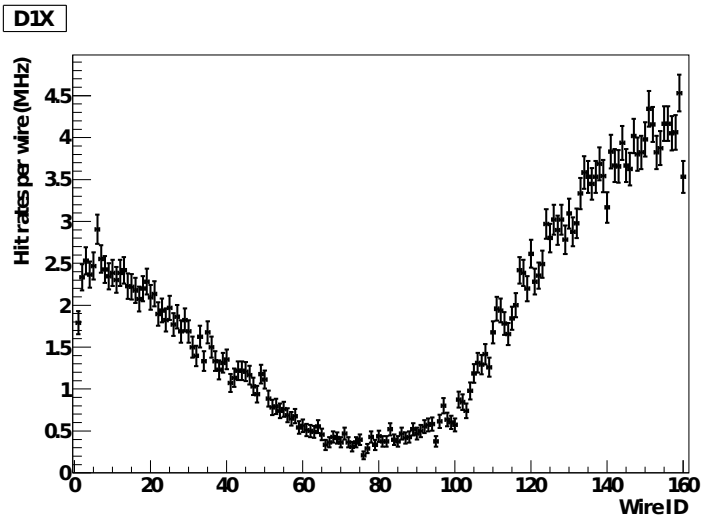

Figure 3.22: Distributions of the single muon's rate in one dimension. The unit in the x-axis is wire-ID which is equivalent to the x-coordinate of the wire inside the spectrometer.

3.10.2 Rate Tolerance

Figure 3.22 shows the single muon's rate at Station 1 in the SeaQuest spectrometer. In Station 1 the highest rates are expected due to its vicinity to the target and beam dump. The integrated expected single rate for Station 1 chamber is 290 MHz. The single rates were evaluated with a GEANT4-based simulation. The maximum single rate per wire and per plane are listed for each station in the following Table 3.7 for all tracking stations. The main source of single rate in the SeaQuest spectrometer

Stations	f_{wire}^{max} [MHz]	f_{plane} [MHz]	$W \times H$ w/ wire spacing [cm]
1	4.0	290	102×122 w/ 0.6
2	2.5	73	233×269 w/ 2.1
3 Minus	0.7	20	232×160 w/ 2.0
3 Plus	0.2	9	180×168 w/ 1.0

Table 3.7: Single muon rates in all four tracking stations of the SaQuest detector.

is the accidental coincidence muons originating from pion decay $p+d \rightarrow \pi^{\pm} + \pi^{\mp} + X \rightarrow \mu^{\pm} + \mu^{\mp} + X$. A method to estimate and model the accidental or random background is presented in the analysis section of this thesis.

Considering the maximum drift times T_{max} for each tracking station during the commissioning run, it is possible to estimate the expected TDC hit rates. First we define the probability P_{BKG}^{wire} that a true hit is associated with a background (without

further specification) as the following:

$$P_{BKG}^{wire} = f_{wire} \cdot T_{max} \,. \tag{3.10.1}$$

In addition we define the probability P_{BKG}^{UV} that a true hit associated with a background hit in the same UX or XV overlapping area as follows

$$P_{BKG}^{UV} = P_{BKG}^{wire} \cdot N_{wire}^{Xing} \,. \tag{3.10.2}$$

With equations (3.10.2) and (3.10.1), it is possible to estimate the expected occupancy O for each station

$$O = f_{plane} \cdot T_{max}/N_{wire} \,. \tag{3.10.3}$$

The following table 3.8 summarizes the probabilities P_{BKG}^{wire}, P_{BKG}^{UV} and expected occupancy O for each station based on the maximum drift time T_{max}. The only way

Stations	T_{max} [ns]	P_{BKG}^{wire} [%]	P_{BKG}^{UV} [%]	O [%]
1	80	32	1300	15
2	180	45	1200	12
3 Minus	180	13	380	3.1
3 Plus	120	2.4	100	0.6

Table 3.8: P_{BKG}^{wire}, P_{BKG}^{UV} and expected occupancy O for each station in the SeaQuest spectrometer. For details, see text.

to influence the occupancy of the chambers is to choose a gas mixture with a small T_{max}. In the next chapter a method to reject background hits will be introduced.

3.10.3 Position and Mass Resolution

One very important resolution of the SeaQuest spectrometer is the mass resolution. It is very directly related to the chamber resolutions. The momentum resolution only depends on the geometrical setup of the spectrometer as can be seen in the following equation

$$\frac{\Delta P}{P} = \frac{P}{P_{kick}} \sqrt{\Delta y_1^2 + (1 + \frac{z_{12}}{z_{23}})\Delta y_2^2 + \left(\frac{z_{12}}{z_{23}}\right)^2 \Delta y_3^2} \,, \tag{3.10.4}$$

where $z_{xy} = z_x - z_y$, z_i is the z-coordinate of the ith station and Δy_i is the position resolution of the i-th chamber. In general the momentum resolution can split up to the three contributions by position resolution ('Chamber'), multiple scattering

('Iron') and angular resolution ('θ'). The individual contributions are added in quadrature to obtain the overall momentum resolution

$$\left(\frac{\Delta P}{P}\right)^2 = \left(\frac{\Delta P}{P}\right)^2_{Chamber} + \left(\frac{\Delta P}{P}\right)^2_{Iron} + \left(\frac{\Delta P}{P}\right)^2_{\theta}. \tag{3.10.5}$$

The momentum resolution can be linked to the mass resolution in the following way

$$\frac{\Delta M}{M} = \frac{\Delta P}{2P}. \tag{3.10.6}$$

It is interesting to note that the resolution $\Delta x_2/x_2$ is dominated by the mass resolution as can be seen in the following parametrization

$$\frac{\Delta x_2}{x_2} \approx 0.57\,\Delta x_f + 0.012\,M^2\frac{\Delta M}{M}. \tag{3.10.7}$$

Figure 3.23 shows the expected mass resolution for typical Drell Yan events evaluated in the dimuon rest frame. Figure 3.24 shows the individual contributions to the mass resolution following Equation (3.10.5) for typical Drell-Yan events. The biggest contribution arises from the multiple scattering within the FMAG absorber. The plots were evaluated assuming a position resolution of 400 μm for each station. Within the SeaQuest acceptance ($\theta = 60^\circ - 120^\circ$), a typical mass resolutions of $\Delta M/M$ of $5-15\%$ is reached. In order to remove all J/ψs from Drell-Yan dimons a 3σ mass cut must be set to 4.5 GeV/c^2 assuming a maximum mass resolution of 15%.

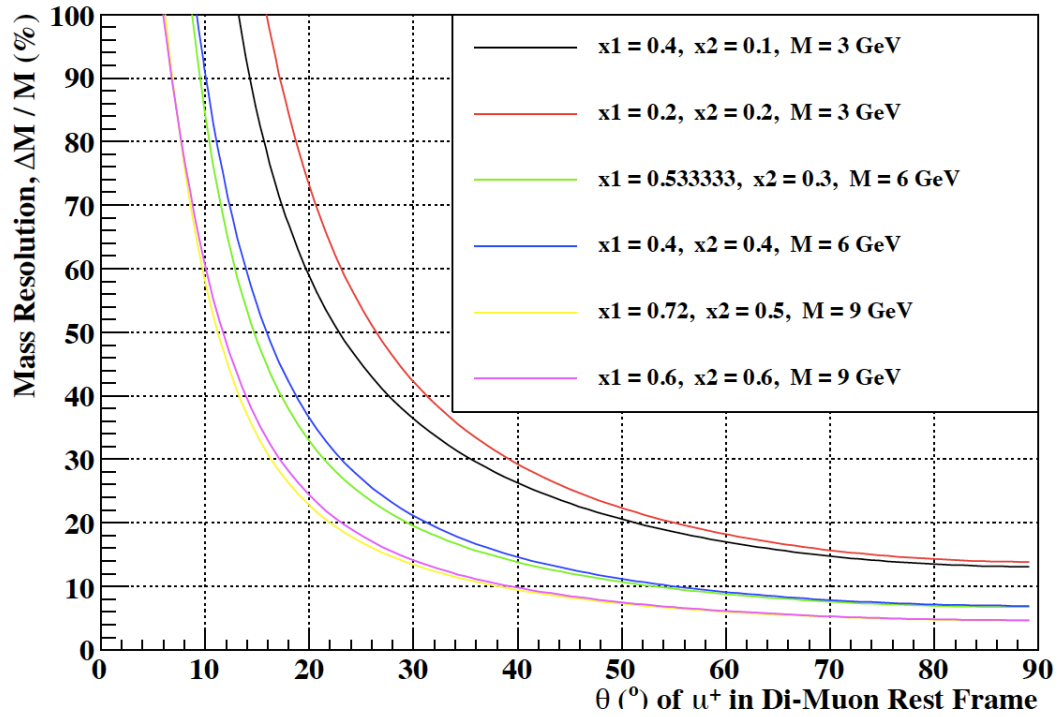

Figure 3.23: Expected mass resolution $\Delta M/M$ of the SeaQuest detector for typical Drell-Yan kinematics. Within the SeaQuest acceptance ($\theta = 60^\circ - 120^\circ$), a typical mass resolutions of $\Delta M/M$ of $5-15\%$ is reached.

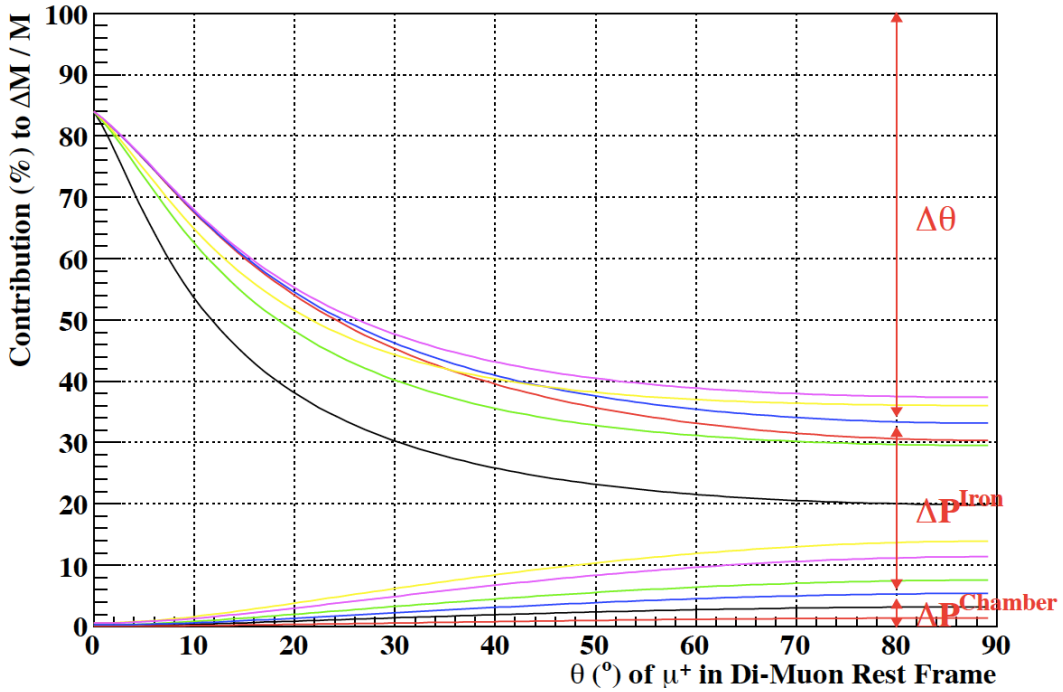

Figure 3.24: Individual contributions to the mass resolution $\Delta M/M$ of the SeaQuest detector.

Chapter 4

Dimuon Track Reconstruction at SeaQuest

4.1 A Track Model for SeaQuest

Spectrometers in particle and nuclear physics have the purpose of identifying the 4-momenta an`fTrkSeeder` and vertices of particles stemming from high-energy collisions and decays of particles or nuclei. The 3-momenta and positions of charged particles are measured by tracking them in magnetic fields with the use of position sensitive detectors. Cluster finding procedures can be applied in some detectors to combine the responses of individual electronic channels in order to improve the accuracy of the position measurements. The position measurements will be called 'hits' throughout this thesis, regardless of whether they stem from a single detector channel or from a combination of several of them. Pattern recognition or track finder algorithms determine which hits contribute to the individual particle tracks. The hits identified at this stage to belong to one track then serve as the input to a fitting procedure, which determines the best estimates for the position and momentum of a particle at any point along its trajectory. A novel algorithm for this task of track finding in the SeaQuest detector is presented in this chapter. It organizes the task of track finding, i.e. the interplay between finding detector hits and associating those with particles trajectories.

As a first step, a formalism is introduced, which allows to describe muon tracks traversing the whole SeaQuest spectrometer. The aim of the formalism is to be as general as possible on one hand, and as restrictive as necessary in describing the track topologies on the other hand. With help of this formalism, it will be possible to combine hits from different drift chambers. The formalism provides a toolkit

to judge if the a given combination of hits is likely to form a muon track. The presented track finding algorithm considers hits from the three different tracking stations at the SeaQuest spectrometer.

4.1.1 The Sagitta Formalism

The goal is to provide a formalism which is capable of describing a muon's trajectory in the SeaQuest spectrometer. Tracking Station 1 is located between the two dipole magnets, FMAG and KMAG. Stations 2 and 3 are located in the back part of the spectrometer behind the analyzing magnet KMAG. Muon tracks going through the complete SeaQuest detector are deflected by both dipole magnets. This fact can be easily be made use of by introducing the 'sagitta' measurement. In general a sagitta is defined as the deflection form a straight line.

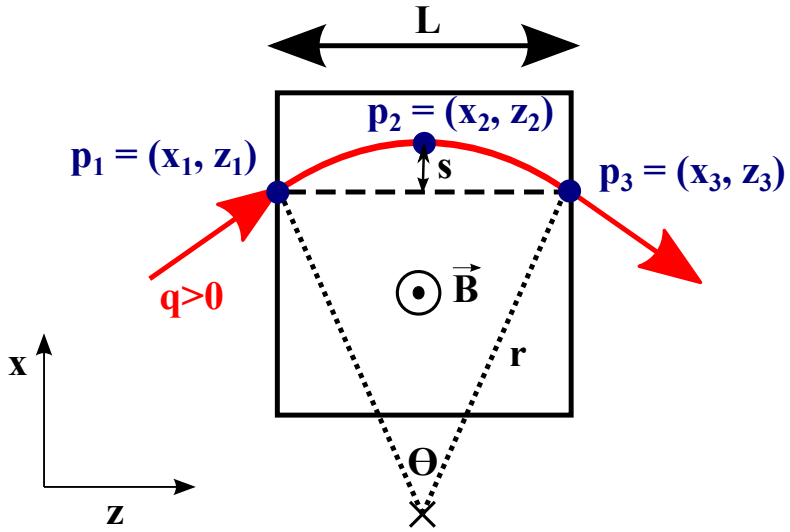

Figure 4.1: A positively charged particle traversing a magnetic field $\vec{B}$. The sagitta is defined as $s = x_2 - \frac{x_1+x_3}{2}$.

As an example we assume the coordinate x at three equidistant measurements in the (x,z) plane $(y = 0)$, as can be seen in Figure 4.1.2. The constant magnetic field $\vec{B}$, which points in the y-direction, deflects the particle on a trajectory perpendicular to the field vector. The particle's momentum component perpendicular to $\vec{B}$ can then be determined with the help of the Lorentz force to $p_\perp = 0.3Br\,\mathrm{GeV/T\cdot m\cdot c}$, with r being the radius of its arc. With the following equation

$$\frac{L/2}{r} = \sin\frac{\theta}{2} \approx \frac{\theta}{2}\,(\text{for small } \theta) \quad \rightarrow \quad \theta = \frac{L}{r} = \frac{0.3B\cdot L}{p_\perp} \tag{4.1.1}$$

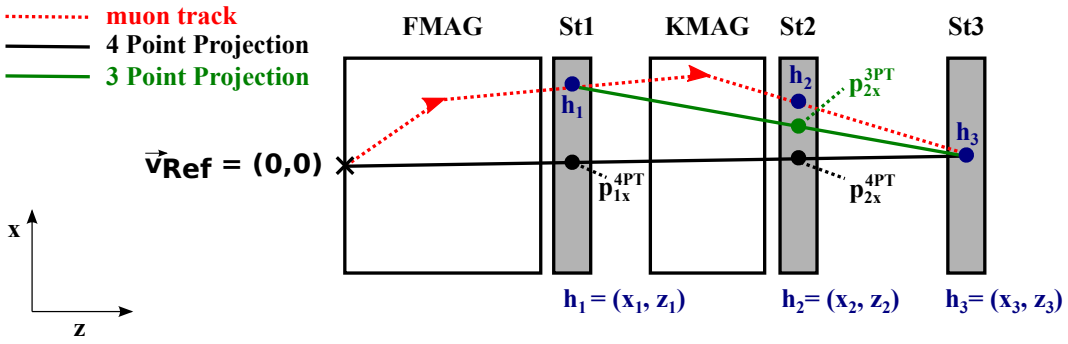

Figure 4.2: In the SeaQuest spectrometer three different sagittas can be measured. The first is the 3-Point sagitta, which measures the deflection of a hit h_2 in station 2 from the projection line between points the points h_1 in station 1 and h_3 in station 3 (green line). The other sagitta measurement is the 4-Point sagitta. Here, the projection line is spanned between a reference point $\vec{v}_{Ref} = (0,0)$ and a hit h_3 in station 3. The 4-Point sagitta can measure both the deflection of a hit in station 1, h_1, and and the deflection of hit in station 2, h_2, from the corresponding projection line (black line).

the sagitta s can be expressed as

$$s = r\left(1 - \cos\frac{\theta}{2}\right) \approx r\left(1 - \left(1 - \frac{1}{2}\frac{\theta^2}{4}\right)\right) = r\frac{\theta^2}{8} \approx \frac{0.3}{8}\frac{L^2 B}{p_\perp}. \tag{4.1.2}$$

In Eq. (4.1.2), it becomes obvious that the sagitta s is proportional to $1/p_\perp$. By summarizing the other coefficients into a detector dependent constant c_D, the sagitta s finally yields

$$s = \frac{c_D}{p_\perp}. \tag{4.1.3}$$

The small angle approximation in Eq. (4.1.2) demands that the sagitta s is small compared to the radius r. Then, Eq. (4.1.3) only holds for sufficiently high momenta $p_\perp$.

4.1.2 Sagitta Measurements in the SeaQuest Detector

The presented formalism is fundamental for a track finder algorithm which groups hits in the different drift chambers to one muon track. In order to achieve this in a fast processing time, no drift times and no global fitting of a track candidate is applied at this stage. The goal is to provide a detailed description of the muon tracks in terms of drift chamber hits as much as possible. The key observable is the sagitta. For the measurement of a sagitta in the SeaQuest detector, at least three different space points in the $x-z$-plane are necessary. A natural choice of points

is to use three hits from the drift chamber stations 1, 2 and 3 (Plus or Minus). A combination of hits $(h_1, h_2, h_3)^{\text{View}}$ from three different stations is referred to has "hit-triplet", or simply "triplet".

The projection between two points, p_1 and p_3 (see Figure) on the line $z = z_2$ defined by the space point p_2 is defined as

$$p_{2,x} = \frac{(z_2 -_z 1)}{(z_3 - z_1)}(x_3 - x_1) + x_1 \,. \tag{4.1.4}$$

Taking Eq. (4.1.4), the sagitta s of point p_2 is defined as the following

$$s = p_{2,x} - x_2 \,. \tag{4.1.5}$$

In the SeaQuest spectrometer, muon tracks are deflected by two separate dipole magnets. It is thus possible to define the following two groups of sagitta measurements:

- The Three-Point (3-PT) Measurement: This measurement is using the projection between the station 1 hit and the station 3 hit as projection line (see the green line in Figure 4.2).
- The Four-Point (4-PT) Measurement: Here, the projection line is spanned between a reference point $v_{Ref} = (0,0)$ and a hit h_3 in station 3. The 4-Point sagitta can measure both the deflection of a hit h_1 in station 1 and and the deflection of a hit h_2 in station 2 from the corresponding projection line (see the black line in Figure 4.2).

In the following paragraphs, the two 4-Point and 3-Point sagittas are considered as independent from each other and thus are uncorrelated.

4.1.3 Organization of Sagitta Measurements

Each triplet of hits $(h_1, h_2, h_3)^{View}$ is defined in a specific coordinate system. This coordinate system depends on the orientation of the layer where the hits were measured. Each drift chamber at SeaQuest consists of six layers, which can be divided into three stereo-layers, such as X'XVV'UU'. One stereo-layer is commonly referred as "view". The layers of one view have the same tilt direction ($0°$, $+14°$, $-14°$). In addition, since there are two stereo-planes in each of the three drift chamber stations, $8\,(= 2^3)$ different combinations of primed and un-primed layers can be built. Primed and un-primed layers are layers with the same tilt angle, but which are

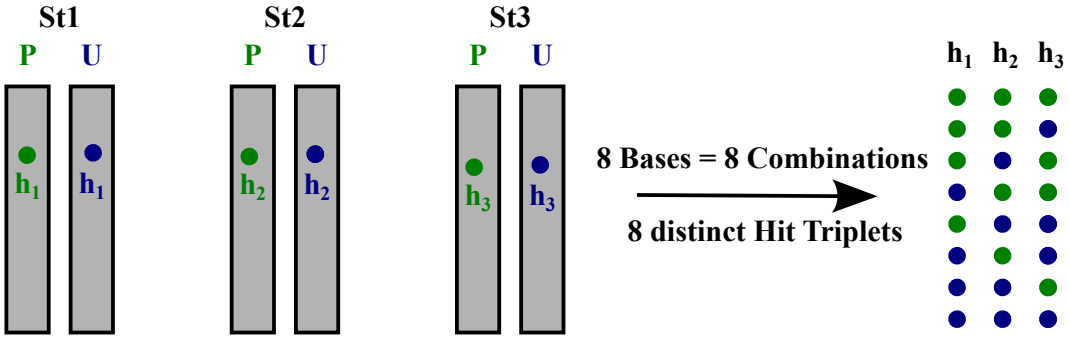

Figure 4.3: Illustration of the sagitta "basis". One basis represents one hit triplet combination between hits (green and blue dots) from different stereo layers (labeled as U or P). Each station has one stereo layer, for Station 3 either the top or the bottom is considered.

shifted by half a wire spacing with respect to each other. From here, we are referring to each of such a combination as the measurement "basis" (see Figure 4.3).

As a first step, each hit must be assigned to an appropriate coordinates within the (local) drift chamber coordinate system. The SeaQuest data acquisition system is recording the element ID of each hit in an event. The following formula describes the conversion from a recorded element ID to a line in the x-y plane. The center for a wire in x-direction, x_{cent}, is defined as (also see Figure 4.4)

$$x_{cent} = x_0 + \Delta x + dx \cdot (ID_{\text{Wire}} - (N_{\text{Elements}} + 1)) \cdot \frac{1}{2}) \tag{4.1.6}$$

with x_0 being the center of the drift chamber in the x direction, Δx the shift for primed and unprimed wire planes, dx the wire spacing, ID_{Wire} the recorded element ID of a hit, and N_{Elements} the total number of wires in the chamber. Details on the drift chamber geometries are listed in Table 3.3 of Chapter 2. With Eq. (4.1.6), a wire is defined by the following top- and bottom coordinates

$$\vec{x}_{top} = \begin{pmatrix} x_{cent} + \tan(\theta) \cdot h_{\text{DC}}/2 \\ y_{cent} - h_{\text{DC}}/2 \end{pmatrix} \quad \vec{x}_{bot} = \begin{pmatrix} x_{cent} - \tan(\theta) \cdot h_{\text{DC}}/2 \\ y_{cent} + h_{\text{DC}}/2 \end{pmatrix}, \tag{4.1.7}$$

with y_{cent} being the center of the drift chamber in the y direction, w_{DC} the width of the drift chamber, h_{DC} the height of the drift chamber, θ the tilt angle of the wire plane.

Since the sagittas are measured in the x-z plane, only the x-coordinate of a hit coordinate vector is considered. For hits in tilted wire planes, a coordinate rotation $R_{xy}(\theta)$ in the x-y plane is applied such that the top and bottom x-coordinate are the

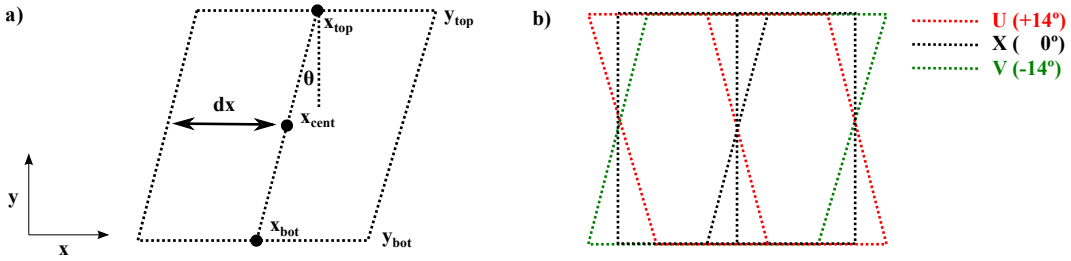

Figure 4.4: a) Definition of the top and bottom coordinates of a wire in a drift chamber. b) Representation of the three different measurement basis, defined by the tilt angle θ of the corresponding wire plane.

same

$$\vec{x}'_{top/bottom} = R_{xy}(\theta) \cdot \vec{x}_{top/bottom} \,. \tag{4.1.8}$$

Finally, an unified naming scheme for all the chambers at SeaQuest is introduced. Since the drift chambers were partially re-used from old experiments (and partially newly constructed), the naming scheme of the tilted and un-tilted wire planes was not consistent (see e.g. Table 3.3 of Chapter 2). The new naming scheme is summarized in Table 4.1. All planes are arranged and ordered following their positive or negative tilt-angle ("+" or "−"), and their relative positive and negative x-shift direction ("+" or "−") between stereo layers.

Angle \ Rel. Shift	Layer Name St 1	St 2	St 3+	St 3-	New
−\+	U	Up	Vp	Up	**Sp**
−\−	Up	U	V	U	**S**
0\+	Xp	X	Xp	Xp	**Xp**
0\−	X	Xp	X	X	**X**
+\−	V	V	U	V	**T**
+\+	Vp	Vp	Up	Vp	**Tp**

Table 4.1: Consistent naming scheme for the layers in all drift chamber station in the SeaQuest spectrometer. The layers are ordered following the direction of the tilt angle and the direction of the relative shift between stereo layers.

4.1.4 Sagitta Measurements with Single Muons

In the previous section the methods of the measurement of sagitta with help of hit-triplets were described and introduced. In this section, measurements based in data are shown. Details on the cuts which were applied can be found in the next Chapter 5. For the measurement the data-set "run2166" was used. In this run the single-muon trigger FPGA-2 described in Chapter 3 was activated. The standard hit-level cuts (like after-pulse removal, hodoscope masking and in-time cuts for the hodoscopes and drift-chambers) were applied to the RAW data sample. For the selection of muon track candidate, events with clear muon tracks with exactly 1 hit per drift chamber and hodoscope plane were selected. By requiring exactly 18 drift chamber hits in the complete SeaQuest spectrometer, full detection efficiency was assumed. Altogether ≈ 3800 events were passing these selection criteria. They were then analyzed in terms of hit-triplets. For each hit triplet the 3-PT sagitta and the two 4-PT sagittas were determined. This has been done for all 8 basis in all 3 views. So, for each view, and for each sagitta measurement we can extract 8 different independent measurements, resulting in a total of 72 sagitta measurements ($= 3\text{views} \times 3\text{sagittas} \times 8\text{basis}$).

Figure 4.5 summarizes the 72 sagitta measurements. The 4-PT-S1 sagittas have a tail at $\approx \pm 30\,\text{cm}$, and a gap between $\approx +5\,\text{cm}$ and $\approx -5\,\text{cm}$. The 4-PT-S2 sagittas have a tail at $\approx \pm 15\,\text{cm}$, and a gap between $\approx +2.5\,\text{cm}$ and $\approx -2.5\,\text{cm}$. The 3-PT sagittas have a tail at $\approx \pm 6\,\text{cm}$. All sagittas show a symmetry around 0 cm with a slight enhancement of negative sagitta values. This can be quantitavely explained by the dominance of μ^+'s due to the dominant background process of pion-muon decay. The positive charge is pronounced due to the up-quark dominance in the proton. Small shifts in the sagittas can particularly be seen in the 3PT sagittas. Misalignment of the detector is a possible explanation for that.

In a second step, the extracted sagitta values were compared to the momentum measurements from the re-constructed event sample (see track reconstruction sections at the end of this Chapter, and details of analysis in the next Chapter). The plots show that, the sagittas without taking drift distances into account, already provide a very good, first estimate for the particle momentum. In Figure 4.6 the sagitta calibrations can be seen. In each sagitta-bin, the p_z-distribution was fitted with a single-Gaussian. From that fit, the average momentum $\langle p_z \rangle$ and standard deviation σ_{pz} was determined. In the last step, these momentum estimates including their un-

certainties were fitted with the following function (motivated by Equation (4.1.3))

$$f(x_s) = \frac{c_0}{c_1 + c_2 \cdot x_s}. \tag{4.1.9}$$

The fit results for all views and all sagitta types are summarized in Figure 4.6. It can be seen in Figure 4.7 that especially the 4-Point-St1 sagitta measurements provide a very precise momentum estimate. This is rather surprising since no drift times and no global track fitting has been applied at this stage yet.

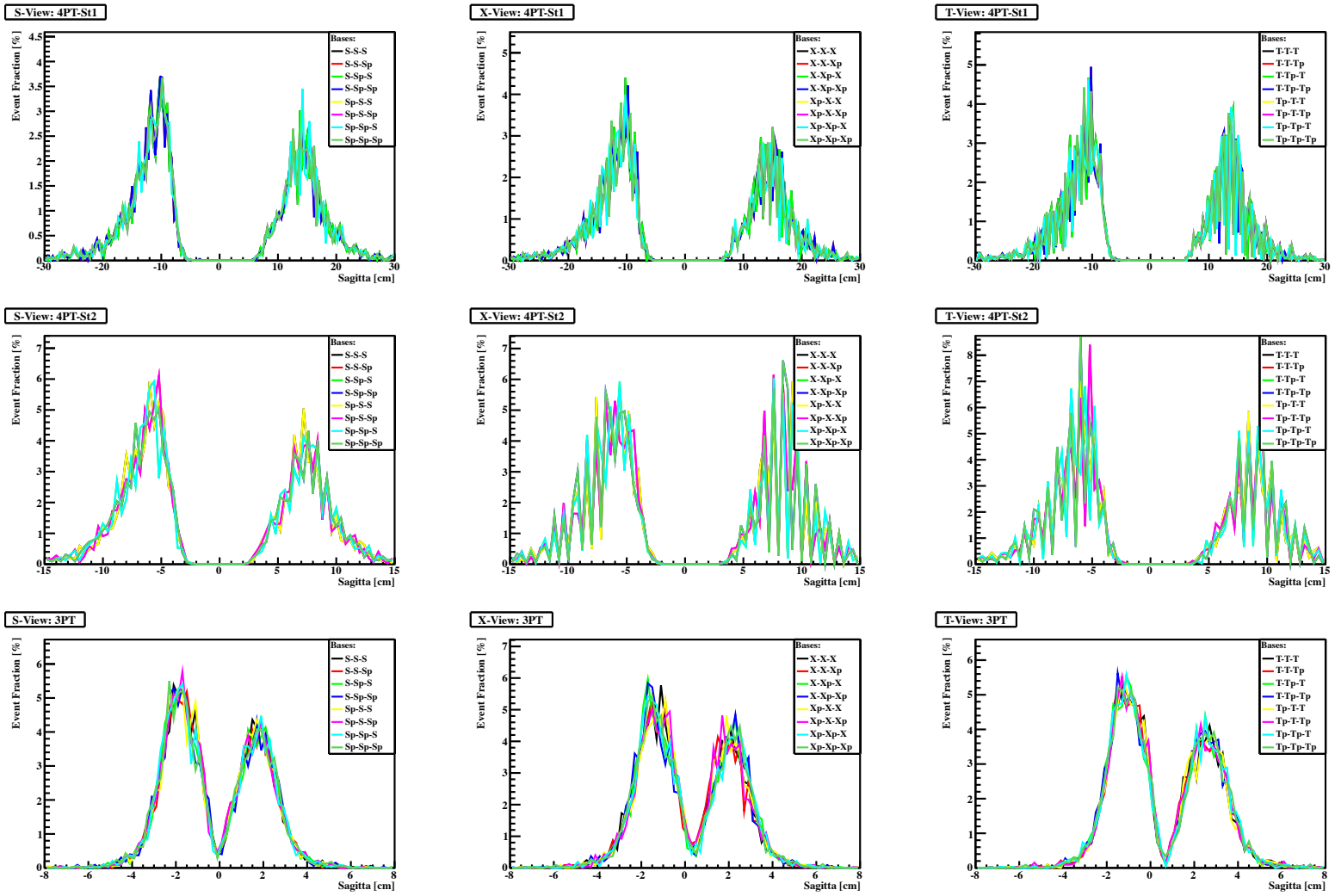

Figure 4.5: The 72 sagittas which can be measured with hit-triplets in the SeaQuest spectrometer. The sagittas were obtained from single muons. The top row shows 4-PT-St1 sagittas, the middle row the 3-PT-St2 sagittas and the bottom row the 3-PT sagittas. From the left column to the right column, the S-, X- and T-view measurements are presented. In each view the sagittas were measured in all 8 basis.

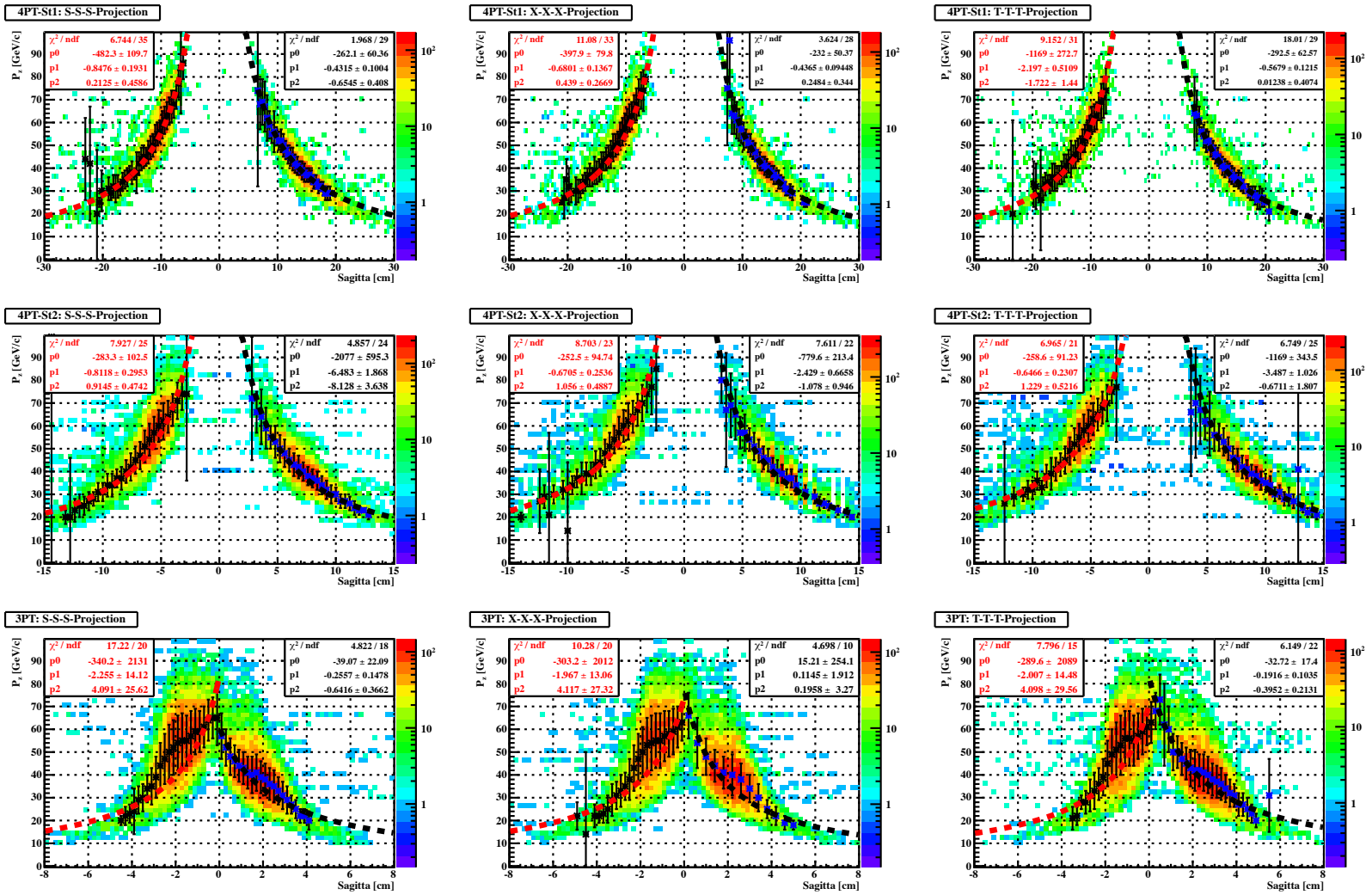

Figure 4.6: The Momentum calibrations of the sagittas are shown. In each sagitta bin, the momentum is fitted with a single Gaussian. The mean values and uncertainty for each sagitta bin was fitted with the function fiven by Equation (4.1.9). The top row shows 4-PT-St1 sagittas, the middle row the 4-PT-St2 sagittas and the bottom row the 3-PT sagittas. From the left column to the right column, the S-, X- and T-view measurements are presented. In each view the sagittas, all 8 basis were combined.

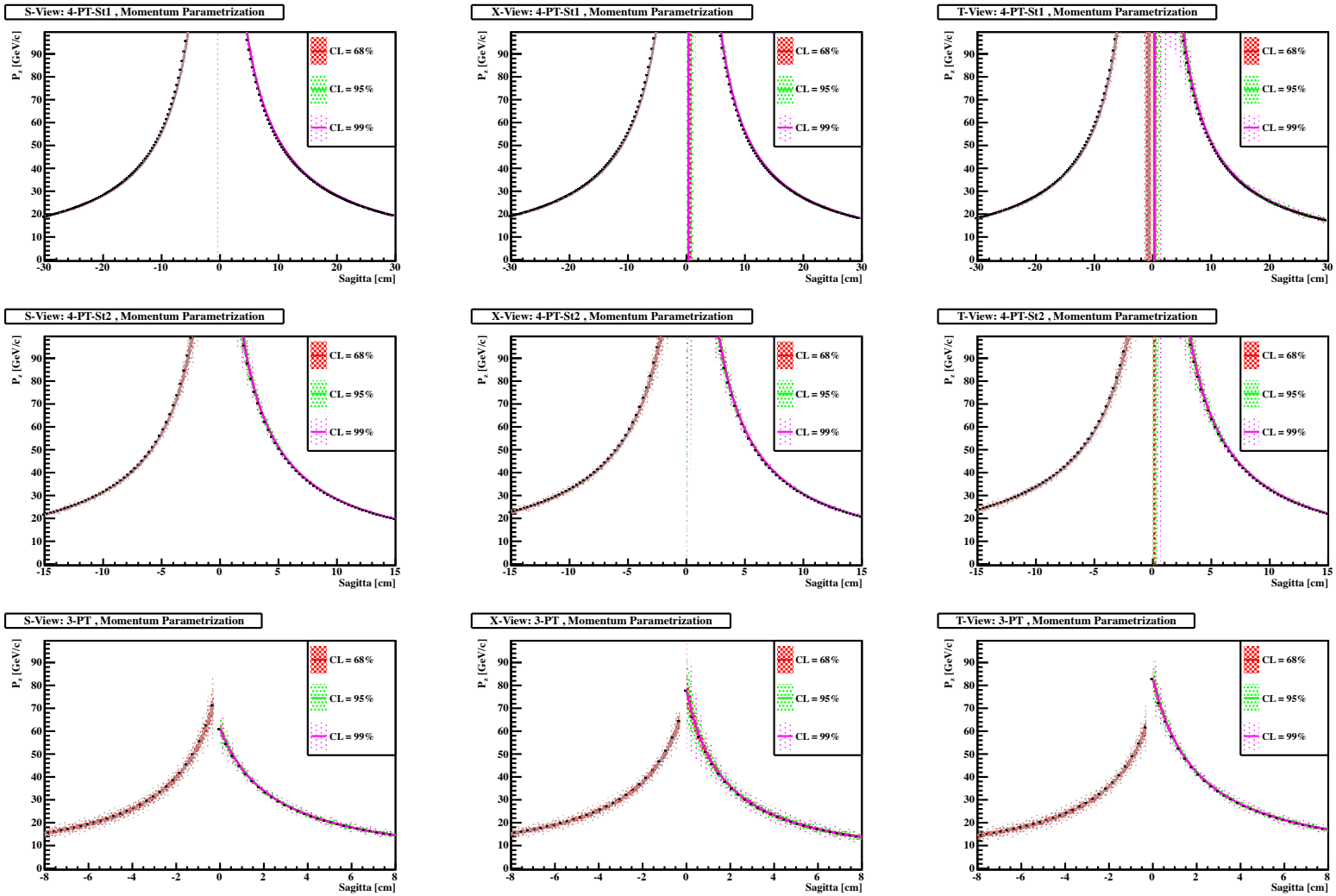

Figure 4.7: The final sagitta-momentum parameterizations of are shown. The parametrization is determined by Equation (4.1.9), the parameters were obtained from a fit of the sagitta measurements to reconstructed single muons. Each parametrization is performed with a 1σ, $2,\sigma$ and $3\,\sigma$ uncertainty estimate.

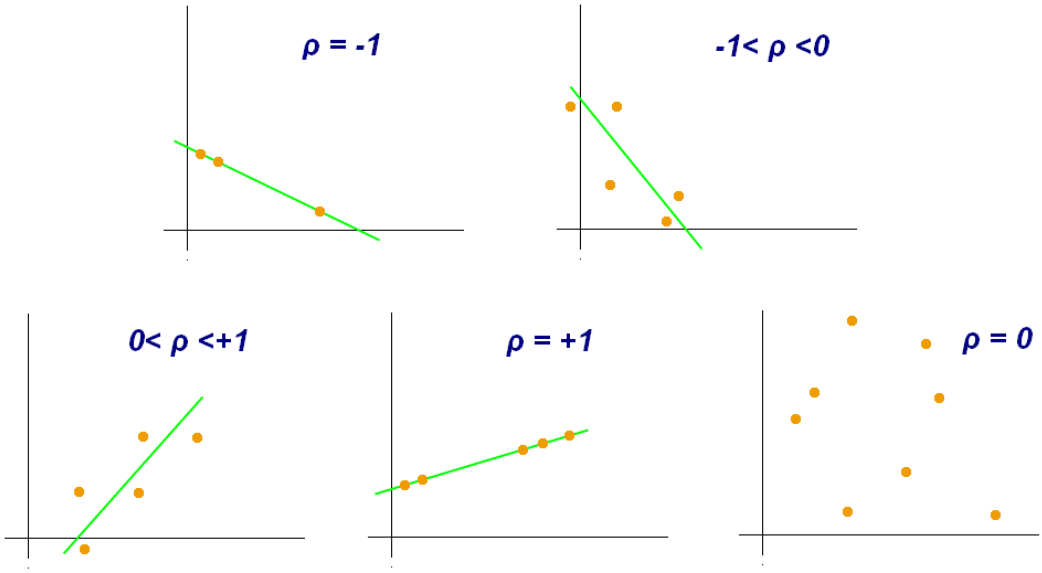

Figure 4.8: Illustration of the Pearson correlation coefficient ρ.

4.1.5 The Correlation Matrix

The 72 sagitta measurements, which were introduced in the previous section, can now be correlated with each other. The idea is to use these correlations as a track model in SeaQuest. A correlation c_{ij} between sagitta s_i and sagitta s_j is defined as

$$c_{ij} = \frac{s_i}{s_j} \quad \text{with} \quad i,j \in [0,71]. \tag{4.1.10}$$

Considering Eq. (4.1.3), it is clear that these correlation coefficients only depend on the spectrometer dependent constants c_D and hence are independent of the particles momentum. The following equation makes this clear.

$$c_{ij} = \frac{c_i^D}{c_j^D} = \text{const.} \tag{4.1.11}$$

All correlation coefficients c_{ij} span a 72×72-matrix, the so-called "correlation matrix" whose elements are constant. The combined set of coefficients c_{ij} describes how the sagittas in the different views are related to each other. These constant correlations provide sufficient constraints for a track model at SeaQuest. All drift chamber hits arising from real muon tracks can be combined to hit-triplets. This model specifies clearly how different hit-triplets in one event can be combined such that the hits form a track candidate. The details about how to properly combine different triplets are described in the following sections.

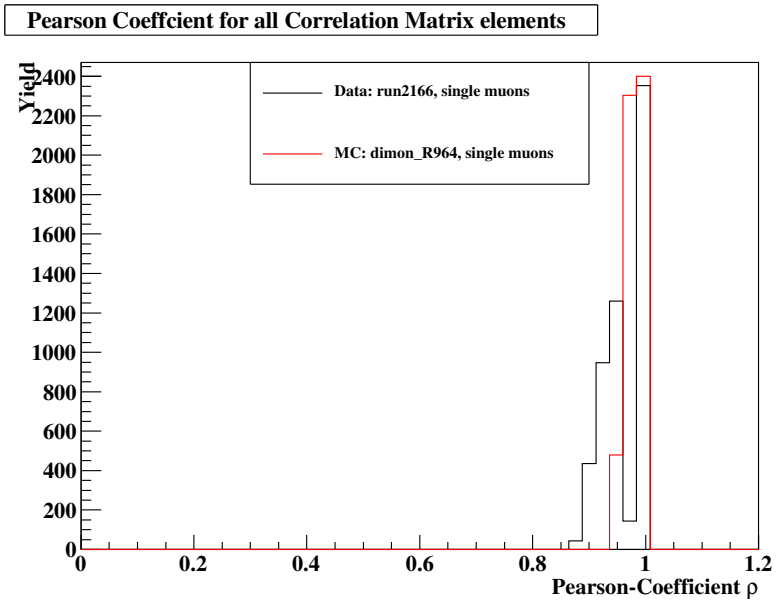

Figure 4.9: Distribution of Pearson coefficients ρ of all matrix elements. Black line represents data, red line Monte-Carlo.

One way to show and illustrate that all matrix elements are well correlated is to evaluate the so-called Pearson coefficient ρ for each matrix element. This coefficient ρ is defined as

$$\rho_{ij} = \frac{\mathrm{cov}(s_i, s_j)}{\sigma_i \sigma_j} = \frac{\mathrm{E}\left[(s_i - \mu_i)(s_j - \mu_j)\right]}{\sigma_i \sigma_j}. \tag{4.1.12}$$

Figure 4.8 shows an illustration of the Pearson coefficient. Figure 4.9 shows the distribution of Pearson coefficients of all elements of the correlation matrix. The minimum value for the coefficients is between ≈ 0.85 and ≈ 0.90, the average is ≈ 0.95. The agreement between data (black line) and Monte Carlo (red line) is very good.

It is important to keep in mind how the indices of the correlation matrix are related to the view, basis and type of sagitta-measurement. The index conversion is defined by

$$\begin{aligned} idx_{\text{View}} &= i \div 24 \\ idx_{\text{Basis}} &= (i \bmod 24) \div 3 \\ idx_{\text{Sagitta Type}} &= (i \bmod 24) \bmod 3 \end{aligned} \tag{4.1.13}$$

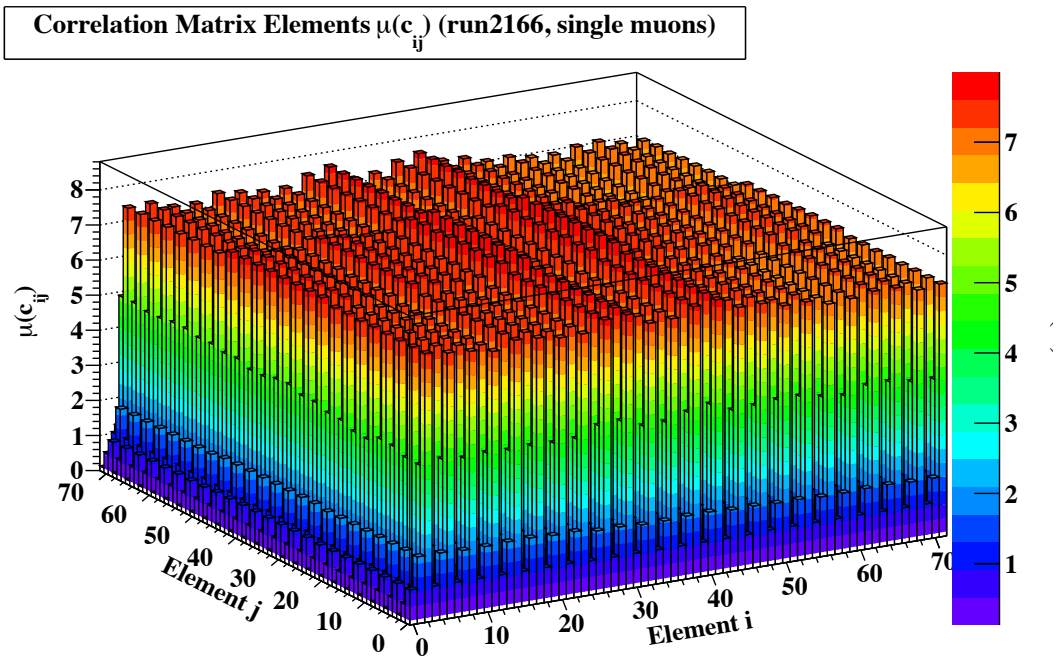

Figure 4.10: The correlation matrix: schematic of the mean value of each element c_{ij}.

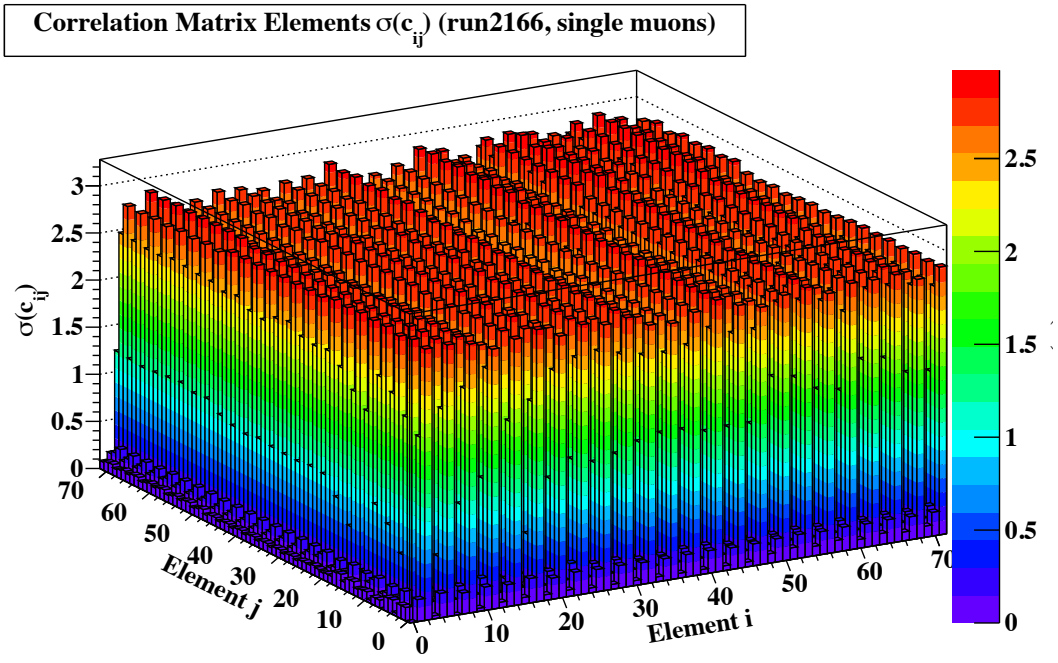

Figure 4.11: The correlation matrix: schematic of the uncertainties of each element c_{ij}.

resulting in the subsequent map

$$\begin{aligned} idx_{\text{View}} &\in [0,1,2] \equiv (\text{S-View}, \text{X-View}, \text{T-View}), \\ idx_{\text{Base}} &\in [0,1,\ldots,8], \\ idx_{\text{Type}} &\in [0,1,2] \equiv (\text{4-PT-St1}, \text{4-PT-St2}, \text{3-PT}). \end{aligned} \tag{4.1.14}$$

Based on the same single-muon data set as used in the previous section, the full correlation-matrix was extracted. For each coefficient c_{ij}, the mean value $\langle c_{ij} \rangle$ and RMS σ_{ij} were determined. One representation of the mean values $\mu(c_{i,j})$ and RMS $\sigma(c_{i,j})$ correlation matrix can be seen in Figures 4.10 and 4.11. Figure 4.12 shows three matrix elements both as one-dimensional distribution and as two-dimensional scatter plot. Figure 4.13 shows the inverse matrix elements of Figure 4.12, and it can be obviously seen that the correlation matrix is not symmetric. In the next section, the hypothesis that the obtained correlation matrix provides a full track model will be tested and examined with the help of Monte-Carlo simulations of muons in the SeaQuest spectrometer.

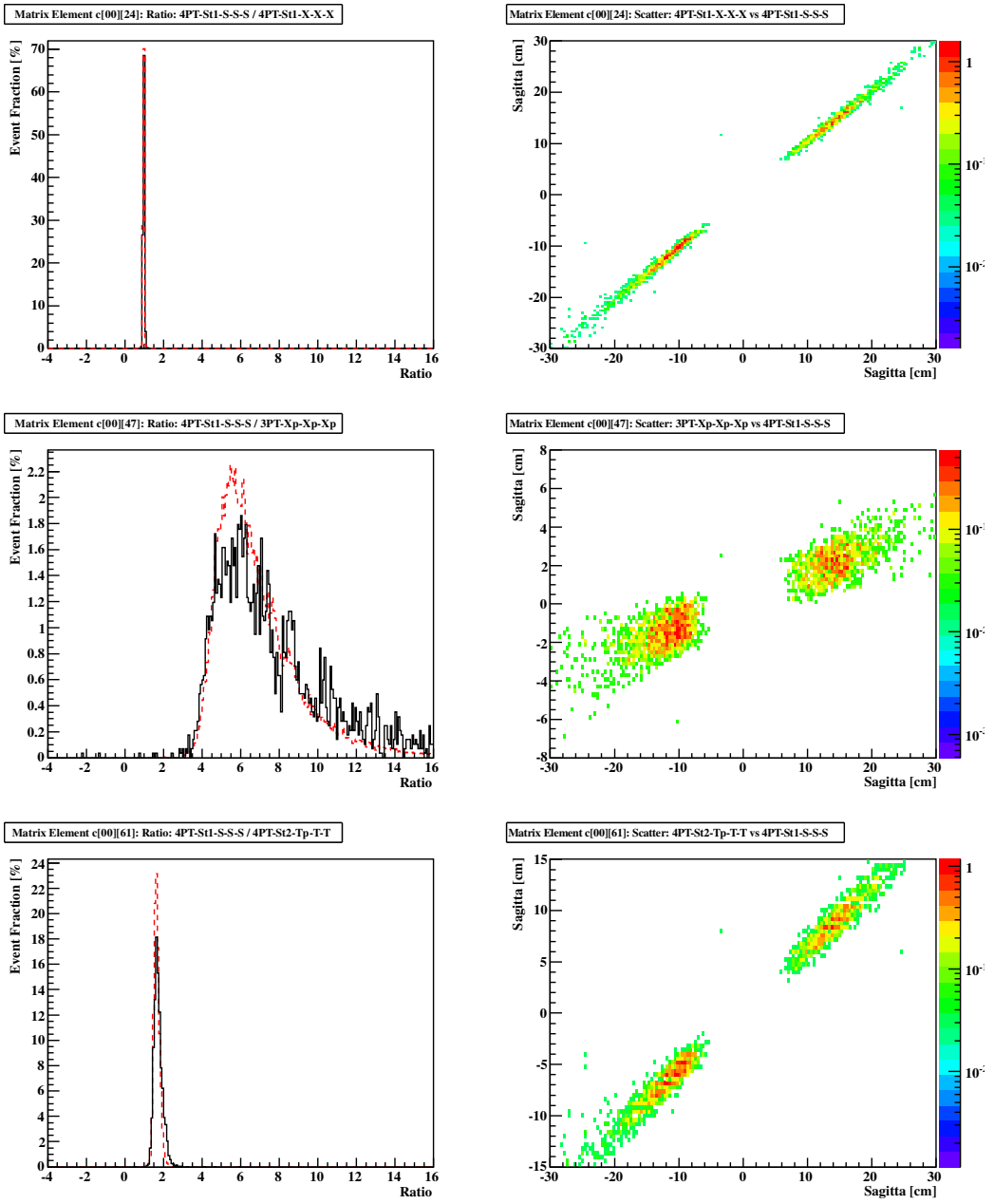

Figure 4.12: Three matrix elements are shown as illustration. Both the one-dimensional representation (left) and the two-dimensional scatter plot (right) are illustrated. In the one-dimensional representation data (black line) is compared to Monte Carlo (red line). Note the varying scales of the *x*- adn *y*-axis in the two-dimensional plot.

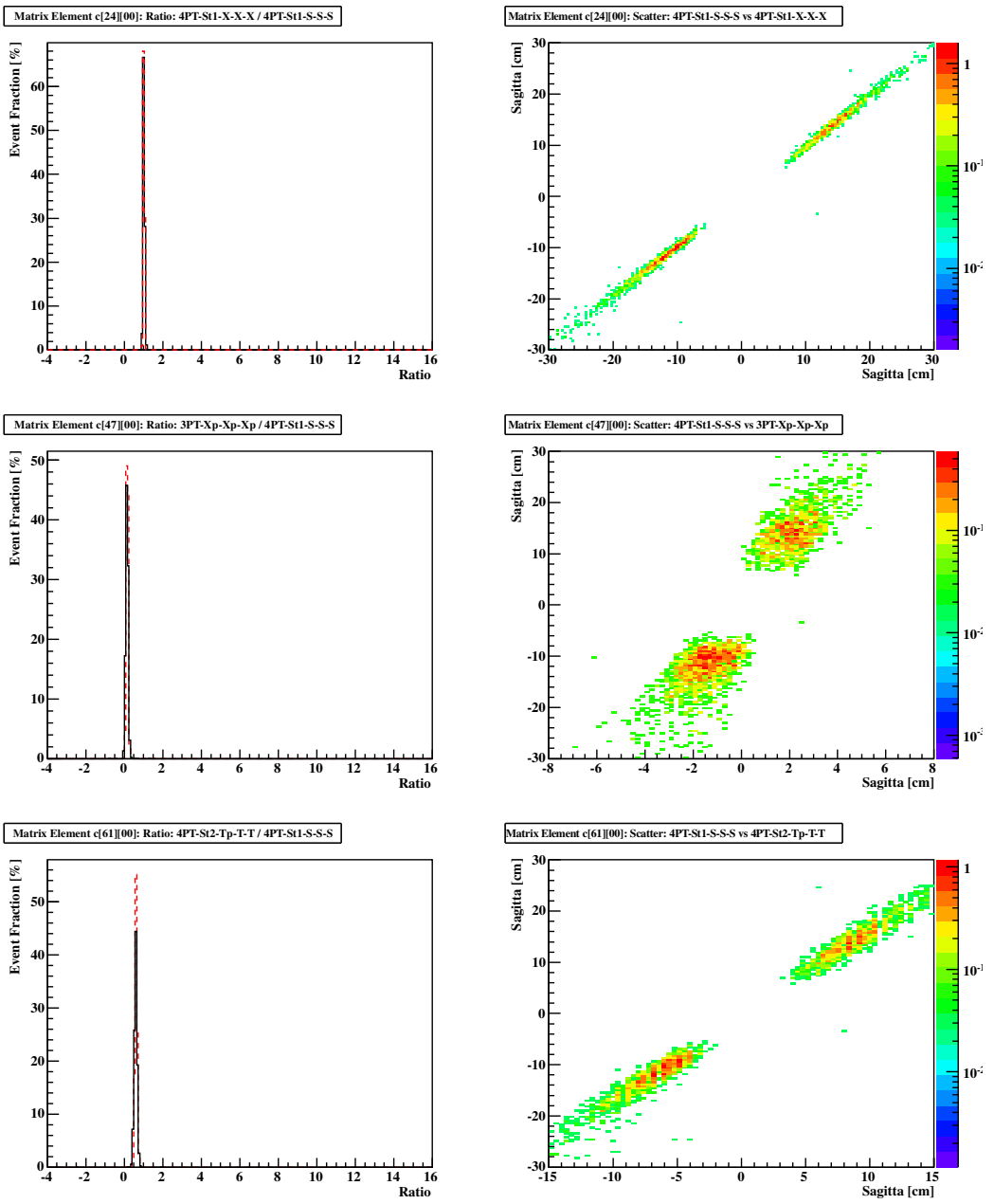

Figure 4.13: The matrix elements which are inverse to the ones shown in Figure 4.12. In the one-dimensional representation data (black line) is compared to Monte Carlo (red line). Note the varying scales of the *x*- adn *y*-axis in the two-dimensional plot.

4.1.6 The Correlation Matrix in Monte-Carlo Studies

The Correlation Matrix was extracted from clear single muon data in the previous section. In order to test the robustness of the extracted correlation matrix, it is necessary to compare the correlation matrix with GEANT4 Monte Carlo Events. The purpose of this study is to check if our track hypothesis and track model in terms of the correlation matrix is valid.

The SeaQuest software group provides several productions of Monte Carlo events. One of the Monte Carlo engines used at SeaQuest is the GEANT4 Monte Carlo (GMC). In the Physics event generation, dimuons are generated following the LO Drell-Yan cross sections. The CTEQ5 PDF set [12] was used for the event generation in the following productions. Subsequently, the generated muons were boosted into the laboratory frame, and processed by the GEANT4 [81]. GEANT4 includes facilities for handling geometry, tracking and detector response.

Since the GMC generates dimuon events, only one of the two muon tracks was selected randomly. In order to match the cut criteria from the analysis of real data, all 18 muon track hits in the tracking stations were required for the extraction of the correlation matrix. Roughly 150k MC events were analyzed.

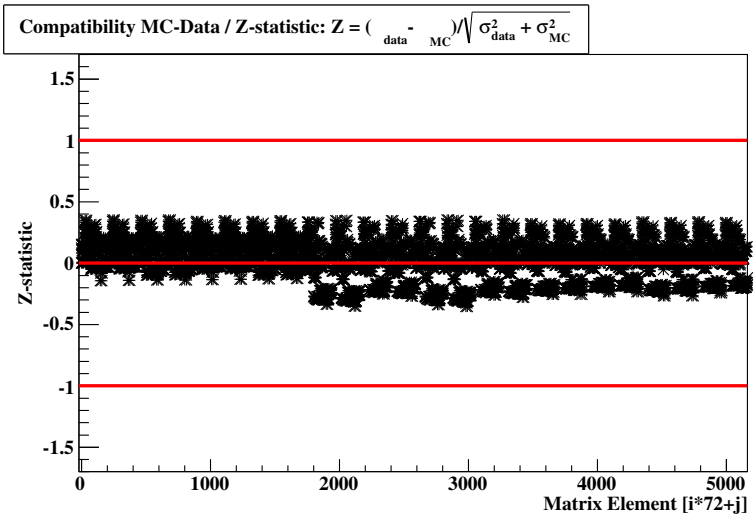

Figure 4.14: The Z-statistic between the Correlation matrix obtained in data and Monte Carlo. If the value is within ± 1, it is an indicator for the compatibility between the two data sets.

The extracted correlation matrix from Monte-Carlo was compared to the correlation matrix from data, by the so-called Z-statistic. To allow the identification of systematic discrepancies between Monte Carlo and real data, deviations were computed for each matrix element of the correlation matrices. The Z-Statistic is defined

as

$$Z = \frac{\mu_{\text{Data}} - \mu_{\text{MC}}}{\sqrt{\sigma^2_{\text{Data}} + \sigma^2_{\text{MC}}}}. \tag{4.1.15}$$

Figure 4.14 shows the Z value for each of the 5184 matrix elements. Assuming normally distributed matrix elements, the Z-statistic is bounded within the values ± 1. No systematic trends can be observed. The correlation matrix in Monte Carlo and in real data are statistically compatible. The track model in form of the correlation matrix can be considered as valid and correct.

4.2 fTrkSeeder - The Track Finding Algorithm at SeaQuest

The correlation matrix provides a constraint to which hit triplets (h_1, h_2, h_3) are originating from a real, physical track penetrating the SeaQuest spectrometer. The fTrkseeder algorithm makes heavy usage of this property. The purpose of the algorithm is two-fold. On one hand it is able to find and identify drift chamber hits which arise from muon tracks. On the other hand, it can also run in a mode which allows to reduce the raw hit sample so that only hits in the drift chambers which can be associated with a full track are kept. In this section, the details of the algorithm are presented.

4.2.1 Track Candidate Formation

The most important ingredient for the presented track finding algorithm fTrkSeeder is the correlation matrix. The correlation matrix from Section 4.1.5 is used as an input to the track finding algorithm. The matrix allows to judge the quality and validity of any given hit-triplet (h_1, h_2, h_3). From a list of "good triplets" a track candidate is formed. In the following section, the most important steps to combine hits to a track will be discussed.

Triplet Finding

The first step, fTrkSeeder is creating a list of all hit triplet combinations (h_1, h_2, h_3) in every view. It only accepts a triplet if the following criteria are fulfilled:

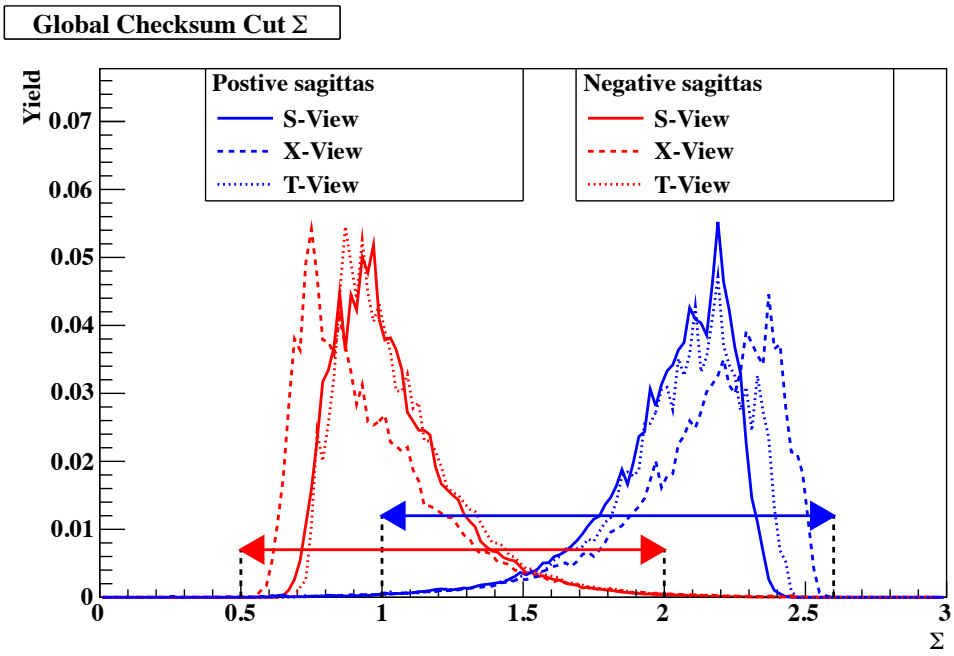

Figure 4.15: Cuts on the global checksum Σ as defined in Equation (4.2.1).

1) Global Checksum

The wire ID's of the hits within one hit triplet have to be within a given global checksum range. The chceksum accounts for hit patterns that match the acceptance criteria of the SeaQuest detctor. In order to obtain the checksum, the wire IDs are normalized to the total number of wires in each layer. Then, the checksum Σ is defined as

$$\Sigma = \frac{ID(h_1)}{N_{\text{Wires in Layer, Station1}}} + \frac{ID(h_2)}{N_{\text{Wires in Layer, Station2}}} + \frac{ID(h_1)}{N_{\text{Wires in Layer, Station3}}} \quad \text{with} \quad \Sigma \in [0,3]. \tag{4.2.1}$$

With help of Monte Carlo Studies the Σ was evaluated. Σ has to be with the following ranges

$$\begin{aligned} \Sigma = &\in [1.0, 2.5] \quad \text{for postive sagittas} \\ \Sigma = &\in [0.7, 2.0] \quad \text{for negative sagittas} \end{aligned} \tag{4.2.2}$$

Figure 4.15 shows the range and the obtained checksum Σ for triplets of muon tracks in the SeaQuest spectrometer. These cuts are motivated to increase the sensitivity for the `fTrkSeeder` to choose triplets from both "in-bender" muons and "out-bender" muons as shown in Figure 4.16.

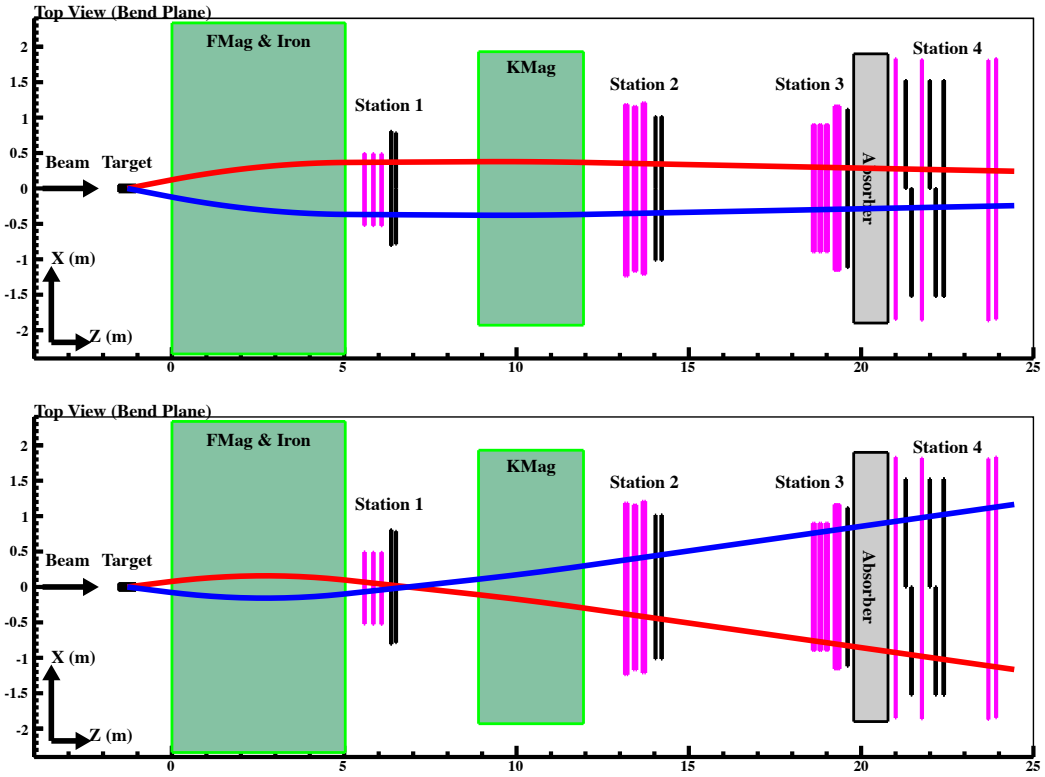

Figure 4.16: The two different track topologies of muon pairs in the SeaQuest spectrometer: muon pairs bending into the acceptance (top) and bending out of the acceptance (bottom).

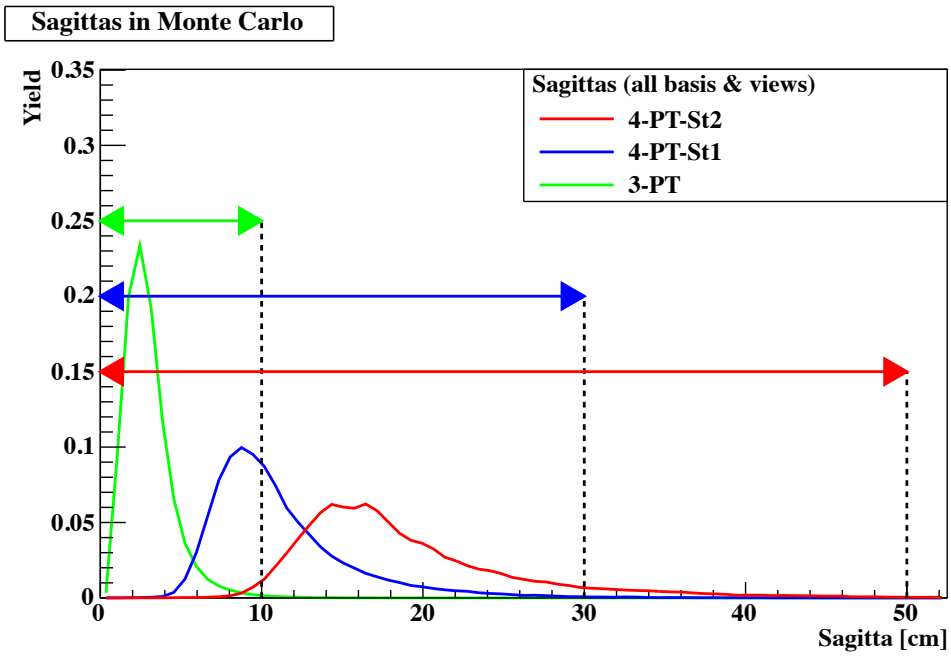

Figure 4.17: Absolute cuts on the sagitta values evaluated with Monte Carlo.

2) Sagitta Cuts

The sagitta cuts on the absolute sagitta values are motivated by the observation in section 4.1.4, especially Figure 4.5. A confirmation by Monte-Carlo can be seen in Figure 4.17. The sagittas which can be measured with one hit-triplet have to be within the following ranges

$$\begin{aligned} |s_{\text{4-PT-St1}}| &\leq 50\,\text{cm} \\ |s_{\text{4-PT-St2}}| &\leq 30\,\text{cm} \\ |s_{\text{3-PT}}| &\leq 10\,\text{cm}. \end{aligned} \tag{4.2.3}$$

`fTrkSeeder` requires all sagittas to have the same sign (either negative or positive).

3) Correlations of Sagittas

The three sagittas which can be accessed within one hit-triplet $(h1, h_2, h_3)$, have to be well correlated. This means that their ratios c_{ij} have to match within a 3σ-range. The correlation coefficient c_{ij} and σ is compared with $\langle c_{ij} \rangle$ obtained from the correlation matrix in Section 4.1.5. Altogether 6 correlation checks are performed, the auto-correlation check (i.e. c_{ii}) is skipped.

Combination of Triplets in the same View: Sextets

Two hit-triplets, s_i and s_j, from the same views are combined to a hit sextet, when the following criteria are fulfilled:

- The hit in Station 3 must be from the same Station 3, i.e. Plus or Minus. Plus means top side and Minus means bottom side.
- Sagitta correlations c_{ij} have to match within a 3σ-range. For two distinct triplets, all three sagittas are compared with all three sagittas of the other triplet. Altogether there are 9 correlation checks.
- The two triplets must have at maximum 2 common hits. Triplets are prioritized so that sextets with least amount of common hits are favored.
- If the triplet hits within one station are from the same sister plane, such as a primed and un-primed combination, the difference in the element ID's $\Delta_{ij} = ID_{h_1^i} - ID_{h_1^j}$ must be $|\Delta_{ij}| \leq 2$. Figure 4.18 illustrates this cut.

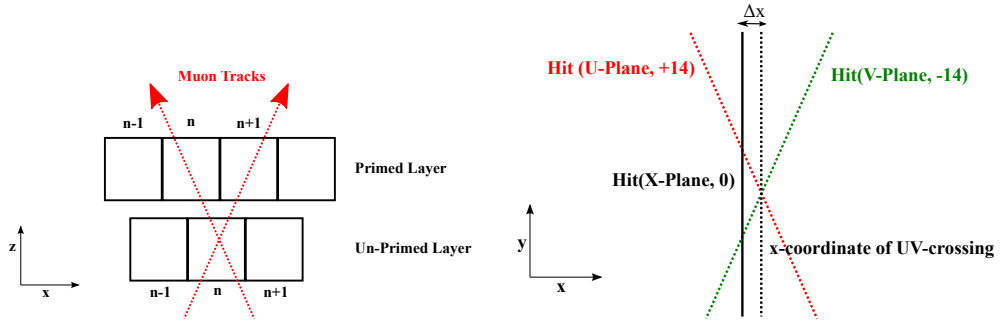

Figure 4.18: Left: The element-ID cut used in combining triplets to sextets. The cut implies that a track may only hit directly adjacent wire cells. Right: The tilted wires of a track candidate must predict the position of the un-tilted wire within a tolerance Δx.

- The difference in the 3-PT sagitta measurements must be $|s^i_{\text{3-PT}} - s^j_{\text{3-PT}}| \leq 2\,\text{cm}$. This cut forces that the triplets have a similar momentum measurement estimate (see previous Section).

Combination of Sextets from different Views

Two hit sextets from different views are combined when the following criteria are successfully checked:

- All sagitta correlations c_{ij} of different sextets have to be within a 3σ-range.
- All wires within one Station intercept in the x-y plane.
- If the triplet hits within one station are from the same sister plane, such as a primed un-primed combination, the difference in the element ID's $\Delta_{ij} = ID_{h^i_1} - ID_{h^j_1}$ must be $|\Delta_{ij}| \leq 2$. Figure 4.18 illustrates this cut.
- The difference in the 3-PT measurement $|s^i_{\text{3-PT}} - s^j_{\text{3-PT}}| \leq 2\,\text{cm}$. This cut forces that the triplets have a similar momentum measurement estimate (see previous Section).

Final Track Candidate

A track candidate is declared when at least three sextets could be matched and the amount of distinct hits is either 5 or 6 per station. The associated hits in the tilted planes of each station have to predict the hits within the untitled plane with a tolerance Δx of 1.5 cell-spacings. Figure 4.18 illustrates the prediction scheme graphically (right side).

4.2.2 Track Finding Efficiencies

A very important characterization of a track finding algorithm is to estimate its efficiencies in Monte-Carlo. For the following study, the same GEANT4 Monte Carlo was used as in Section 4.1.6. Monte Carlo productions at SeaQuest take noise effects in the digitization process into account. Most noise effects arise from cross-talk or δ-ray effects. These effects were characterized based on data and then built in the digitization step of the Monte Carlo. Drift chamber hits can also be caused by secondary particles which are created when one of muons interacts with detector material, in particular in the FMAG iron. The dimuon detection efficiency is defined as follows

$$\varepsilon_{\text{Detection}} = \frac{N_{\text{dimuon}}}{N_{\text{all}}}, \tag{4.2.4}$$

where N_{dimuon} is number of drift chamber hits caused by one of the two (Drell-Yan-) muons per event, and N_{all} is the total number of hits in the Monte Carlo event. The background particle suppression efficiency is defined as

$$\varepsilon_{\text{BKG}} = 1 - \frac{N_{\text{BKG}}^{\text{After}}}{N_{\text{BKG}}^{\text{Before}}}, \tag{4.2.5}$$

where $N_{\text{BKG}}^{\text{Before}}$ is number of drift chamber hits caused by secondary particles. $N_{\text{BKG}}^{\text{After}}$ is the number of hits caused secondary particles which are accidentally associated with a muon track candidate. Similarly, the noise suppression efficiency is defined in the following

$$\varepsilon_{\text{Noise}} = 1 - \frac{N_{\text{Noise}}^{\text{After}}}{N_{\text{Noise}}^{\text{Before}}}, \tag{4.2.6}$$

where $N_{\text{Noise}}^{\text{Before}}$ is number of drift chamber hits caused by cross-talk or δ-rays. $N_{\text{Noise}}^{\text{After}}$ is the number of hits caused by detector noise which are accidentally associated with a muon track candidate.

Figure 4.19 shows the above defined efficiencies as a function of number drift chamber hits (summed over all stations) N. The detection efficiency $\varepsilon_{\text{Detection}}$ behaves rather flat over the complete range of N. The average dimuon detection efficiency is $(98.6 \pm 2.4)\%$. `fTrkSeeder` seems to be very robust in associating the correct hits to track candidates. The background particles suppression efficiency ε_{BKG} reaches an average value of $(84.1 \pm 18.2)\%$. Although this value is rather high, the high fluctuation suggests that the Monte Carlo model requires some refinement. Finallly, the detector noise suppression efficiency $\varepsilon_{\text{Noise}}$ reaches an average value of $(79.2 \pm 27.8)\%$. In summary, the `fTrkSeeder` has a intelligence to

associate the correct muon hits with final track candidates, while being at the same time fairly powerful in the rejection of unwanted hits caused by detector noise or background particles.

Besides the efficiencies, there is another way to characterize the quality of final track candidates in terms of purity. The purity is defined as the following fraction

$$p = \frac{N_{\text{dimuons}}}{N_{\text{all}}}, \tag{4.2.7}$$

where N_{dimuons} is the number of hits per event caused by the muons and N_{all} is the number of all drift chamber hits in the SeaQuest detector. Figure 4.20 shows the purity after fTrkSeeder processed the Monte Carlo event plotted versus the original purity. It can be stated that fTrkSeeder constantly improves the purity per event.

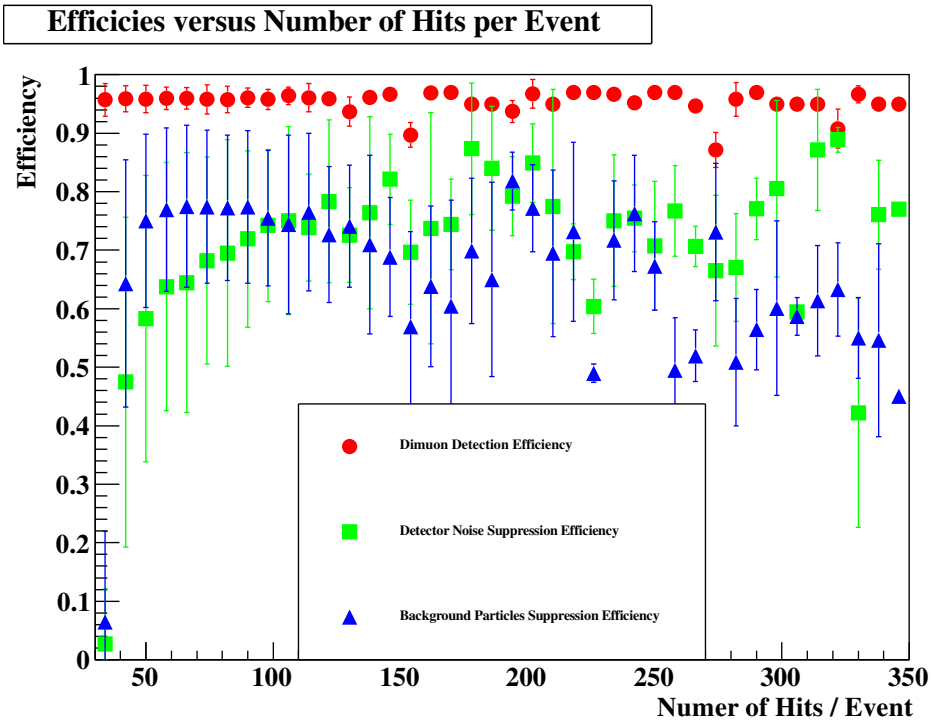

Figure 4.19: The detection efficiency $\varepsilon_{\text{Detection}}$ (red), the background particles suppression efficiency ε_{BKG} (blue), the detector noise suppression efficiency $\varepsilon_{\text{Noise}}$ as a function of the total number of drift chamber hits per event.

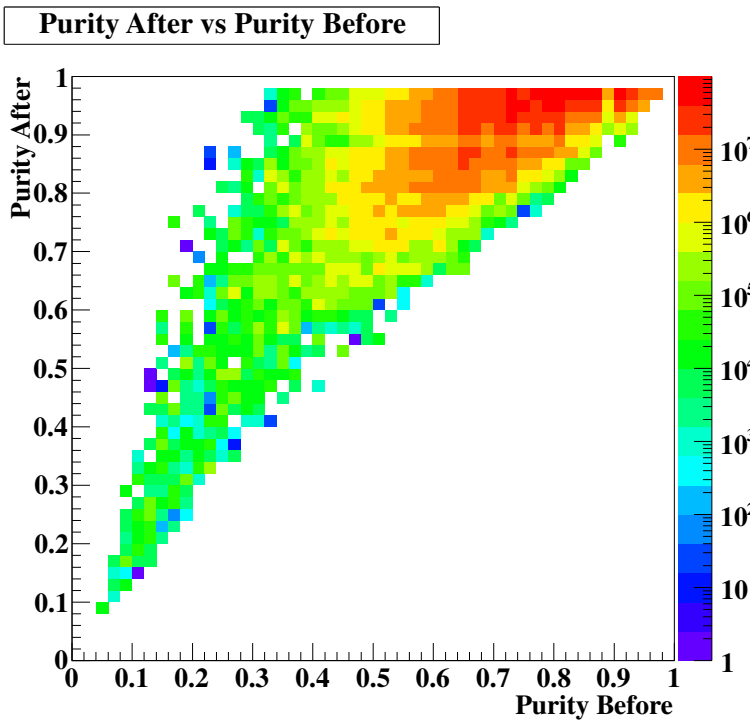

Figure 4.20: The event purity after `fTrkSeeder` processed the event versus original event purity denoted as 'purity before'. `fTrkSeeder` improves the purity of hits in one event.

4.3 sqerp - The Track Fitting Software at SeaQuest

4.3.1 The Track Parametrization

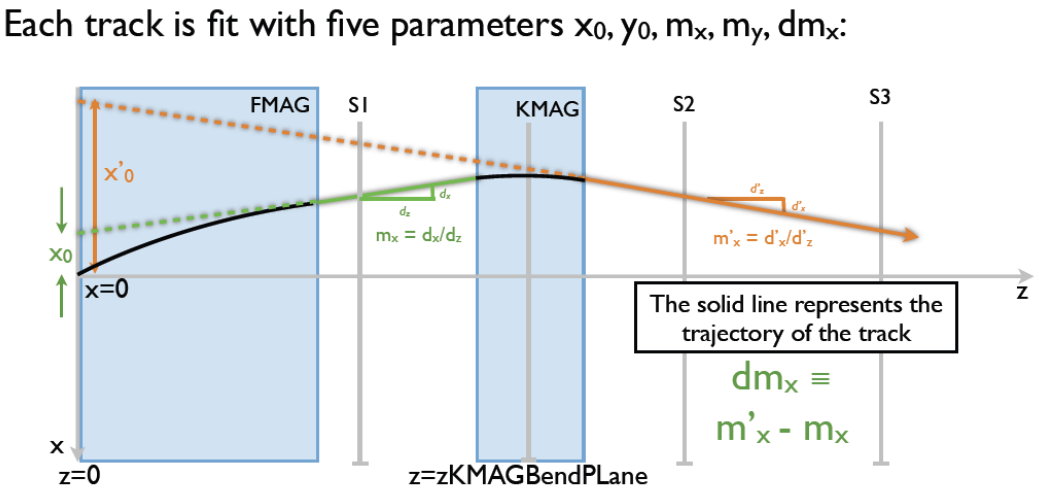

Figure 4.21: The track parametrization for the SeaQuest detector is divided in two, one for the front part of the detector with Station 1, and the other for the back part of the detector, including Stations 2 and 3.

The purpose of the track fit is to determine the most accurate estimates of the track parameters together with the corresponding covariances. For this purpose `sqerp` is used. `sqerp` is an acronym for "SeaQeust Event Reconstruction Program" and is the standard track fitting software at SeaQuest. A track is modeled and parametrized by a collection of straight line segments, tangent to the particle's trajectory. These straight line segments are called track states. As all tracks in SeaQuest can be regarded as going in the forward direction, it is natural to parameterize the track states as a function of the z coordinate. A track state is defined by a position and a tangent direction at a given z. This results in four track parameters. Furthermore, a fifth parameter, dm_x, is added to include the momentum measurement obtained from the curvature in the magnetic field. In all cases, only single charged particles are considered, i.e., $q = \pm 1$. Conveniently, the state vector is chosen as follows

$$\vec{x} = \begin{pmatrix} x \\ y \\ m_x \\ m_y \\ dm_x \end{pmatrix} \quad \text{with} \quad m_x = \frac{\partial x}{\partial z}, \quad \text{and} \quad m_y = \frac{\partial y}{\partial z} \quad . \tag{4.3.1}$$

The corresponding errors on $\vec{x}$ are given by a 5×5 state covariance matrix, C. The state vector and its covariance matrix are commonly referred to as the track state. As shown in Figure 4.21, there are two track states in the SeaQuest spectrometer: one for the front part of the spectrometer ($\vec{x}$), and one for the back part of the spectrometer ($\vec{x'}$). In the following paragraphs, the track state will always be referred as $\vec{x}$. The projection for the state vector and its covariance matrix at the k^{th} drift chamber layer is obtained from an initial rough state estimate, $\vec{x}_0$, using the propagation relation:

$$\vec{x}_k = f_k(\vec{x}_0) \quad , \tag{4.3.2}$$

$$C_k = C_0 F_k^T . \tag{4.3.3}$$

In this notation, $\vec{x}_k$ refers to a projected state vector. The location of the track states can be chosen anywhere along the trajectory. In the track fit, it is useful to determine the states at the measurement planes. The combination of a measurement and a track state is referred to as a node. The transport of a state the initial node 0 to a state at node k is described by the propagation relation

$$\vec{x}_k = f_k(\vec{x}_0) \quad , \tag{4.3.4}$$

where f_k is the track propagation function. The actual function f_k depends on the chosen propagation method. For a straight line extrapolation, f_k simplifies to

$$f_k(\vec{x}_0) = F_k \vec{x}_0 \quad , \tag{4.3.5}$$

where F_k is the transport matrix given by

$$F_k = \begin{pmatrix} 1 & 0 & \Delta z & 0 & 0 \\ 0 & 1 & 0 & \Delta z & 0 \\ 0 & 0 & 1 & 0 & 0 \\ 0 & 0 & 0 & 1 & 0 \\ 0 & 0 & 0 & 0 & 1 \end{pmatrix} \quad \text{with} \quad \Delta z = z_k - z_0 \quad . \tag{4.3.6}$$

The measurements provide information about the trajectory at each layer. The projection equation describes the relation between a measurement, m_k, and a track state as

$$m_k = h_k(\vec{x}_k) + \varepsilon_k \quad , \tag{4.3.7}$$

where h_k is the projection function, and ε_k the measurement noise. For example, in case a detector directly measures the x coordinate of a track state, h_k simplifies to

$$h_k(\vec{x}_k) = H_k \vec{x}_k \quad , \tag{4.3.8}$$

where the measurement matrix, H_k, is given by

$$H_k = \begin{pmatrix} 1 & 0 & 0 & 0 & 0 \end{pmatrix} \quad . \tag{4.3.9}$$

Since the detection planes in SeaQeust measure only one coordinate, the projection matrix, H, is a 1×5 matrix. The uncertainty in ε_k in described by the covariance matrix $V_k \equiv \mathrm{cov}(\varepsilon_k)$. In case of an one-dimensional measurements, V_k is simply the measurement error squared.

4.3.2 The Track Fitting

In order to make the first projection, the track fit requires an estimate for the initial track state, $\vec{x}_0$ which is estimated at $z = 0$. This estimate is evaluated by an initial loose fit of a track candidate without taking drift distances of the corresponding hits into account. The residual is the distance between the measurement, m_k, and the state vector in the measurement plane. The projected residual and its covariance matrix are given by

$$r_k = m_k - h_k(\vec{x}_0) \quad , \tag{4.3.10}$$

$$R_k = V_k + H_k C_k + H_k^T \quad . \tag{4.3.11}$$

The expected variance, R_k, has a contribution from both the covariance matrix of the track state, C_k, and the measurement variance, V_k. The predicted contribution of all measurements (=number of hits which are included in the fit) to the total χ^2 equals

$$\chi^2 = \sum_k r_k \left(R_k\right)^{-1} r_k \quad . \tag{4.3.12}$$

The purpose of the fit is to find the optimal track states that give a minimal χ^2. A more intuitive way to write χ^2 is

$$\chi^2 = \sum_k \frac{r_k^2}{\sigma_k^2}, \quad . \tag{4.3.13}$$

where σ_k is the spatial single-layer resolution in the detector plane k and $r_k = h_k - m_k$ the residual. In order to determine the residual of a measurement, the state vector is projected onto the measurement space. At the drift chambers at SeaQuest, a measurement can be represented by a straight line corresponding to the central coordinate of a hit. The residual is the distance between this line and the intersection point of the track state with the sensor plane. This results in a linear projection function. For each of these measurements, which measure a coordinate in a plane at fixed z, the projection function can be expressed as

$$h_k(\vec{x}_k) = x\cos\alpha_S + y\sin\alpha_S\,, \tag{4.3.14}$$

where α_S is the rotation (stereo) angle with respect to the y axis. The projection onto drift chamber measurement, which depends on the distance of closest approach to the wire, is given by a non-linear equation. The closest distance of a state $\vec{x}$ to a wire in an x-layer is given by the projection relation:

$$h_k(\vec{x}) = (x - x_{\text{wire}})\cos\theta = \frac{x - x_{\text{wire}}}{\sqrt{1+t_x^2}} \quad , \tag{4.3.15}$$

where x_{wire} is the x coordinate of the wire, and θ is the track angle with the z axis in the x-z plane. This expression is non-linear in the track parameter t_x.

4.3.3 Momentum Estimation with the p_T-Kick Method

The momentum of a track candidate can be estimated assuming that the muon is originated from the interaction point. This method, known as the p_T-kick method, is based on the idea that the effect of the magnetic field can be described by an instant kick of the momentum vector in the center of the magnet. In general, the actual momentum kick, Δp_x, depends on the integrated magnetic field along the particle's trajectory:

$$\Delta\vec{p} = q\int d\vec{l}\times\vec{B}\,. \tag{4.3.16}$$

The main component, Δp_x, provides the highest precision on the momentum. In terms of the track parameters this relation becomes:

$$\Delta p_x = p_{x,f} - p_{x,i} = p\left(\frac{m_{x,f}}{\sqrt{1+m_{x,f}^2+m_{y,f}^2}} - \frac{m_{x,i}}{\sqrt{1+m_{x,i}^2+m_{y,i}^2}}\right) \tag{4.3.17}$$

where the subscript $m_{x,f}$ and $m_{y,f}$ are the slopes of the track candidate. They are

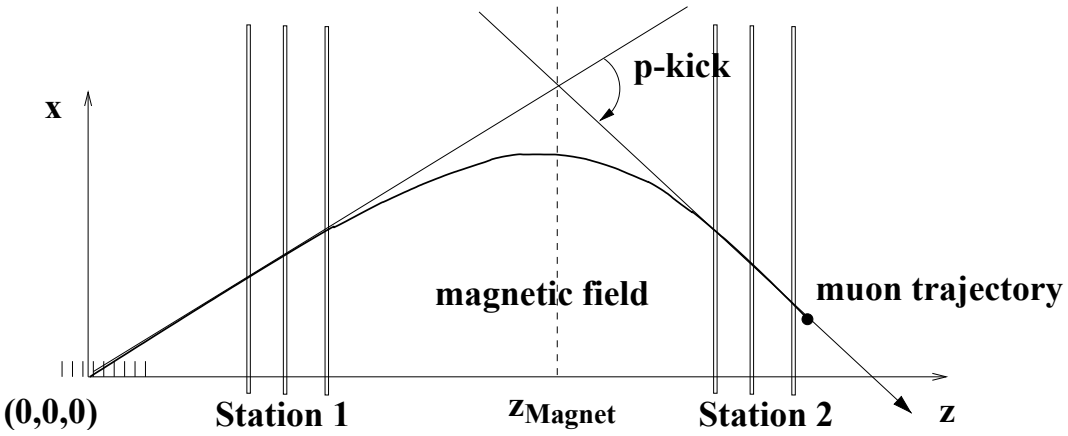

Figure 4.22: Schematic drawing of the p_T-kick method (not to scale). The effect of the magnetic field is approximated by a instant kick at z_{Magnet}. The difference in slopes are used to estimate the actual momentum.

known from the initial rough fit to the wire positions, and are evaluated at the magnets effective bend plane $z_{\text{zKMAGBendPLane}}$ (see Figure 4.21). The slopes before the magnet are $m_{x,i}$ and $m_{y,i}$. Note that the charge of the particle, q, is determined from the sign of curvature and the field polarization. However, `sqerp` utilizes averaged Δp_x-values based on simulations of the magnetic fields of the two dipole magnets, and does not evaluate the integrated magnetic field effectively traversed by the muon. Figure 4.22 shows a schematic of the p_T-kick method.

4.3.4 The Swim Method for Vertex Determination

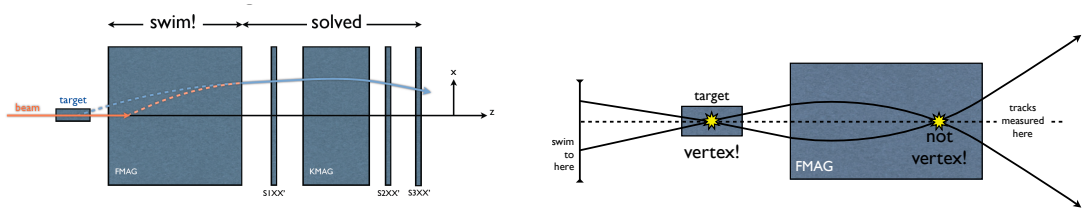

Figure 4.23: Schematic of the vertex determination by *sqerp*.

Unlike KMAG, FMAG is made of solid iron. In that iron, muons multiple scatter and lose energy due to ionization. A typical 40 GeV muon leaves about 7 GeV in the iron. The curvature deflection of the track within the FMAG is a function of the momentum of the muon. The energy loss Δp can be parameterized by the particle's momentum p. Figure 4.24 shows the parametrization evaluated with Monte Carlo. The energy loss is parametrized as linear function. The iron is divided into a finite amount of small volumes. At each of these volumes a deflection correction is applied and energy added back to the muon. Every track is stepped through every single volumes of iron and back through the target. All steps are stored and the upstream-most closest approach to the beam axis is considered to be the vertex of

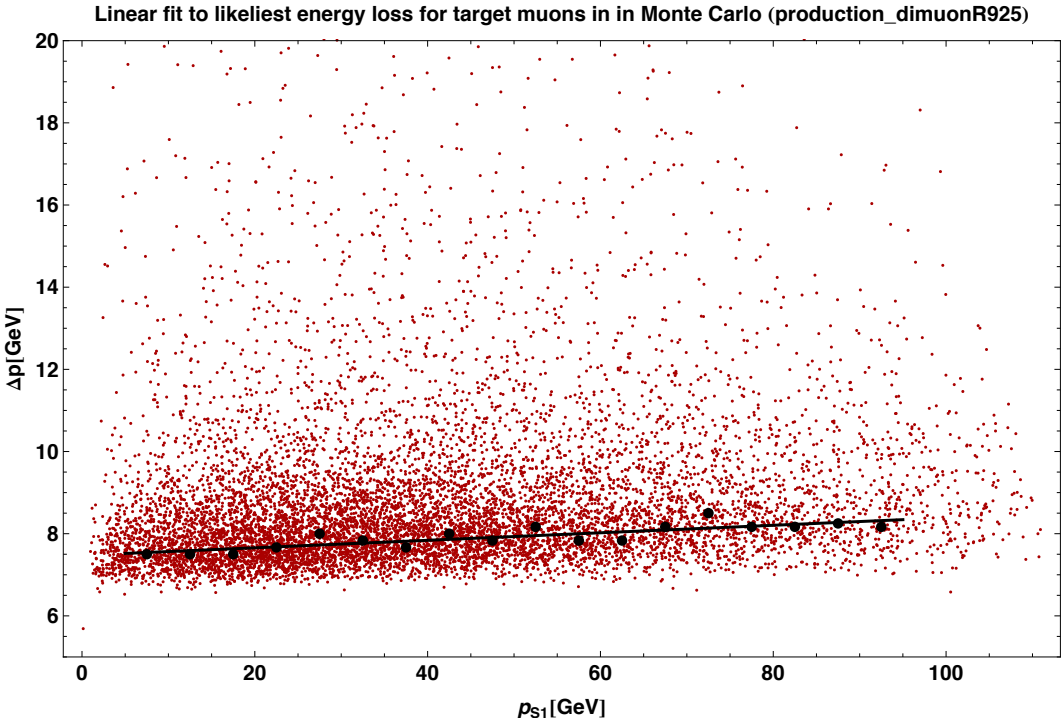

Figure 4.24: Linear fit of the likeliest energy loss in every momentum bin.

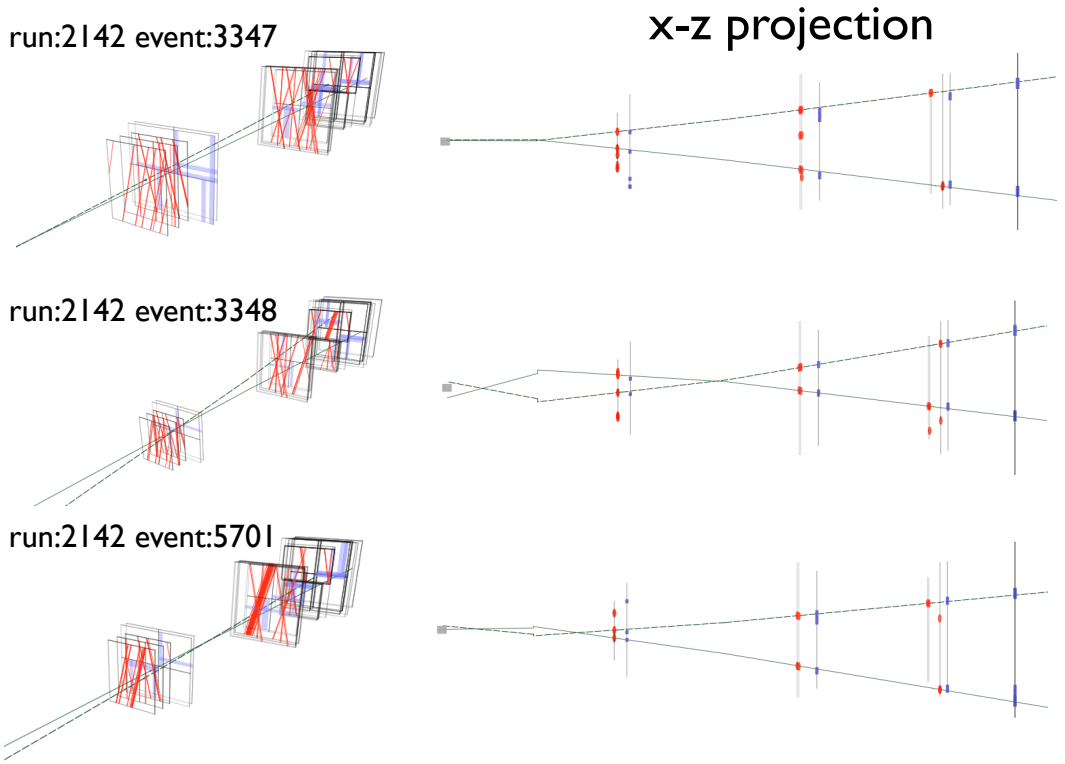

Figure 4.25: Event displays of reconstructed dimuon events. 3D view with chamber hits in red and hodoscope hits in blue can be seen on the right, a $x-z$-projection on the right.

the track. Then the position and momentum coordinates of the track at this point are determined. Dimuons can be constructed by pairing positive and negative tracks from the same event which meets various quality criteria (see next Chapter). Kinematics are then computed using the sum of the two separate muons' four-momenta. i.e. the four-momentum of the dimuon. Based on this, all relevant dimuon kinematics can be computed, like e.g. x_b, x_t as shown in Section (2.2.2). Examples of reconstructed dimuons can be seen in Figure 4.25.

Chapter 5

Data Analysis

5.1 Outline of the Analysis

A C++ based analysis framework was used to replay the raw data, process the data with the track finder `fTrkSeeder` and call the SeaQuest reconstruction software `sqerp`. The framework has been developed and maintained by Tokyo Institute of Technology and is based on ROOT [76]. ROOT is a powerful object-oriented framework that has been developed at CERN by and for the nuclear and particle physics community. From the replayed data files, called "default data set", the track finding algorithm `fTrkSeeder` was processing the raw events and creating a new data set optimized for track reconstruction, called "seeded data set".

The flow-chart of the analysis procedure is illustrated in Figure 5.1. The raw hit data recorded from the detectors were first transformed into ROOT files by the Analyzer after calibration. In the "Default Method" the default data set was directly passed to the track fitter `sqerp`. In the "Improved Method", the "seeded data sample" was passed to the track fitter which results in much higher yields in the track reconstruction. In the track fitting procedure `squerp`, all relevant dimuon relevant kinematic variables were extracted. In the following analysis, the default method and improved method will always be compared.

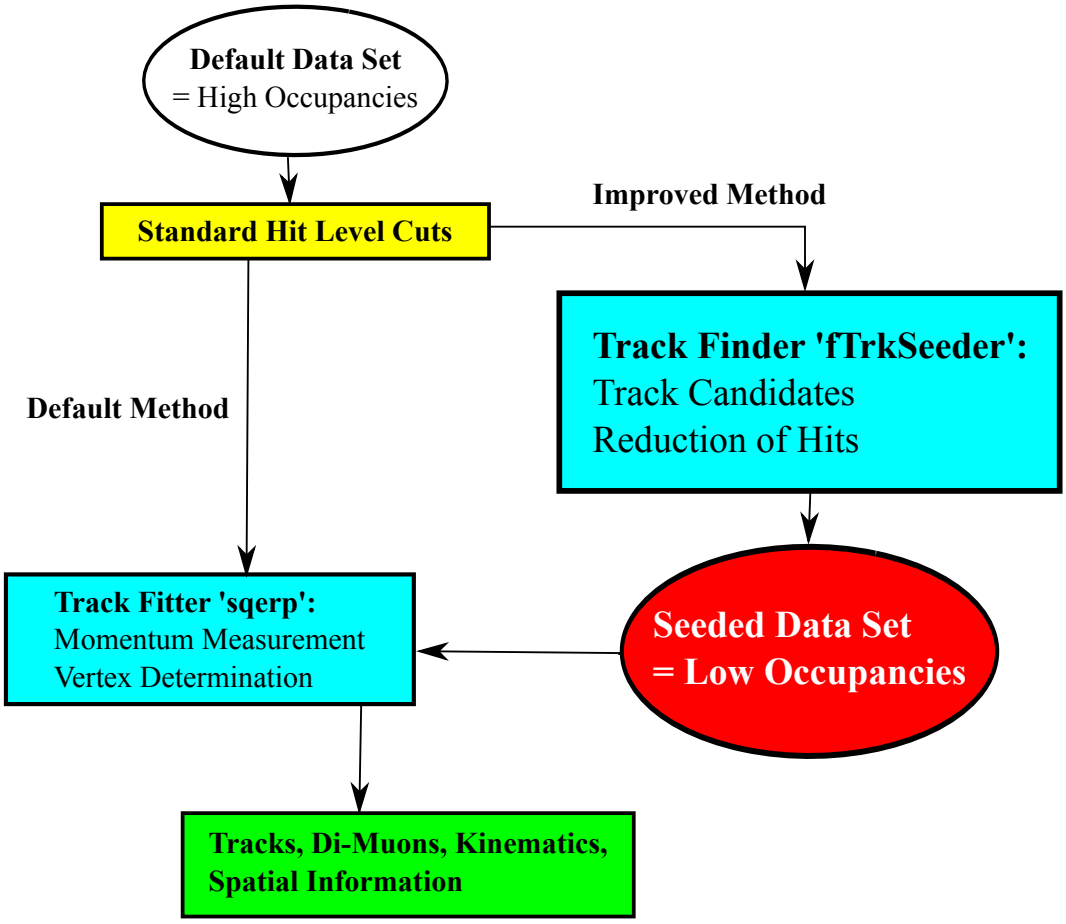

Figure 5.1: The flow chart of the presented track reconstruction at SeaQuest.

5.2 Motivation of the Analysis

The purpose of the presented analysis is to provide methods to deal with the data during the commissioning run of the SeaQuest in 2012. The problem during the commissioning run (March/April 2012) was the time structure of protons from the accelerator. As the result, on the experimental side, we observed high multiplicity/occupancy events. They are commonly referred to as SPLAT (as in what happens when a tomato is thrown at a wall) event. Because of these events, the track reconstruction was difficult. In typical SPLAT events, a large fraction of drift chamber wires and hodoscope scintillators fired. Figures 5.2 - 5.5 show the average occupancy per event for each recorded data set. In particular the drift chambers located closer to the beam interaction region (Station 1 & 2) showed average occupancies between 30% and 60%.

For the purpose of monitoring the beam quality at high frequencies, SeaQuest installed what is commonly called the scalerDAQ, which is independent of the mainDAQ where the TDCs are installed. The scalerDAQ is a VME/CODA system with a sis3610 standalone trigger board triggered by a gate generator pulsing at 7.3 kHz. It had one 32 bit 140 MHz VME scaler installed to monitor one of the hodoscope planes at the trigger frequency (7.3 kHz). The assumption that goes into this setup is that the raw rates seen on the hodoscopes were dictated by the intensity of the beam. We can therefore monitor the beam intensity at 7.3 kHz in order to find by what frequencies the beam is diluted. The 360 Hz component likely is a remnant of a 3-phase electric power that is also being used in the Main Injector.

As a result of detailed studies, most of the events that satisfied the dimuon roads were coming from random coincidences occurring inside the SPLAT event. The raw rates of the hodoscopes showed intensity fluctuations ranging over 3 orders of magnitude. This caused several problems for the experiment:

- The high intensity beam buckets cause SPLAT in the detectors
- Since the high intensity buckets cause SPLAT, they have a higher probability of (accidentally) satisfying the trigger roads. Therefore, the DAQ has a high probability of being triggered by SPLAT events.
- Since the dominant frequency is 360 Hz (or 2.8 ms time interval), and the DAQ deadtime being $\approx$ 1.2 ms, and since the DAQ is preferentially triggered at the peak of the high intensity buckets, it was dead for a significant portion of the section of beam where the beam intensity reduces rapidly, and where

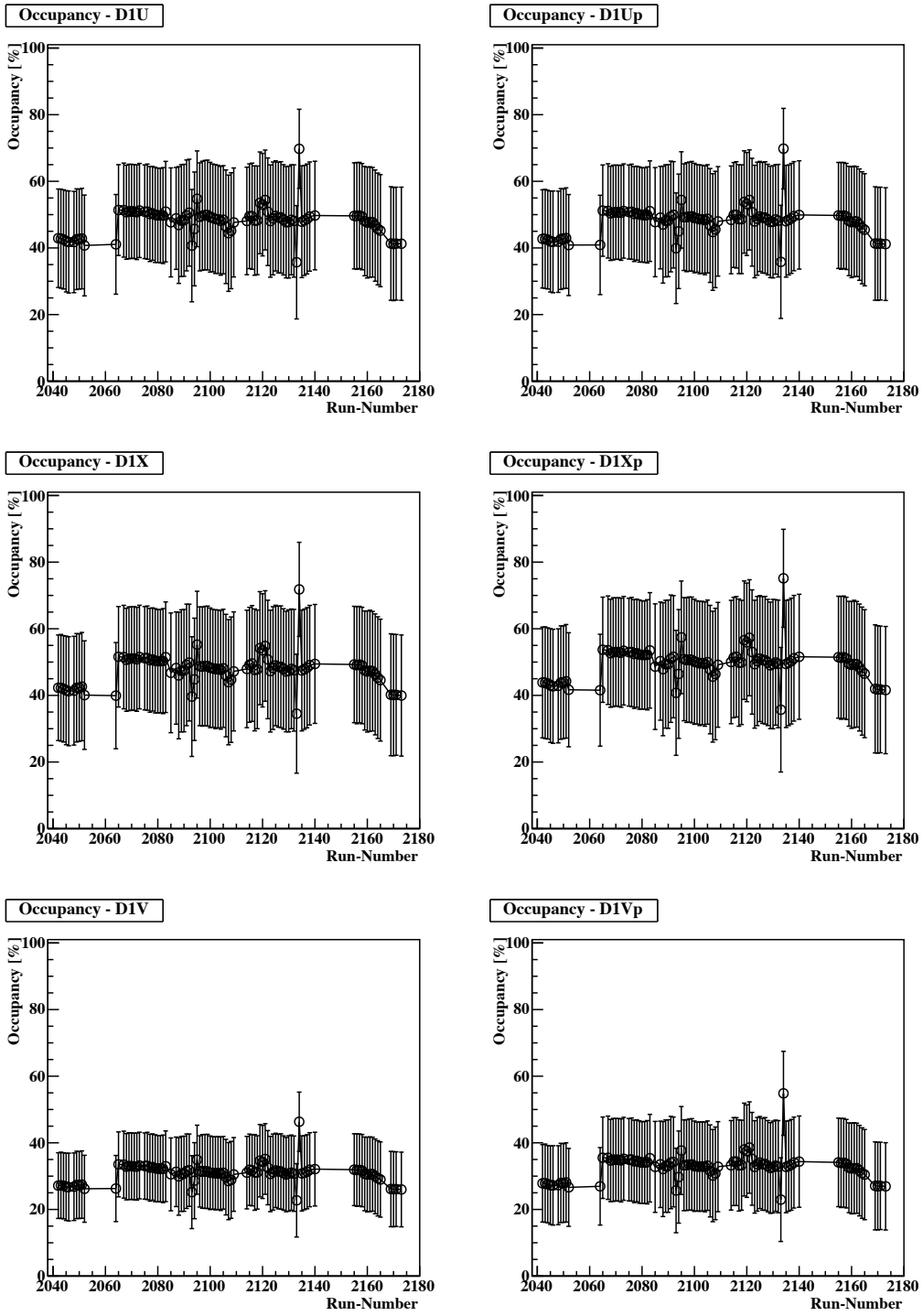

Figure 5.2: All layers of Station 1: Occupancy versus time during the commissioning run.

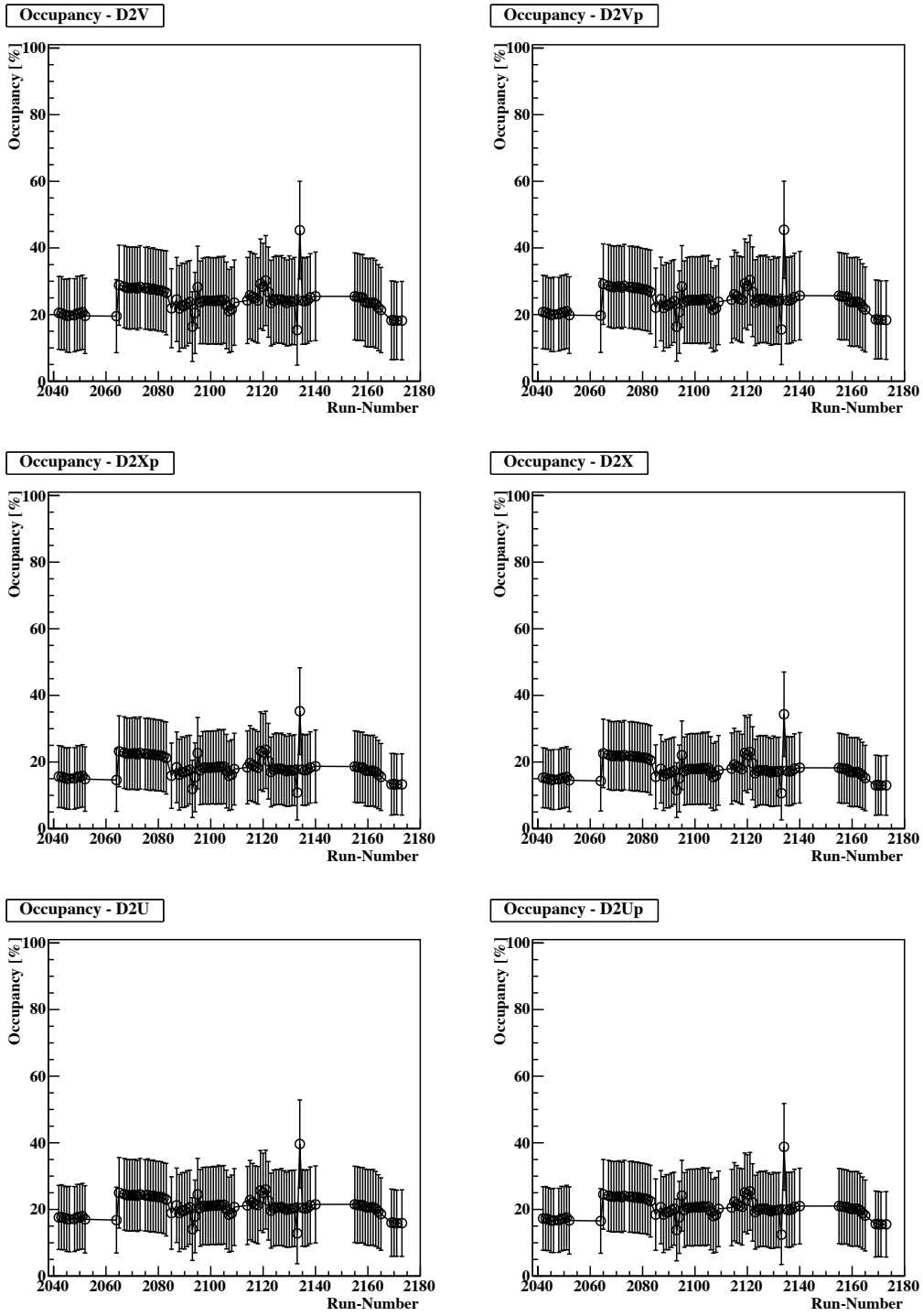

Figure 5.3: All layers of Station 2: Occupancy versus time during the commissioning run.

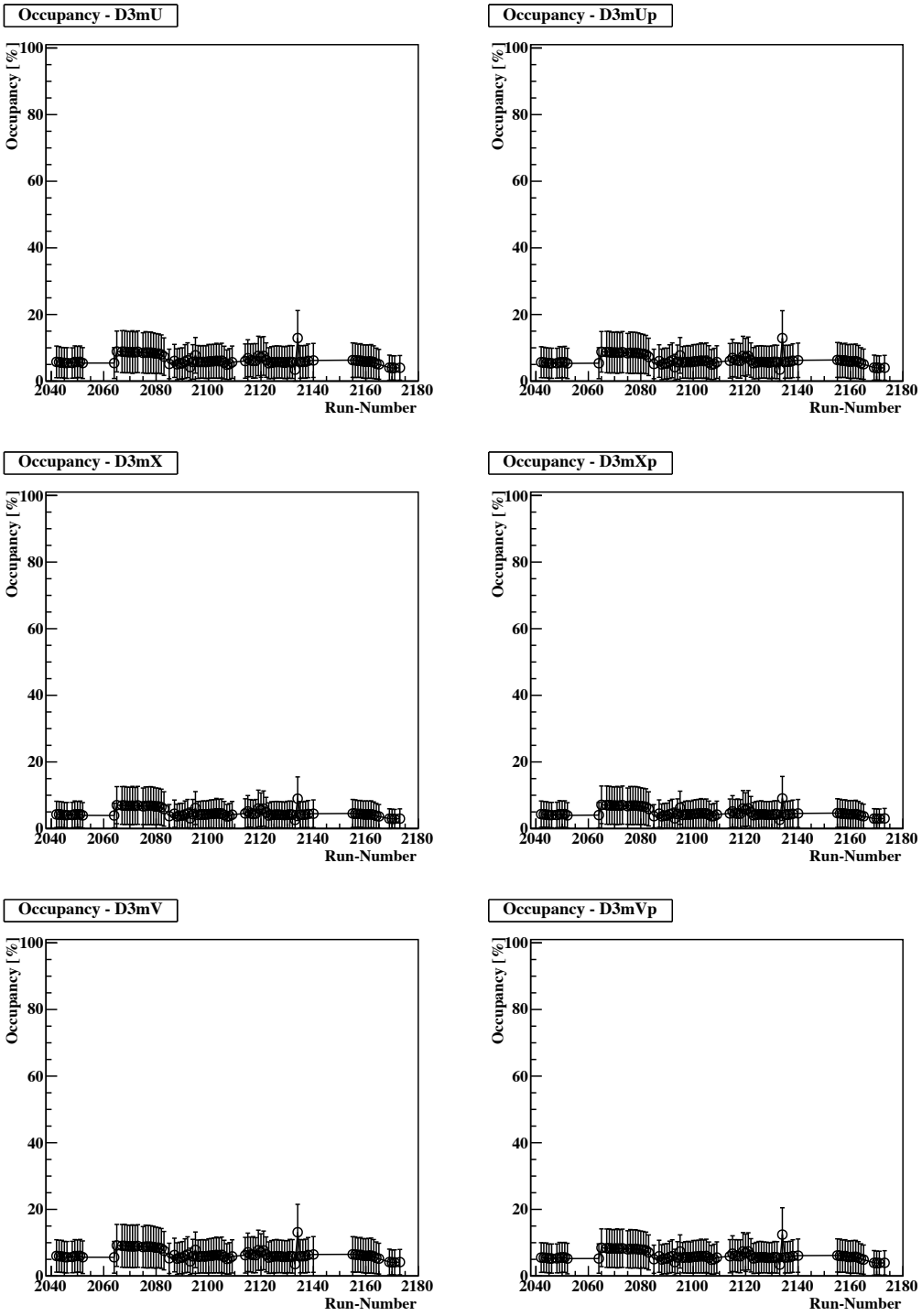

Figure 5.4: All layers of Station 3 Minus: Occupancy versus time during the commissioning run.

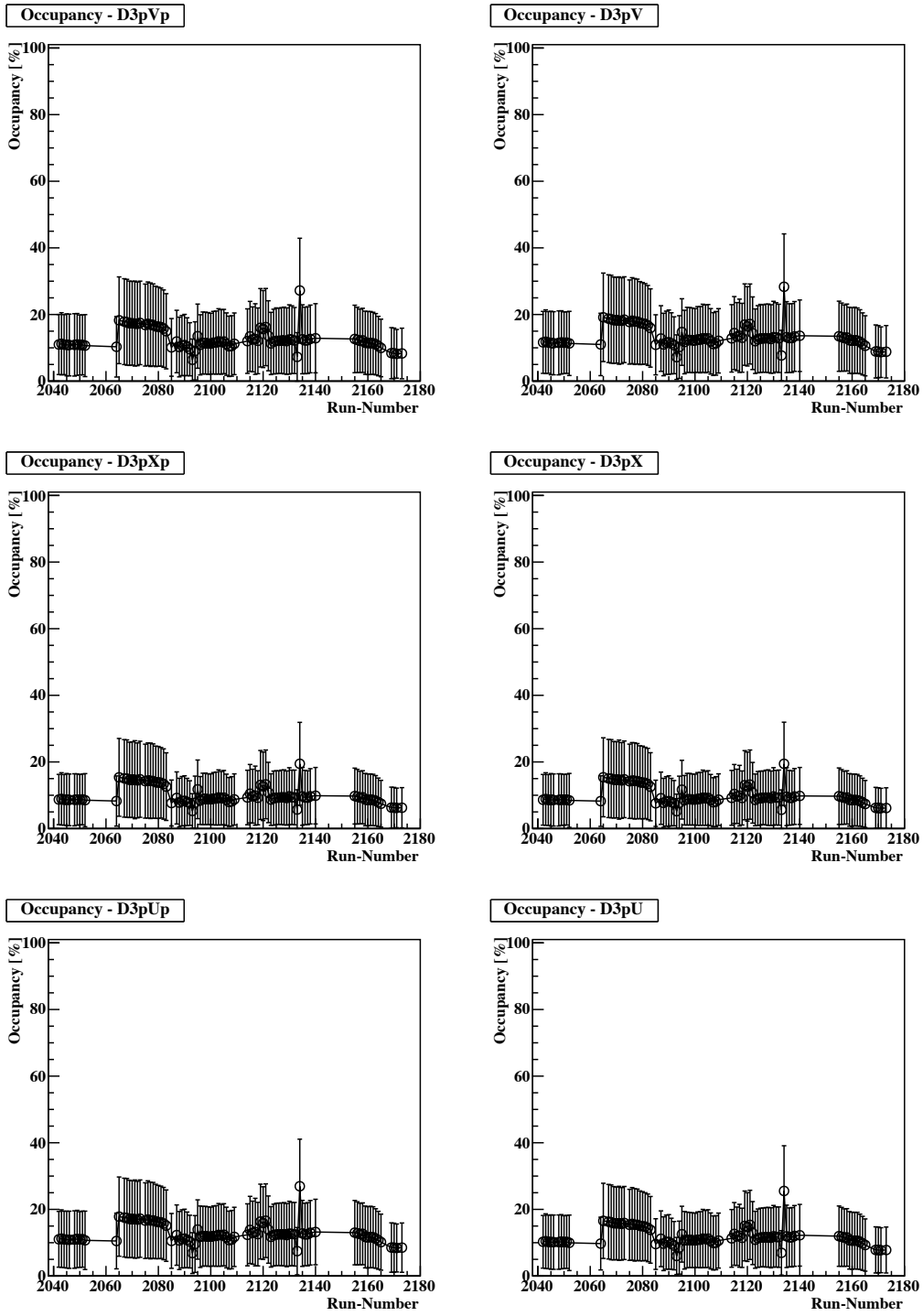

Figure 5.5: All layers of Station 3 Plus: Occupancy versus time during the commissioning run.

lower intensity beam can be seen. Coincidentally, these lower intensity sections of the beam are where one could expect better data, where SPLAT is not a problem.

It should be noted that the Memorandum of Understanding (MOU) between Fermilab and the SeaQuest collaboration require an average duty factor of 60 %, where spills below 25 % are not counted as "beam used". The duty factor q is defined as

$$q = \frac{\langle I \rangle^2}{\langle I^2 \rangle} \quad \text{with} \quad I = \sum_{N_{\text{spill}}} N_{\text{X2T}} \tag{5.2.1}$$

with N_{X2T} being the number of hits in the X2T hodoscope and N_{spill} being the number of triggered events within one spill. Figure 5.6 shows the average duty factor per 5 s spill for the last weeks of commissioning. The average duty factor during the last weeks of beam was 18.5 %. Figure 5.7 shows the distribution of the duty factor.

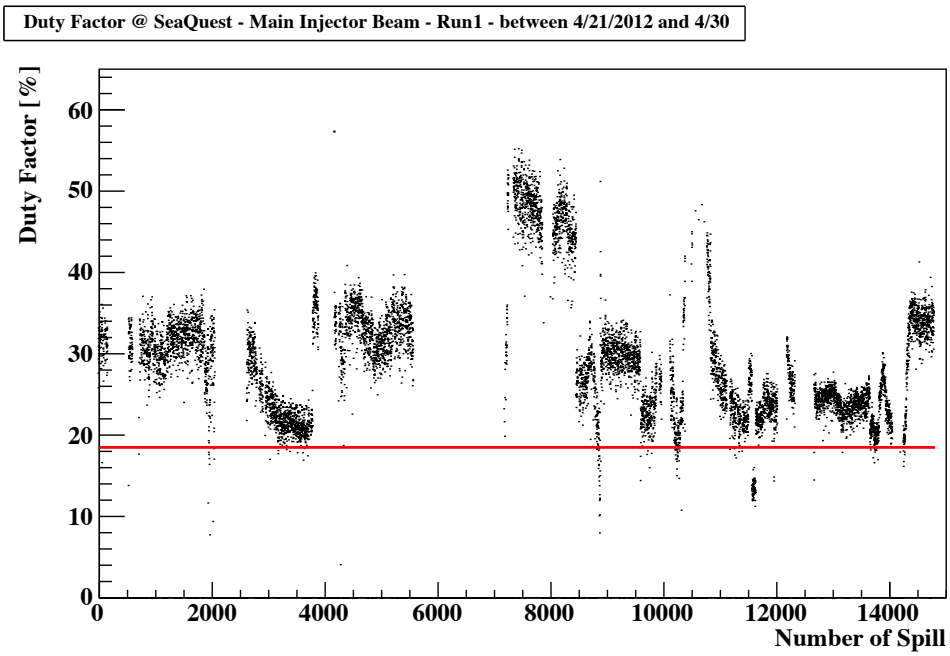

Figure 5.6: The duty factor during the last weeks of the commissioning run at SeaQuest. The black points show the duty factor per spill, the red line shows the average duty factor over the shown period of time. When there is no point shown, the duty factor was 0%.

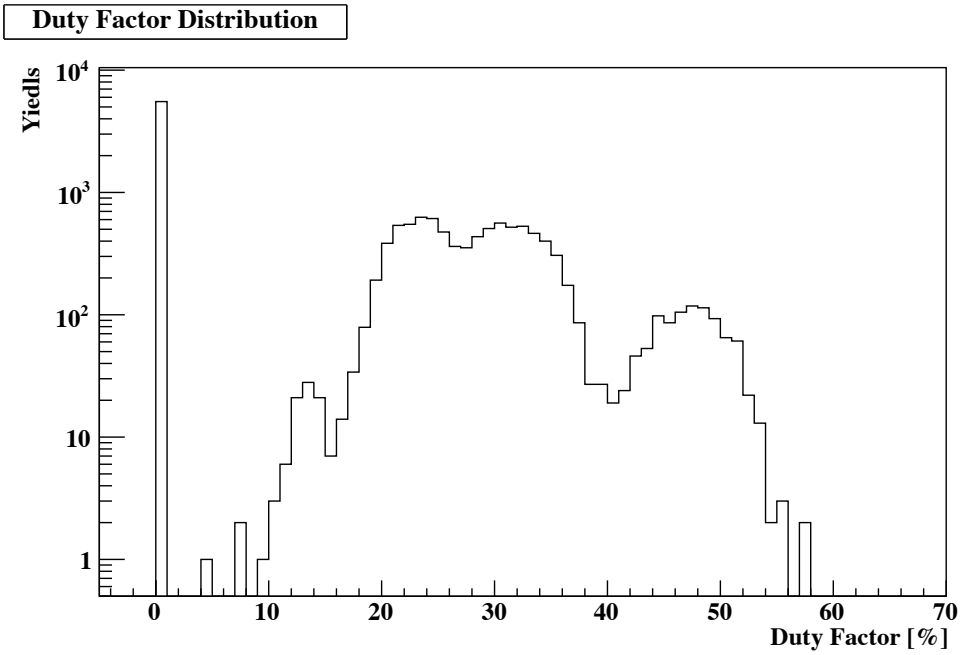

Figure 5.7: Distribution of the duty factor per spill. Note the logarithmic scale and the abundance of spills at a duty factor of 0 %.

5.3 Trigger and Run Selection

For the analysis presented in this thesis, all runs, which were recorded with the dimuon trigger FPGA-1, are used. It is a total of 93 runs which are combined to sets of equal amount of events. The combined data set contain 1.25×10^6 triggered events. A summary of the runs and data sets can be seen in Table 5.1.

5.3.1 Standard Hit-Level Cuts

All the events in the mentioned data sets are raw hit-level events. For the analysis presented, the following hit level cuts were applied to all raw events:

- In-time Cuts:
  Both drift chamber and hodsocope hits are required to be in-time with respect to the read-out window of the DAQ system. The readout windows are specified for each drift chamber and hodoscope array.

- After-Pulse-Removal:
  In case in one event, one drift chamber wire had multiple hits, only the earliest hit with respect to read-out window was selected. This accounts particularly for noisy read-out electronics causing after ringing hits.

- Hodoscope Masking:
  Only drift chamber hits were considered which were masked by an active hodoscope paddle. A tolerance of 10 cm was allowed in order to account for the mis-alignment of the detectors. In addition, this tolerance accounts for big track slopes.

5.4 Cuts Applied in `fTrkSeeder`

The details and the purpose of cuts for the track finding algorithm `fTrkSeeder` are described in the previous chapter. The summary of the cuts is listed in Table 5.2. It should be noted, that `fTrkSeeder` does not require any special hit-level cuts except the ones which are described in Section 5.3.1.

5.4.1 Performance

The strategy of the analysis is to reduce the occupancies of the recorded events in order to guarantee a reasonable track reconstruction. `fTrkSeeder` was used

Block of Runs	Run	$N_{Triggers}$
A	2173	26235
	2171	30754
	2170	41038
	2169	34602
	2165	40956
	2164	30276
	2163	29838
	2162	30790
	2161	10461
	2160	32664
	2159	27118
	2158	26686
	2157	30246
	2156	30206
	2155	30177
	Total	$\mathbf{4.05 \times 10^5}$
B	2140	14020
	2138	15109
	2137	11799
	2136	10818
	2135	10961
	2134	1869
	2133	27128
	2132	11198
	2131	1991
	2130	1988
	2129	10003
	2128	10847
	2127	12246
	2126	15707
	2125	13502
	2124	15149
	2123	20397
	2122	22490
	2121	44649
	2120	4737
	2119	10948
	2118	10016
	2117	573
	2116	1288
	2115	14112
	2114	7102
	Total	$\mathbf{1.99 \times 10^5}$

Data Set	Run	$N_{Triggers}$
C	2109	14074
	2108	12901
	2107	13498
	2106	9802
	2105	15400
	2104	15952
	2103	15983
	2102	18967
	2101	16086
	2100	9709
	2099	20167
	2098	18864
	2097	26121
	2096	486
	2095	4224
	2094	1279
	2093	1325
	2092	5198
	2091	11653
	2090	13968
	2089	11687
	2088	10579
	2087	3303
	Total	$\mathbf{2.55 \times 10^5}$
D	2085	4102
	2083	15501
	2082	30860
	2081	25004
	2080	28922
	2079	30742
	2078	31139
	2077	23639
	2076	17439
	2075	11505
	2073	33384
	2072	10111
	2071	8071
	2070	33084
	2069	29289
	2068	38227
	2067	54682
	2065	12192
	2064	3386
	Total	$\mathbf{4.33 \times 10^5}$

Data Set	Run	$N_{Triggers}$
E	2052	2838
	2051	27558
	2050	16625
	2049	15850
	2048	13871
	2046	14728
	2045	13771
	2044	2860
	2043	20454
	2042	13267
	Total	$\mathbf{1.39 \times 10^5}$
A+B+C+D+E		$\mathbf{1.25 \times 10^6}$

Table 5.1: Summary of the data set used in this thesis.

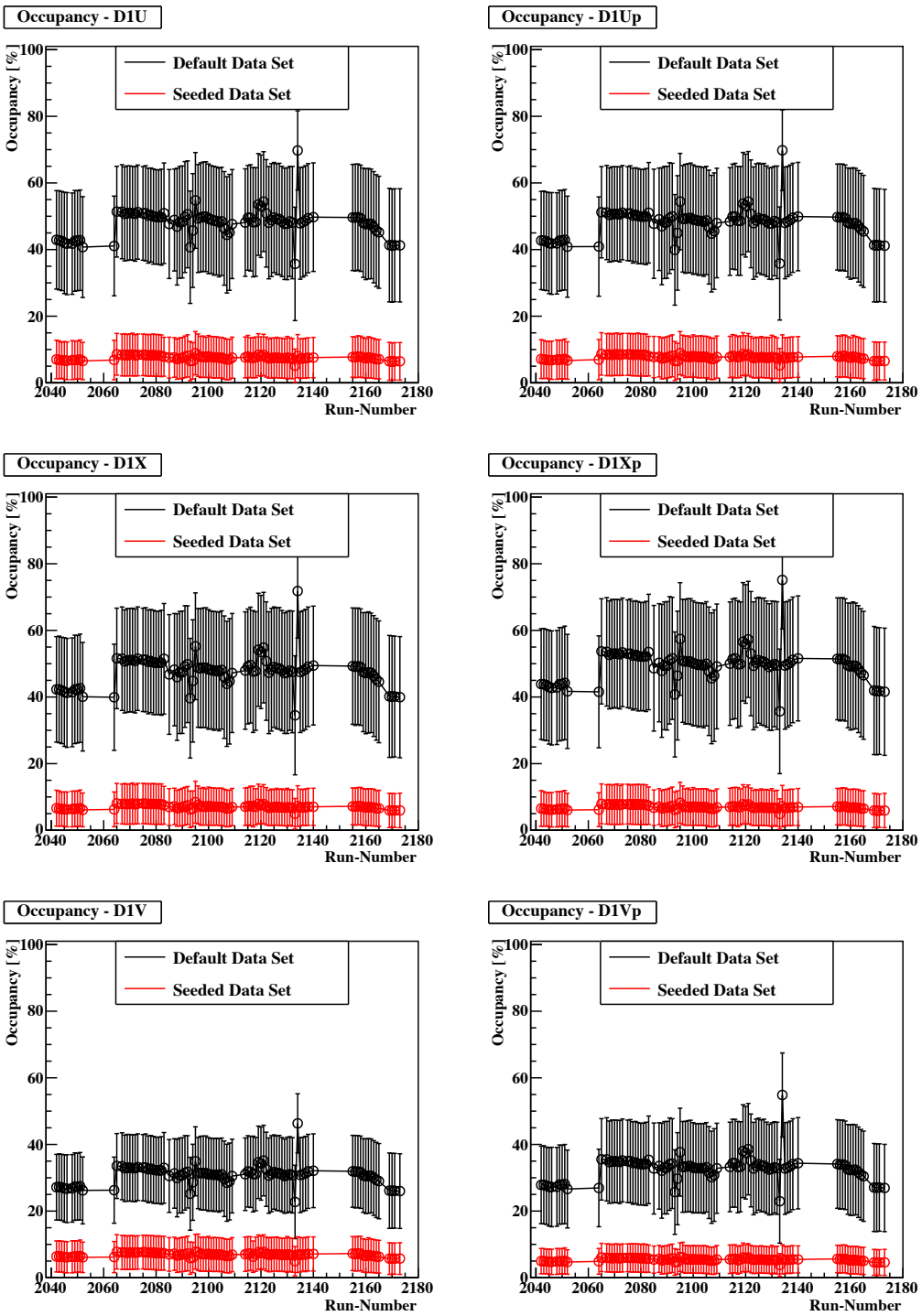

Figure 5.8: All layers of Station 1: Occupancy after `fTrkSeeder` has processed the raw-data set. Occupancy versus time during the commissioning run. The black line shows the average occupancy per event in the raw-sample, the red line represents the average occupancy per event in after `fTrkSeeder` was applied.

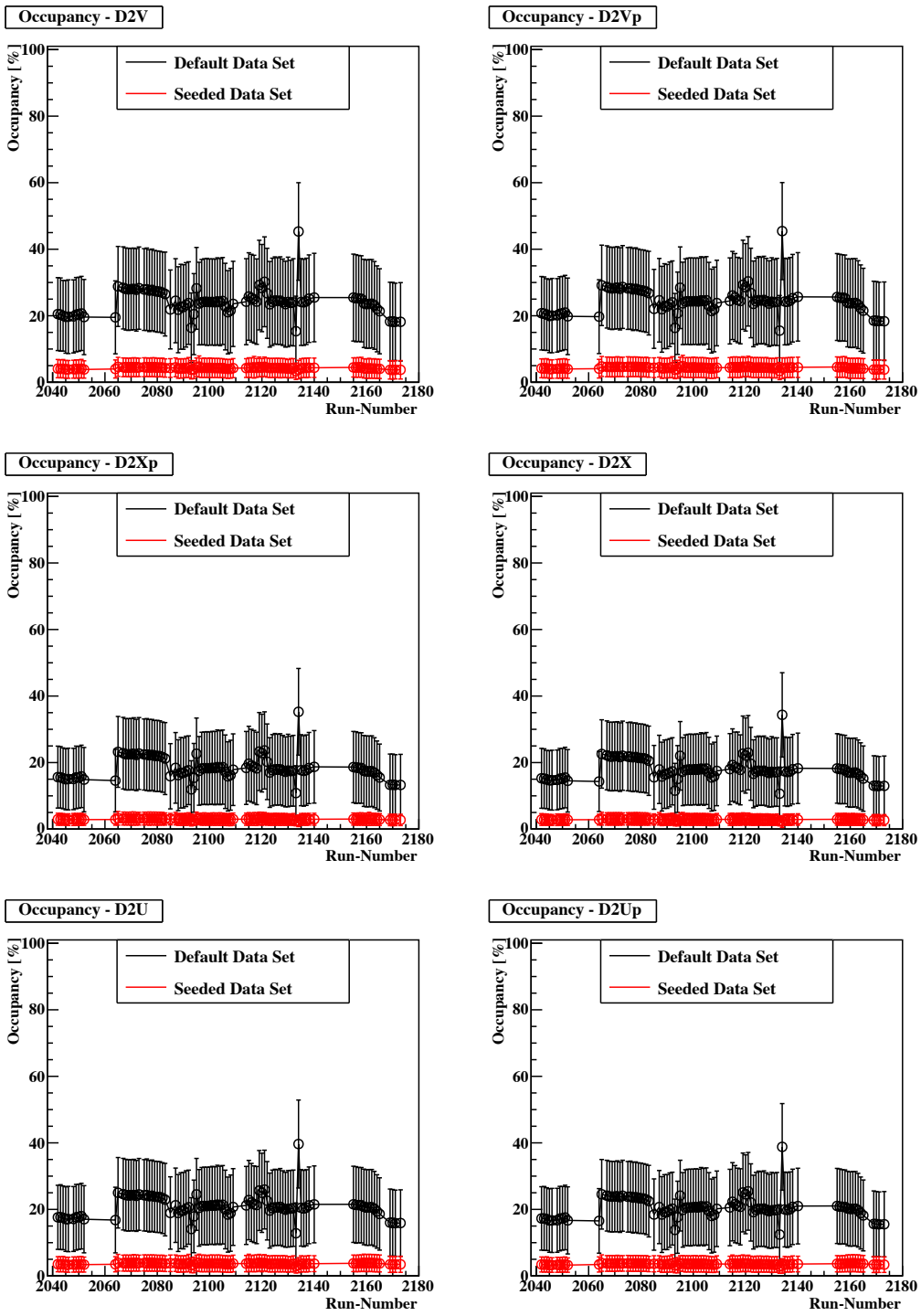

Figure 5.9: All layers of Station 2: Occupancy after fTrkSeeder has processed the raw-data set. Occupancy versus time during the commissioning run. The black line shows the average occupancy per event in the raw-sample, the red line represents the average occupancy per event in after fTrkSeeder was applied.

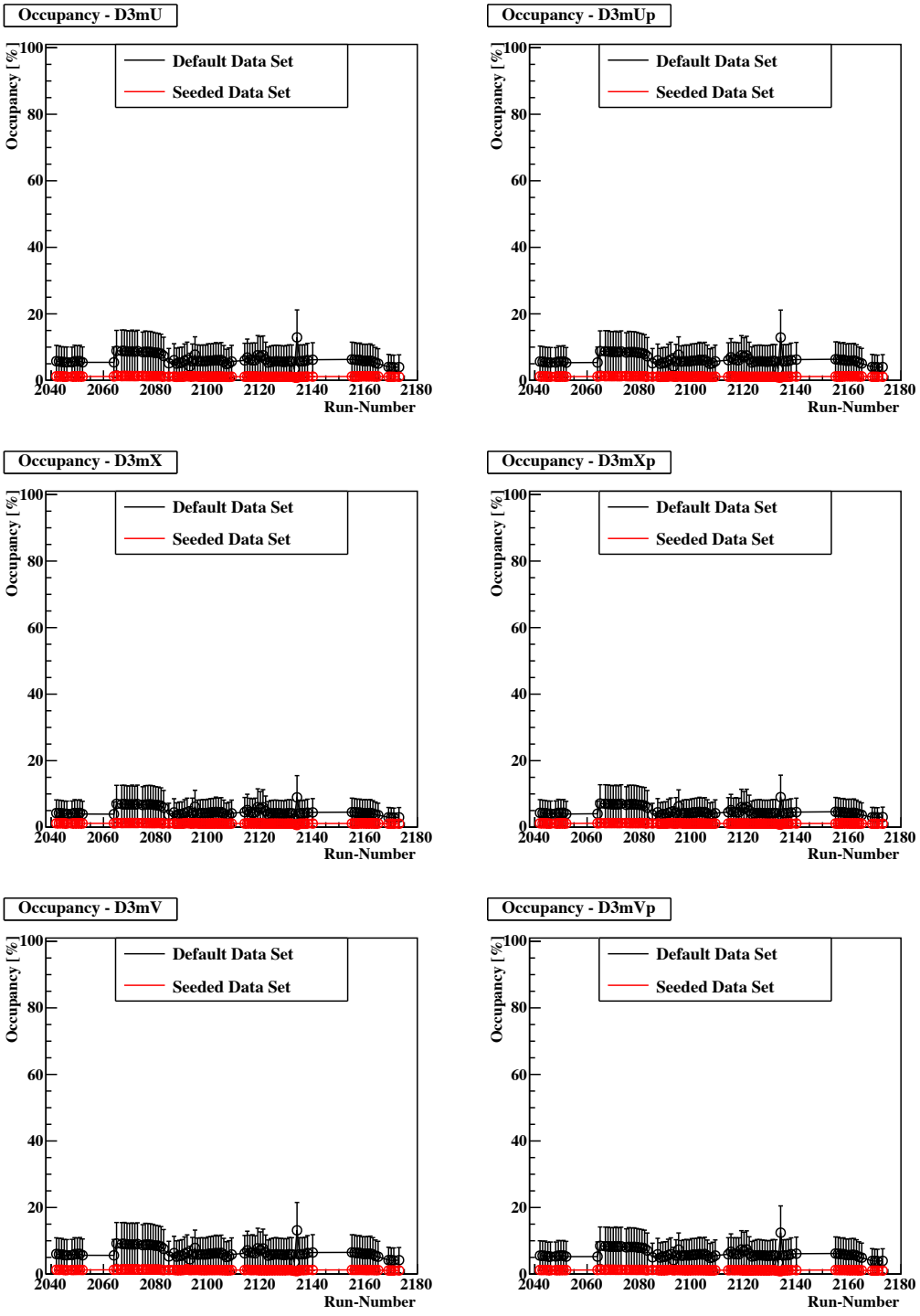

Figure 5.10: All layers of Station 3 Minus: Occupancy after `fTrkSeeder` has processed the raw-data set. Occupancy versus time during the commissioning run. The black line shows the average occupancy per event in the raw-sample, the red line represents the average occupancy per event in after `fTrkSeeder` was applied.

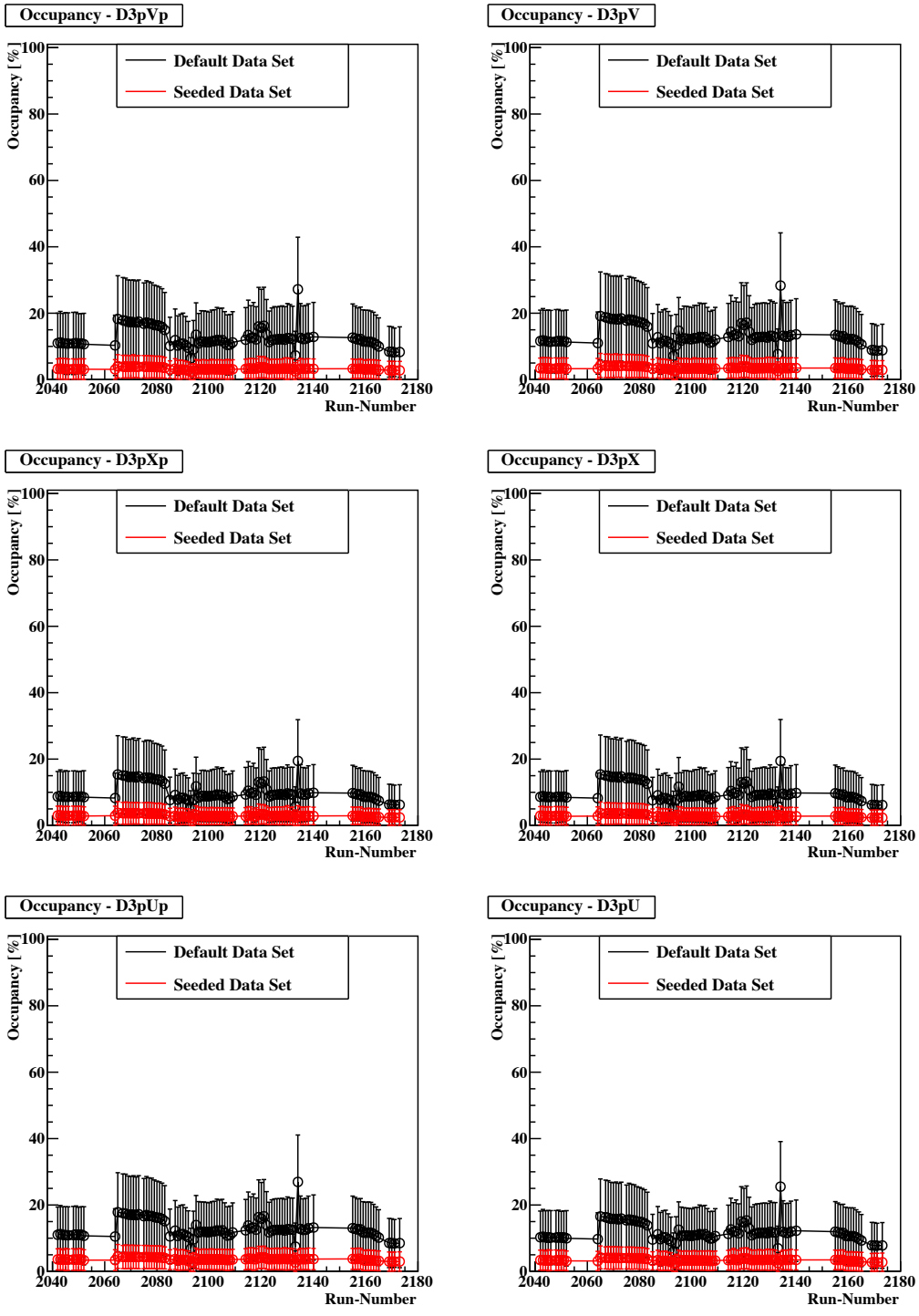

Figure 5.11: All layers of Station 3 Plus: Occupancy after fTrkSeeder has processed the raw-data set. Occupancy versus time during the commissioning run. The black line shows the average occupancy per event in the raw-sample, the red line represents the average occupancy per event in after fTrkSeeder was applied.

Cut Name	Cut Condition
Checksum Σ postive saggita	$\in [1.0, 2.5]$
Checksum Σ negative saggita	$\in [0.7, 2.0]$
Absolute value of 4-PT-St1 sagitta	$\lvert s_{\text{4-PT-St1}} \rvert \leq 50\,\text{cm}$
Absolute value of 4-PT-St2 sagitta	$\lvert s_{\text{4-PT-St2}} \rvert \leq 30\,\text{cm}$
Absolute value of 3-PT sagitta	$\lvert s_{\text{3-PT}} \rvert \leq 10\,\text{cm}$
Correlation tolerance	$3\,\sigma$
XUV tolerance	$1.5 \times$cell-size
Maximum number of positive triplets	4000
Maximum number of negative triplets	4000
Number of hits per track candidate	$15 \leq N_{\text{Candidate}} \leq 18$

Table 5.2: Summary of cuts of `fTrkSeeder` which are used in this analysis.

so that only raw hits which are associated to a track candidate are kept and stored. Events which either do not have a track candidate fulfilling the cuts or have too many candidates (see the maximum number of allowed triplets in Table 5.2) are discarded for the following track reconstruction. With this technique the occupancies in the drift chambers are reduced to average values of 5 % per event (see Figure 5.8 - 5.11). This is a dramatic improvement compared to the raw data. The comparison for each layer of all the drift chambers is shown in Figures 5.8 - 5.11.

In the following, a few characteristics of the performance of the algorithm are presented. First, it is important to know how effective the algorithm works in terms of removing non-physical hits. For this, the average hit-reduction per event was measured. The hit reduction r is defined as

$$r = 1 - \frac{N_{\text{after}}}{N_{\text{before}}}\,, \tag{5.4.1}$$

with N_{after} being the number of all the drift chamber hits after the the track finding step, and N_{before} being the number of all the drift chamber hits in the events as it was recorded. The reduction per event was measured as a function of the computation time (see top=panel in Figure 5.12). An average hit reduction of $\approx 80\,\%$ per event is reached by `fTrkSeeder`. This implies that a significant fraction of the recorded raw-hits are not correlated with a muon track.

Another important characteristic of `fTrkSeeder` is how the algorithm scales with the number of hits. Since the hit-combinations which need be checked by `fTrkSeeder` increase exponentially with the amount of hits, it would be natural that also the computation time has a similar scaling behavior. Figure 5.12 suggests such a exponential behavior. For future developments on the algorithm it is desir-

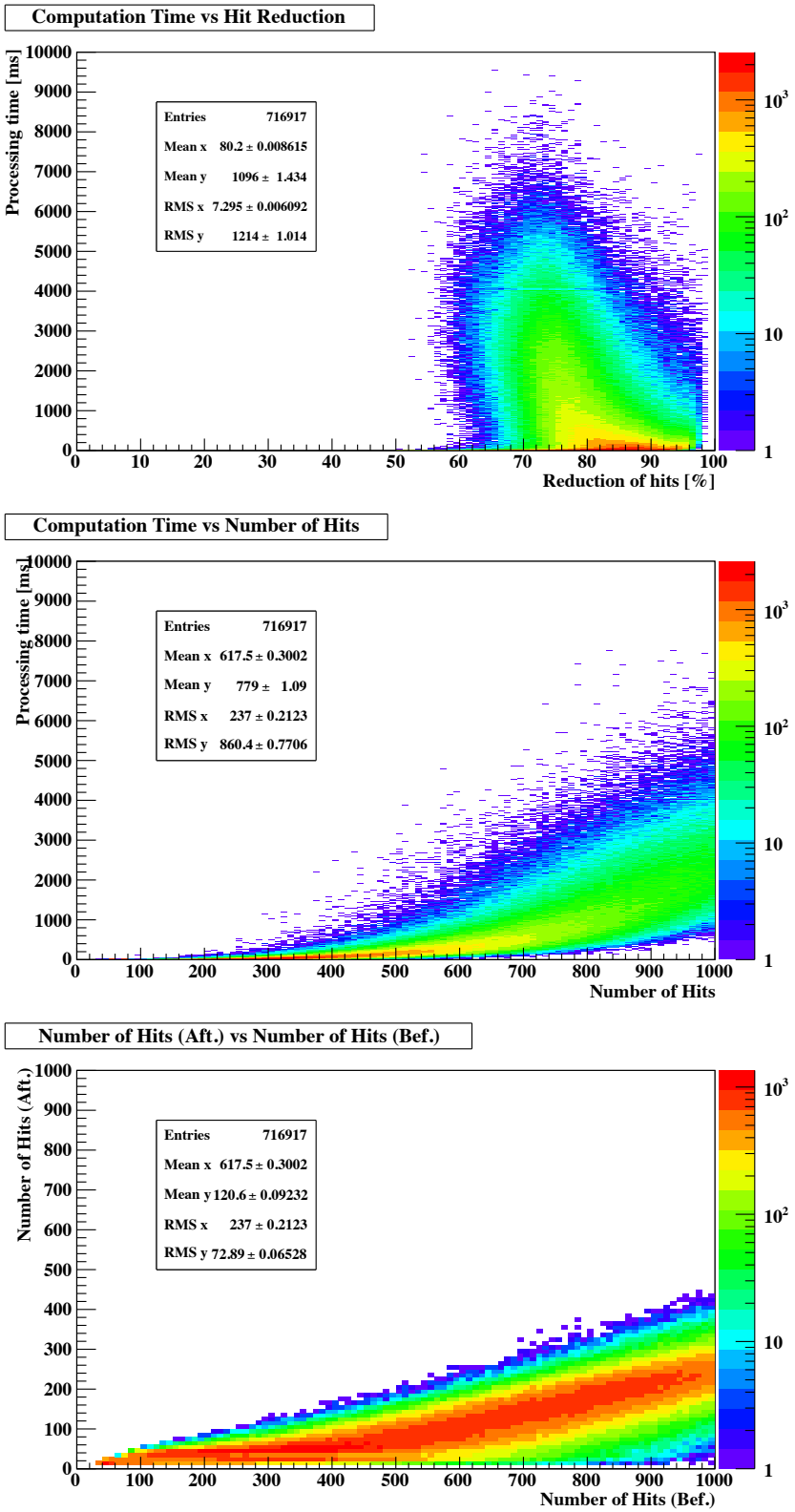

Figure 5.12: Summary of the performance measurements of fTrkSeeder. Top: Computation time as a function of hit reduction. Middle: Processing time as function of number of hits in the event. Bottom: number of drift chamber hits N_{after} as a function of N_{before}

able to design a more robust algorithmic behavior. The last measurment is the scatter plot N_{after} as a function of N_{before} (bottom panel in Figure 5.12). It is remarkable to note that for $N_{\text{before}} < 500$ the N_{aft} behaves very constant. This suggests a very strong hit-rejection power of the track finding algorithm. For values of N_{before} bigger than 500, N_{after} rises with a very small slope of $\approx 0.2 - 0.3$. All measurements in Figure 5.12 have been performed over the full data-set. The average processing time was 780 ms per event.

5.4.2 Event Yields

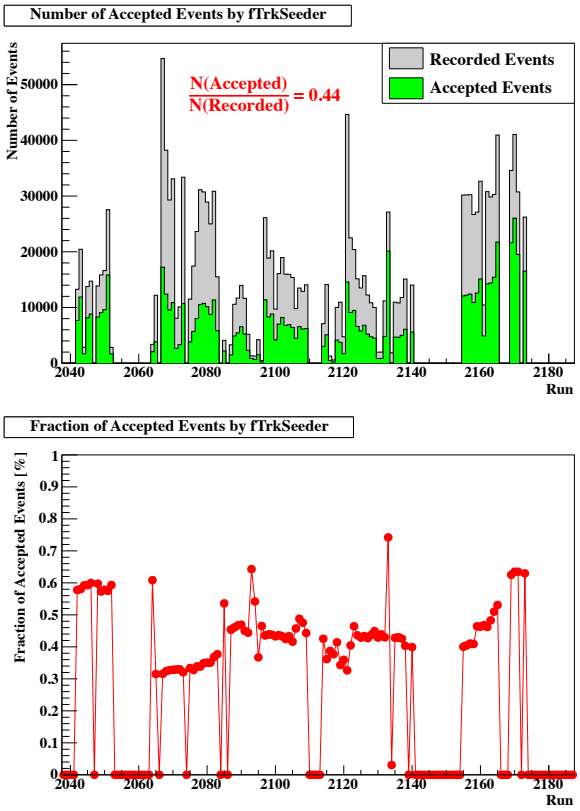

Figure 5.13: Top: Number of all recorded events (gray) and accepted events by `fTrkSeeder` (green). Altogether 44 % of all events are accepted by the track finding algorithm. Bottom: Fraction of accepted events for each run.

`fTrkSeeder` only accepted a raw event if at least one track candidate was identified by `fTrkSeeder` based on the cuts described in 5.2. An event was rejected either if there were to many triplet combinations in one event or if there were not enough hits to form a track candidate. The fraction of events which were considered as reconstructible was 44 % of the total dimuon data set, see Figure 5.13.

5.5 Cuts Applied in sqerp

5.5.1 Hit-Level Cuts

The track reconstruction program sqerp requires very well defined cuts on the hit level. In order to limit the combinatorial space for the track fitting procedure, one has to specify the cut windows for total amount hits per event and per tracking station very carefully. For the present analysis, the following two cuts are used which are listed in Table 5.3.

	Number of hits in		
Cut Name	Station 1	Station2	Station3
Cut1	$10 \leq N_{\text{Station1}} \leq 100$	$10 \leq N_{\text{Station2}} \leq 100$	$10 \leq N_{\text{Station3}} \leq 100$
Cut2	$10 \leq N_{\text{Station1}} \leq 60$	$10 \leq N_{\text{Station2}} \leq 30$	$10 \leq N_{\text{Station3}} \leq 30$

Table 5.3: Summary of the two cuts used in sqerp in this analysis.

The choice of the cut affects the selection of events which are processed by squerp tremendously. As reported in the beginning of this chapter, a significant fraction of recorded events have very high multiplicities. Thus, the amount of events which match either Cut1 or Cut2 on the raw event sample is rather low. However, for the hit-reduced data sample created by fTrkSeeder, the fraction of events which satisfy the corresponding cut windows increased significantly, as is shown in Table 5.4. For the complete data set, the increase of events which match the Cut1 range increased by 1518 % and for events which match the Cut2 range increased by 2253 %.

	Default data set		Seed data set		Increase	
Block of Runs	Cut1	Cut2	Cut1	Cut2	Cut1	Cut2
A	10258	3619	137297	73734	1337%	2036%
B	5779	2062	80576	40500	1393%	1963%
C	4572	1623	67920	33699	1485%	2075%
D	2301	599	81553	32771	3543%	5470%
E	2700	739	46909	22710	1736.%	3072%
Total	25610	8642	414255	203414	1518%	2253%

Table 5.4: Summary of the amount of event in each block of runs for the two hit-level cuts Cut1 and Cut2. The increase of events for each cut window in the seeded data sample compared to the raw data sample is shown in the last two columns.

In the following Cut1 is used for the track reconstruction for the default data set, and Cut2 for the track reconstruction for the seeded data set. The cuts are motivated

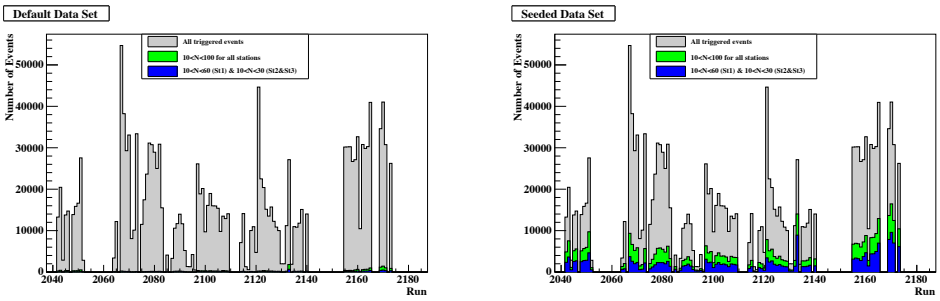

Figure 5.14: Left: Number of events which match Cut1 (green) and Cut2 (blue) for the default data set (left) and hit-reduced data set by `fTrkSeeder` (right).

by the computation time which is required by `sqerp` to process the complete data set. Figure 5.14 summarizes the event yields for both data sets.

5.5.2 Track Level Cuts

The cuts applied to successfully reconstructed muon tracks are listed in Table 5.5.

Cut Name	Cut Condition
χ^2/NDF	$\chi^2 \leq 4.$
P_z	$P_z \geq 10\,\text{GeV}$

Table 5.5: Summary of cuts of `sqerp` which are used in this analysis.

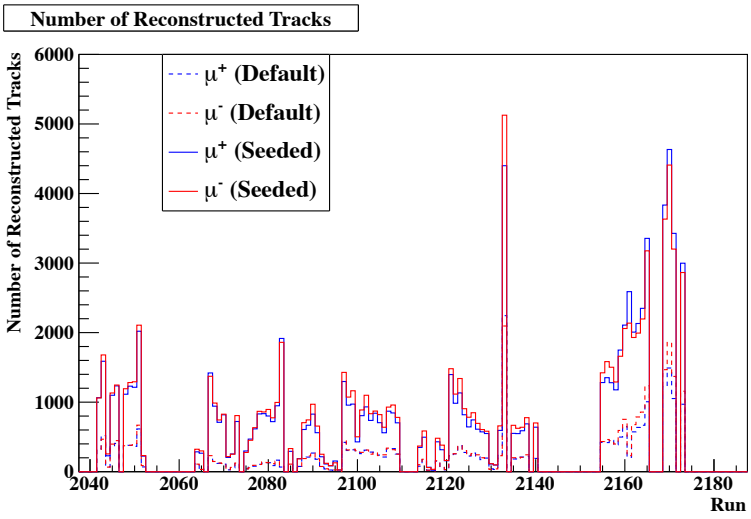

Figure 5.15: Illustration of the number of reconstructed muon tracks. The yields of the default data set are shown in dashed lines, the yield of the seeded data set in solid lines.

The motivation for the χ^2-Cut is mainly to reject tracks which take too many

Block of Runs	Default data set		Seed data set		Increase	
	μ^+	μ^-	μ^+	μ^-	μ^+	μ^-
A	10653	12729	36271	35053	339%	274%
B	6274	6311	17508	19837	278%	313%
C	4928	4988	14096	15863	285%	317%
D	1896	2000	13351	13777	703%	688%
E	3168	3293	9952	10420	313%	315%
Total	26919	29321	91178	94950	239%	224%

Table 5.6: Summary of the amount of reconstructed muon tracks for the default and seeded data set. The increase by the seeded data set is listed in the last column for each particle type.

fake hits into account. Fake hits give rise to high values of χ^2. A χ^2 of 4 accounts for small in-efficiencies in the drift chambers, detector misalignment and uncertainties in the drift-time calibrations. The Cut on z-component of the reconstructed momentum P_z is motivated by the vertex determination in which the track is accounted for energy loss in the FMAG iron. The yields of reconstructed tracks fulfilling the cut criteria is summarized in Table 5.6, and visualized in Figure 5.15. `fTrkSeeder` increased the the yield of μ^+-tracks could be increased by a factor of 3.39 and the yield off μ^--tracks by a factor 3.24. The resulting momentum distributions for both data sets are shown in Figure 5.16. The normalized track multiplicities, i.e. the number of tracks per event are shown in Figure 5.17. `fTrkSeeder` increases the relative fraction of events with more than 1 track compared to the default case.

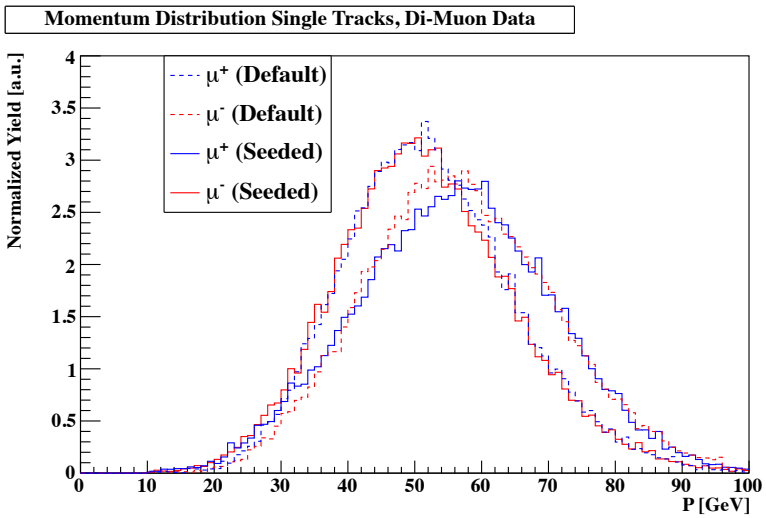

Figure 5.16: Normalized momentum distributions of reconstructed muon tracks. Seeded data set in dashed lines, default data set in solid lines.

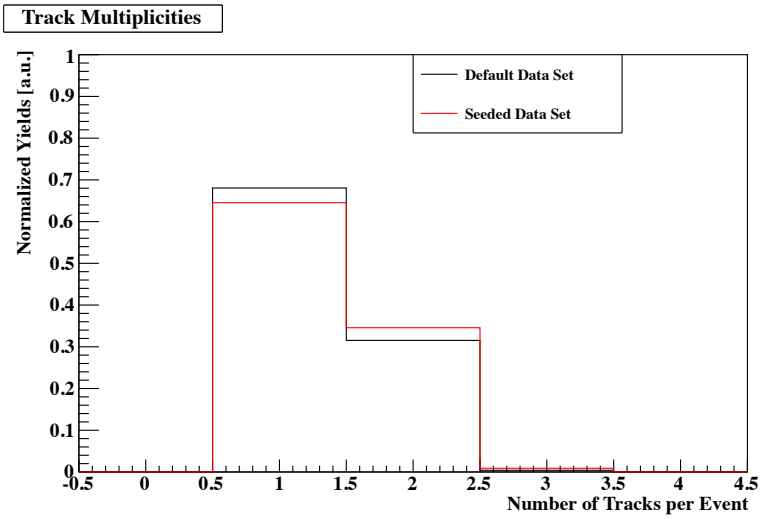

Figure 5.17: The Track Multiplicites in the default data set and the seeded data set. The red line suggests that `fTrkSeeder` increases the relative fraction of events with more than 1 track compared to the default case.

5.5.3 Dimuon Cuts

A dimuon pair is constructed by combining a positively and a negatively charged muon track in one event. The requirements to classify a two single tracks as a dimuon is listed in Table 5.7.

Cut Name	Cut Condition
χ^2/NDF for μ^+	$\chi^2 \leq 4.$
χ^2/NDF for μ^+	$\chi^2 \leq 4.$
$\Delta z_{\text{Vertex}} = \lvert z_{\text{Vertex}}(\mu^+) - z_{\text{Vertex}}(\mu^-)\rvert$	$\Delta z_{\text{Vertex}} \leq 100\,\text{cm}$

Table 5.7: Summary of dimuon cuts of `sqerp` which are used in this analysis.

The z-vertex cut is inspired by the length of the target flasks which are 50.8 cm long. `sqerp` was optimized to provide a resolution so that the vertex of a dimuon arising from the target can be resolved. Thus, the maximum distance between the vertex twice the target length.

The yields of reconstructed dimuons fulfilling the cut criteria are summarized in Table 5.8. `fTrkSeeder` increased the the yield of dimuon-tracks by a factor of 3.25. The Δz-distribution is shown in Figure 5.19. Both for the seeded and for the default data set, it is fairly flat. The two dimensional scatter plots in Figures 5.20 and 5.21 show the $\chi^2_{\mu^+}$-vs-$\chi^2_{\mu^-}$ for the seeded and dfault data set. By applying the cut $\chi^2 \leq 4.$, one selects exactly the region of the scatter plots where most events are accumulated.

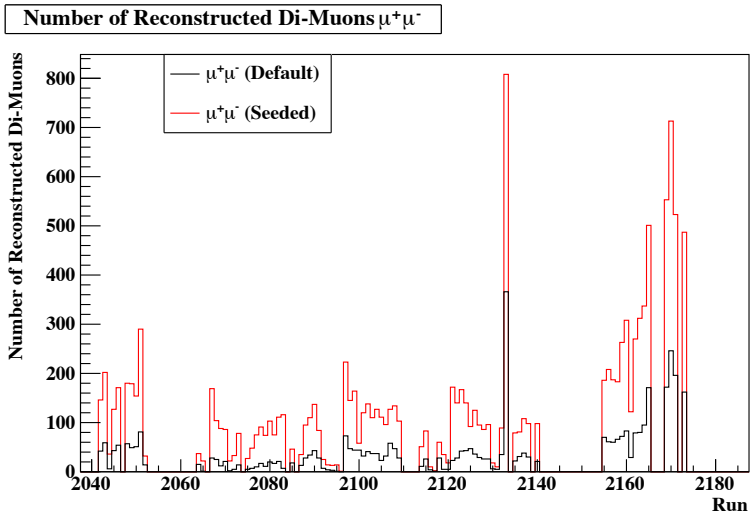

Figure 5.18: Illustration of the number of reconstructed dimuons. The yields of the default data set are shown in dashed lines, the yield of the seeded data set in solid lines.

Block of Runs	Default data set $\mu^+\mu^-$	Seed data set $\mu^+\mu^-$	Increase
A	1642	5201	313 %
B	934	2791	295 %
C	705	2224	309 %
D	257	1422	548 %
E	414	1377	1371 %
Total	3952	13020	225 %

Table 5.8: Summary of reconstructed dimuons for the default and seeded data set. The increase of dimuons by the seeded data set is listed in the last column.

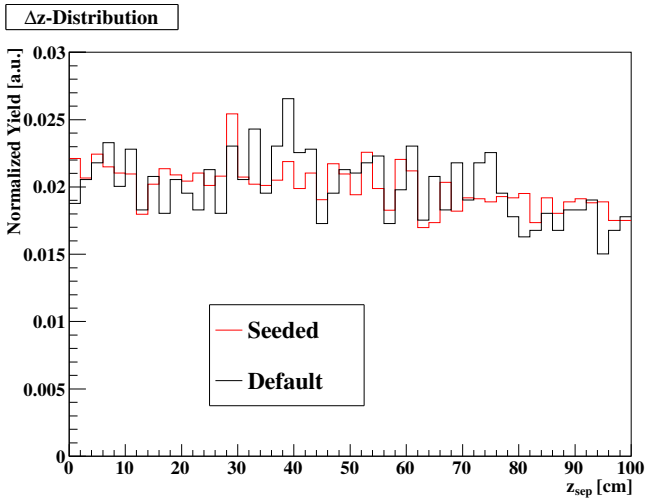

Figure 5.19: Δz-distributions for the default (black line) and seeded (red line) data set.

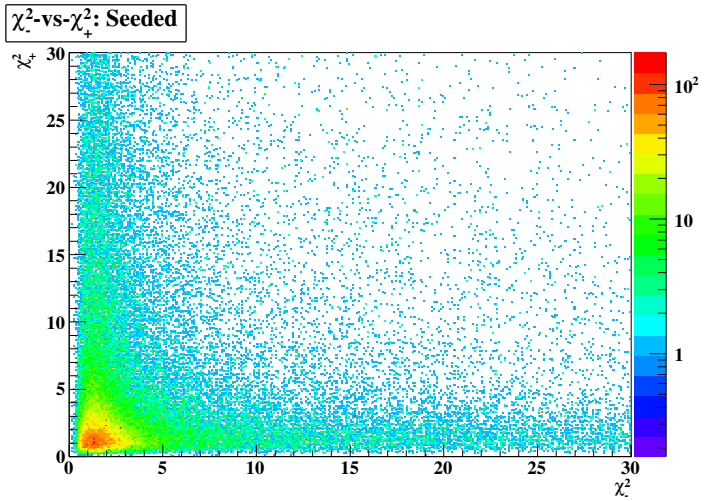

Figure 5.20: $\chi^2_{\mu^+}$-vs-$\chi^2_{\mu^-}$-scatter plot for the seeded data set. The cut $\chi^2 \leq 4.$ selects the region where most events accumulate.

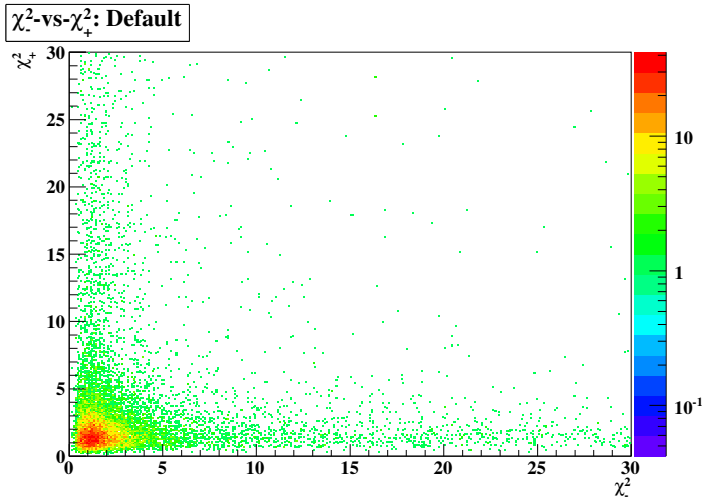

Figure 5.21: $\chi^2_{\mu^+}$-vs-$\chi^2_{\mu^-}$-scatter plot for the default data set. The cut $\chi^2 \leq 4.$ selects the region where most events accumulate.

Chapter 6

Results and Discussion

6.1 The Reconstructed Dimuon Mass Spectra

The most important result of the commissioning run of the SeaQuest spectrometer in 2012 is the invariant mass spectrum of the reconstructed dimuons from proton-proton collisions at a beam energy of 120 GeV. The invariant dimuon mass spectrum can be see in Figure 6.1. The error bars represent statistical uncertainties.

The yield of dimuon in the low-mass region between 0.2 and 1 GeV/c^2 rises very steeply. The spectrum reaches its first peak at mass values $M_{\mu^+\mu^-} \approx 1\,\text{GeV/c}^2$. For values between 1 and 2.4 GeV/c^2 the spectrum falls similarly steeply as it was rising in the low-mass region. The peak at ≈ 1 Gev/c^2 has a rather symmetric shape. This part could be combinatorial background. combinatorial background is defined as two opposite-sign muons which were produced independently by pion decay or other processes, coincidentally fired the dimuon trigger system. Based on the dimuon cuts presented in the previous chapter it appears to be a valid dimuon event. Detailed studies on the background are presented in the later sections.

In the region between 2.4 Gev/c^2 and 3.1 Gev/c^2 a second peak is observed. This peak can be associated with the J/ψ particle. The main decay channel of the J/ψ meson is the dimuon decay channel with a branching ratio of 5.97 % [72].

For the mass region above 4 Gev/c^2, the following observations can be made. With the SeaQuest default method of track reconstruction (black line in Figure 6.1) the yield in this region seems to be pretty low. However, with the improved method, which combines my track finder `fTrkSeeder` with the track fitter `sqerp`, the fraction of muon pairs could be increased compared to the the low-mass muon pairs. This behavior can be observed in Figure 6.2. It shows the ratio of the invariant mass spectrum obtained by the improved method over the mass spectrum obtained by the

default method. The improvement in yield per bin is rather constant $\approx 200\%$ for mass values below $3\,\mathrm{GeV/c^2}$. For mass values above $3\,\mathrm{GeV/c^2}$, the ratio increases constantly.

It is difficult to compare the shape of the re-constructed invariant mass spectrum spectrum with expectations from e.g. Monte Carlo. On one hand, this can be attributed to the unexpected beam problems during the commissioning run. On the other hand, the dimuon trigger setting which was used during Run1 did not have any level-2 trigger cut. The level-2-trigger at SeaQuest is responsible to estimate the average p_T of a muon track which is matching the trigger road criteria. There was no cut implemented in trigger setup for the commissioning run. Thus it is not suited to measure Drell-Yan events. In order to judge on the performance on the SeaQuest spectrometer, it is important to have a detailed look at the J/ψ peak region. It is possible to make use of J/ψ to judge the performance of the SeaQuest spectrometer, and of the reconstruction software at the same time. In the following section a detailed study of the J/ψ-peak is presented.

Figure 6.4 (6.3) shows the two-dimensional distribution of invariant mass versus z-vertex for the default (seeded) data set. The shape of the scatter plots is rather similar. Most of the re-constructed dimuons originate from the inside the FMAG iron with vertex values of $z \geq 0\,\mathrm{cm}$. No significant dependence of the invariant mass is observed. For detailed studies it is necessary to identify the underlying physics in more detail. For this purpose, we introduce background models in the following sections. They allow us to isolate the J/ψ signal from background. Pure J/ψ observables are well suited for comparisons with Monte Carlo predictions.

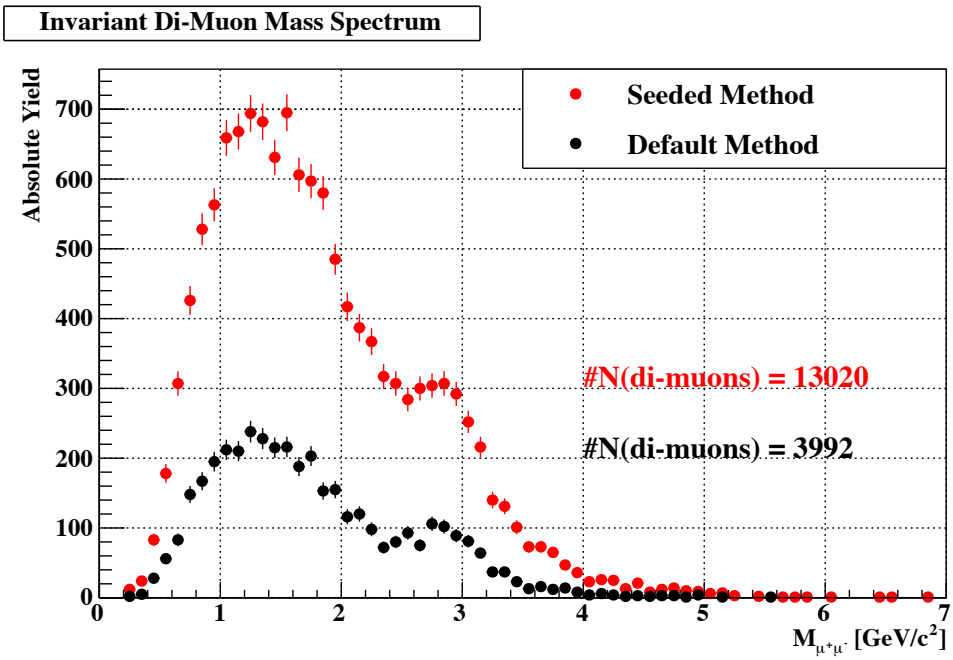

Figure 6.1: Invariant mass spectrum based on the commissioning run of the SeaQuest spectrometer. The black line shows the spectrum obtained from the deault data sample, the red line shows the result obtained from the seeded sample.

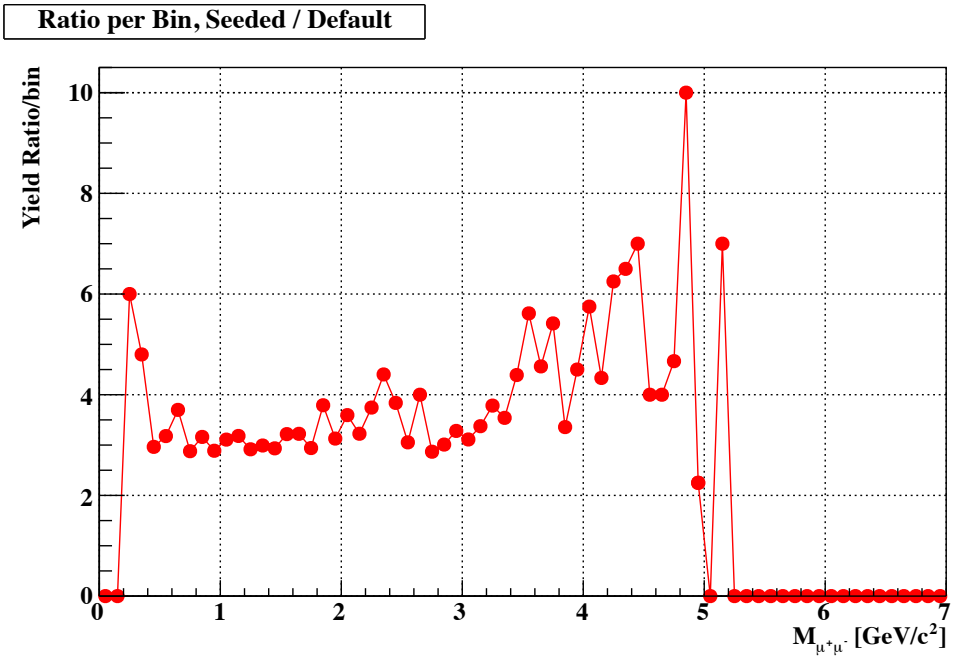

Figure 6.2: Ratio of the invariant mass spectrum obtained with the default data set over the mass spectrum obtained from the seeded data set. The seeded data set particularly increased the ratio of dimuons in the mass range above 3 GeV/c^2.

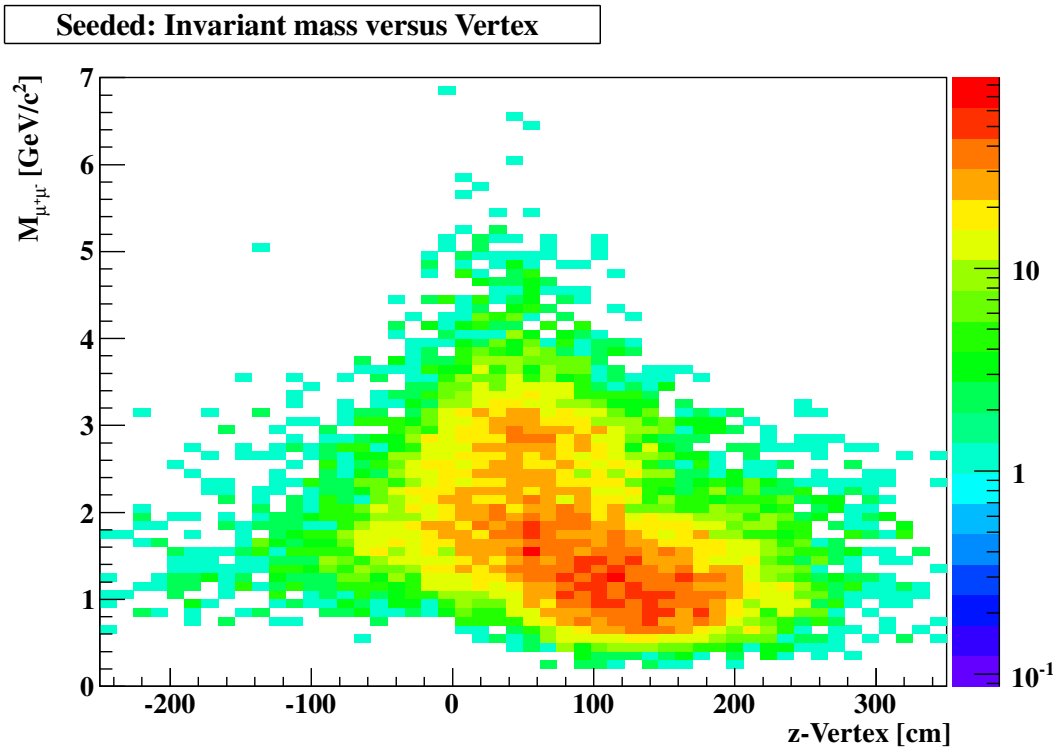

Figure 6.3: Two-dimensional distribution of invariant mass versus z-vertex for the seeded data set.

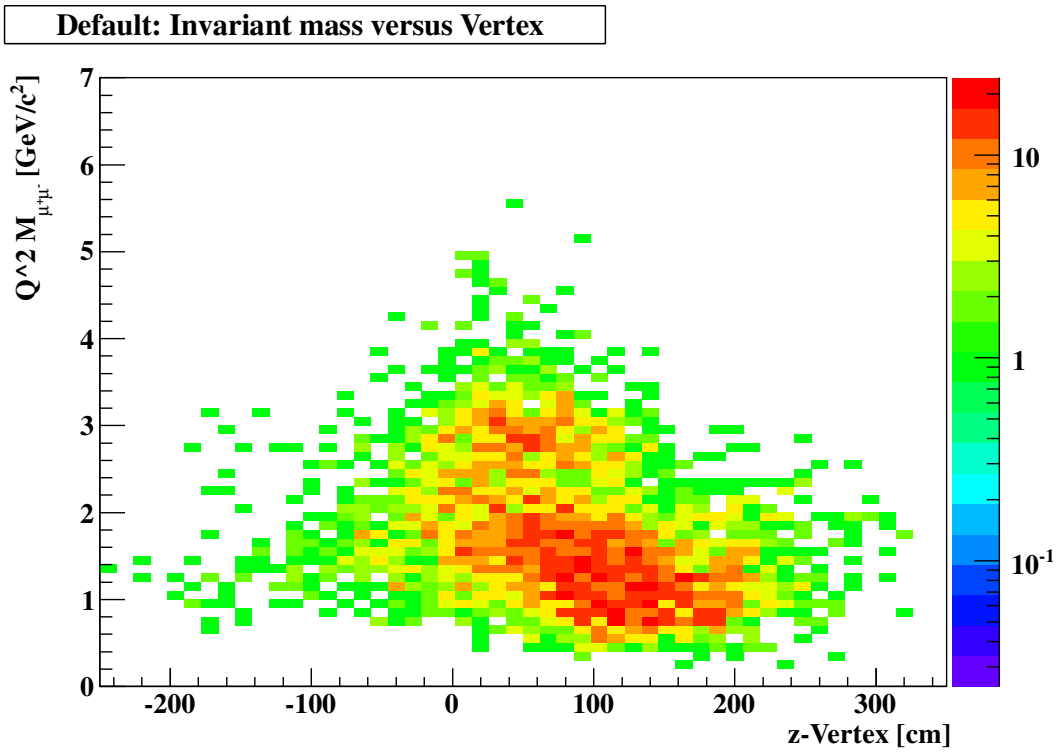

Figure 6.4: Two-dimensional distribution of invariant mass versus z-vertex for the default data set.

6.2 J/ψ Yields, Mass and Width

In order to have an estimate of the shape and position of the J/ψ-peak, it is necessary to have a reasonable background model. For the studies on the J/ψ, it is sufficient to obtain a model for the mass region above $1\,\mathrm{GeV/c^2}$. In the following analysis two models for the background estimation are used. The first one is a model obtained by a polynomial model. The second model is based on a combinatorial background model. This model is randomly mixing single muon tracks from different events and combines them to one fake dimuon.

6.2.1 Background Model I: 4th-order Polynomial

The polynomial background model applied in this analysis was a fourth order polynomial fit.

$$f_{\mathrm{Background}}(x) = c_0 + c_1 \cdot x + c_2 \cdot x^2 + c_3 \cdot x^3 + c_4 \cdot x^4 \,. \tag{6.2.1}$$

The fit was performed in the mass range of (see Figure 6.5 and 6.7)

$$[1.4\,\mathrm{GeV/c^2}, 5.5\,\mathrm{GeV/c^2}]. \tag{6.2.2}$$

In order obtain an estimate on the background in the J/ψ mass region, the mass range of

$$[2.4\,\mathrm{GeV/c^2}, 3.5\,\mathrm{GeV/c^2}] \tag{6.2.3}$$

was skipped. The obtained fit function was extrapolated into the J/ψ-region and subtracted from the mass spectrum. By this, one obtains a mass spectrum corrected for the background (see Figures 6.6 and 6.8).

For the estimation of the reconstructed J/ψ-mass, a single Gaussian fit was performed in the region given in Eq. (6.2.3). The obtained J/ψ-mass values are (c.f. Figures 6.6 and 6.8)

$$\text{Default Sample}: \quad M(J/\psi) = (2.919 \pm 0.023)\,\mathrm{GeV/c^2} \tag{6.2.4}$$

$$\text{Seeded Sample}: \quad M(J/\psi) = (2.938 \pm 0.020)\,\mathrm{GeV/c^2}\,. \tag{6.2.5}$$

For the the reconstructed J/ψ-width, the following results were obtained (c.f.

Figures 6.6 and 6.8)

$$\text{Default Sample}: \quad \sigma(J/\psi) = (0.218 \pm 0.021)\,\text{GeV/c}^2 \tag{6.2.6}$$

$$\text{Seeded Sample}: \quad \sigma(J/\psi) = (0.205 \pm 0.019)\,\text{GeV/c}^2\,. \tag{6.2.7}$$

The mass values both for the default data sample, as well as for the seeded data sample are below the PDG value of $M(J/\psi) = (3.097 \pm 0.011)\,\text{GeV/c}^2$. This suggests that there must be a small offset in the SeaQuest spectrometer causing that difference. Future studies have to revisit the momentum kick by both dipole magnets FMAG and KMAG, and the energy loss parameterizations in the FMAG iron. The width values both for the default data sample, as well as for the seeded data sample are above the PDG value of $\sigma(J/\psi) = (0.093 \pm 0.003)\,\text{GeV/c}^2$.The resolution improved slightly with the seeded data sample compared to the default sample.

The yield of J/ψ's was obtained by a numerical integration of the background corrected mass spectrum. The integration range was set to

$$[2.7\,\text{GeV/c}^2, 3.2\,\text{GeV/c}^2]\,. \tag{6.2.8}$$

Taking the error in the numerical integration into account, the following J/ψ-yields were obtained for the default data sample, and the seeded data sample respectively

$$\text{Default Sample}: \quad N(J/\psi) = 253.46 \pm 21.89 \tag{6.2.9}$$

$$\text{Seeded Sample}: \quad N(J/\psi) = 602.21 \pm 48.99\,. \tag{6.2.10}$$

The yield of J/ψs, when `fTrkSeeder` was used, increased by a factor of 2.4 compared to the default method (the factor is defined as $N_{\text{Seeded}}(J/\psi)/N_{\text{Default}}(J/\psi)$).

By taking the ration of the amount of background events (defined by the 4th-order polynomial, to the number of J/Ψs, it is possible to define the Singal-to-Noise Ratio (*SNR*). The number of background events was evaluated in the kinematic range given in Eq. (6.2.8). The obtained *SNR*s for the default and the seeded data sample are as follows

$$\text{Default Sample}: \quad SNR = 1.12 \pm 0.16 \tag{6.2.11}$$

$$\text{Seeded Sample}: \quad SNR = 0.33 \pm 0.09\,. \tag{6.2.12}$$

The *SNR* has decreased in the seeded sample compared to the default sample. For Run1, `fTrkSeeder` improved the absolute yield on dimuons, not the *SNR*.

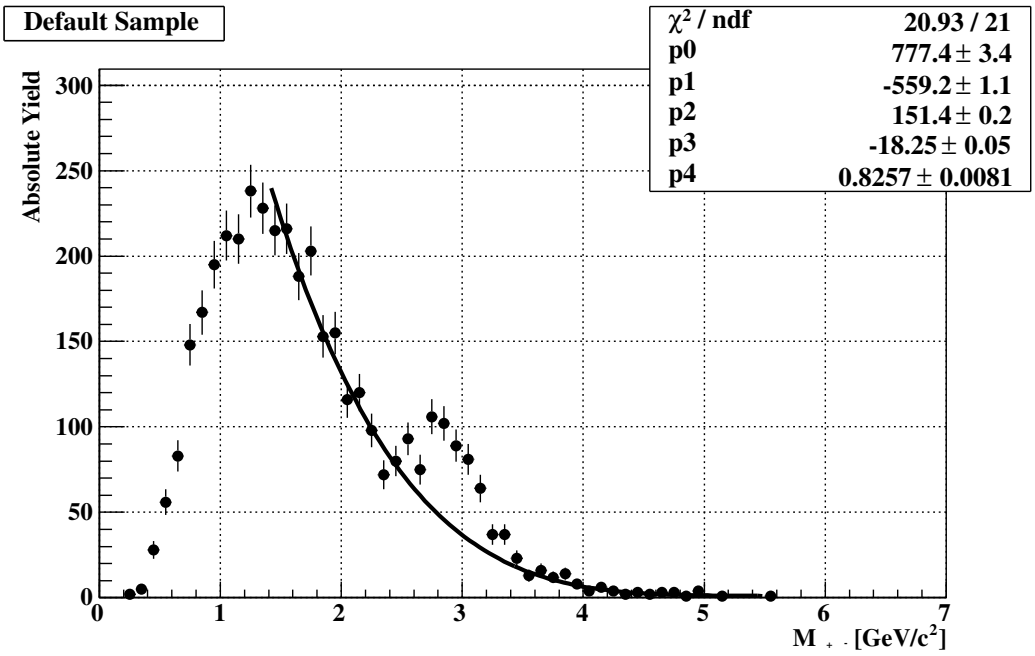

Figure 6.5: Invariant mass spectrum obtained with the default sample. The solid black line shows the 4-th order polynomial background estimation.

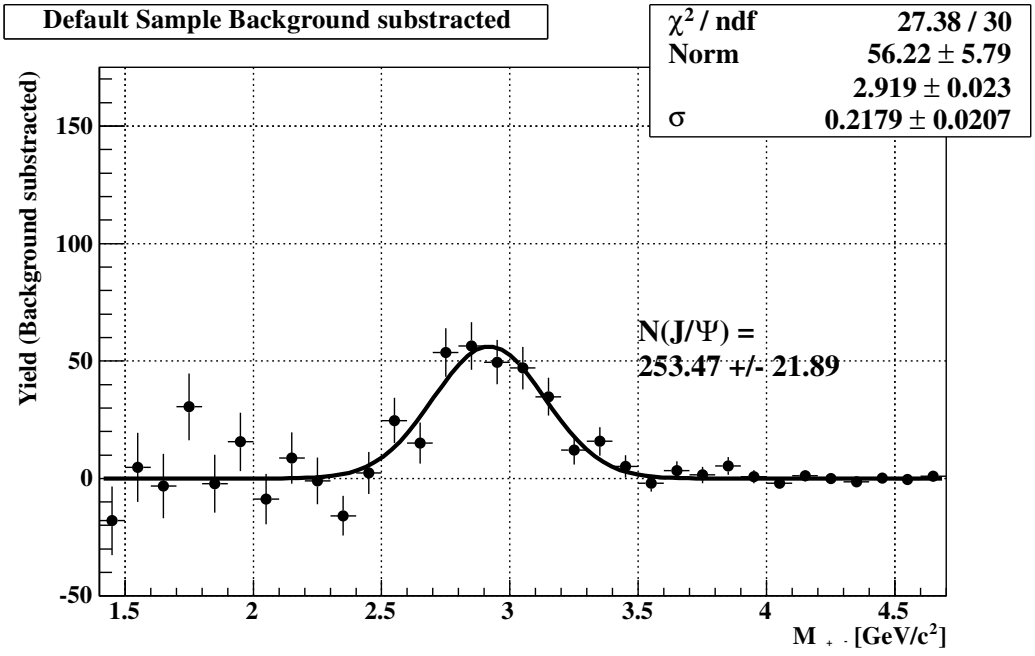

Figure 6.6: Invariant mass spectrum for the default sample corrected for the background. The J/ψ-mass is estimated with a single Gaussian. The number of reconstructed J/ψ's is estimated via a numerical integration in the range $[2.7\,\mathrm{GeV/c^2}, 3.2\,\mathrm{GeV/c^2}]$.

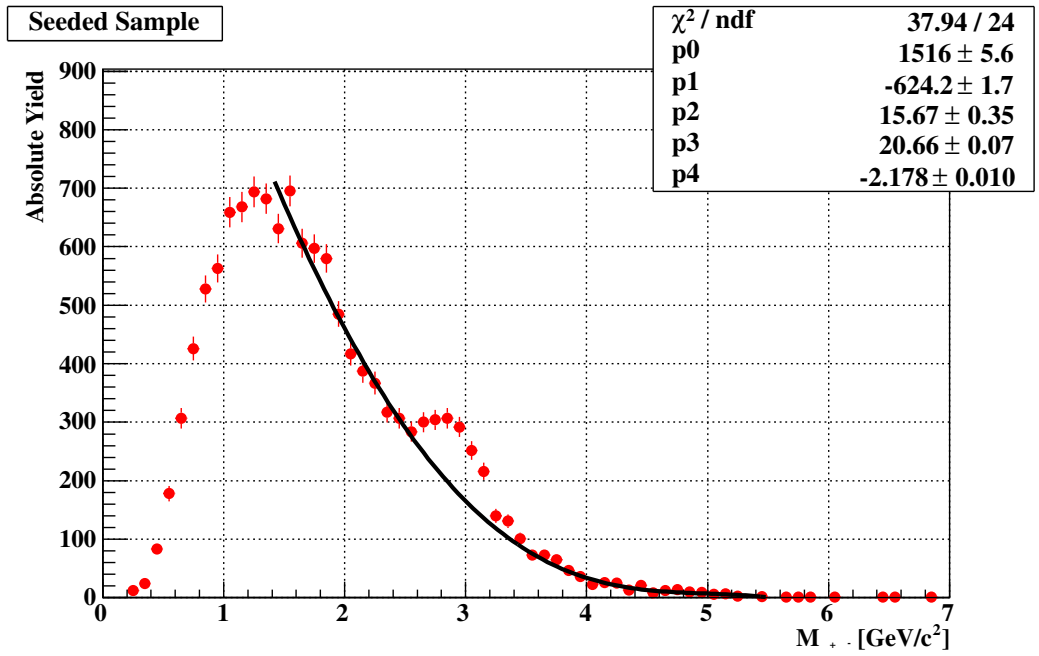

Figure 6.7: Invariant mass spectrum obtained with the seeded sample. The solid black line shows the 4-th order polynomial background estimation.

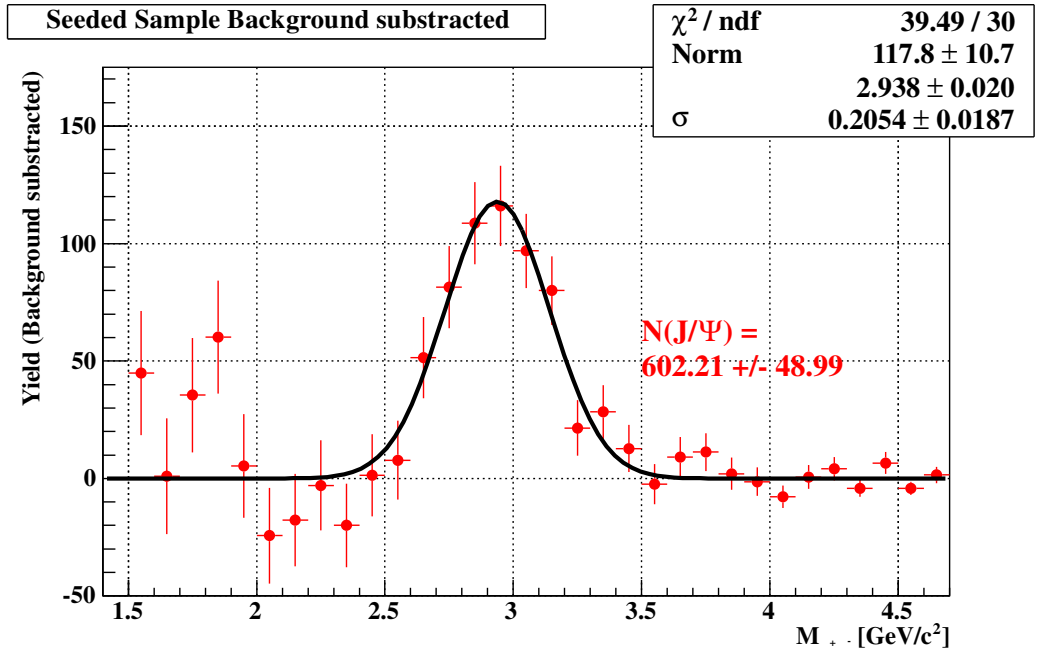

Figure 6.8: Invariant mass spectrum for the seeded sample corrected for the background. The J/ψ-mass is estimated with a single Gaussian. The number of reconstructed J/ψ's is estimated via a numerical integration in the range $[2.7\,\mathrm{GeV/c^2}, 3.2\,\mathrm{GeV/c^2}]$.

6.2.2 Background Model II: Event Mixing

Random muon pairs are the most significant background at SeaQuest, particularly in the mass regions up to the J/ψ mass. The definition of a random pair is that two opposite sign muons which were produced independently by pion decay or other processes, coincidentally fired the trigger system and appeared to be a valid dimuon event. The random pair distributions could not be measured directly, because the pairs were indistinguishable from the 'real' dimuons in the spectrometer; they were however obtained from randomly mixing single muon track with opposite charges from different recorded events. The mixing requirements were the same as for the dimuon reconstruction within one event (c.f. Section 5.5.3). Altogether 10k combinatorial dimuons were generated out of the $\approx$ 91k positve and $\approx$ 95k negative muon tracks (cf. Section 5.5.2).

This combinatorial background model was subtracted from the reconstructed seeded mass spectrum in order to correct for background contamination. By this, an alternative method to the 4th-order polynomial fit for the extraction of the J/ψ mass, width and yield is introduced. Before the subtraction was performed, the combinatorial background mass spectrum was matched to the reconstructed mass spectrum in a way that the number of dimuons in the mass range

$$[1.9\,\mathrm{GeV/c^2}, 2.4\,\mathrm{GeV/c^2}] \tag{6.2.13}$$

was matched (cf. Figure 6.9).

The extracted values for the J/ψ mass, width, yield and *SNR* are as follows

$$M(J/\psi) = (2.972 \pm 0.038)\,\mathrm{GeV/c^2} \tag{6.2.14}$$
$$\sigma(J/\psi) = (0.336 \pm 0.056)\,\mathrm{GeV/c^2} \tag{6.2.15}$$
$$N(J/\psi) = 655 \pm 59.90 \tag{6.2.16}$$
$$SNR = 0.47 \pm 0.11\,. \tag{6.2.17}$$

The extracted values are different between the polynomial background fit and the combinatorial background. Considering the two methods as independent form each other, this can be used for a rough estimate of a systematic error. Taking the difference between Equation (6.2.5) and (6.2.14) (Equation (6.2.7) and (6.2.15)), the systematic error of the J/ψ mass (width) can be estimated to $\approx$ 2% ($\approx$ 27%). Note that, that due to the very limited statistics, a rigorous treatment of systematic errors is difficult. More detailed studies have to be performed in future.

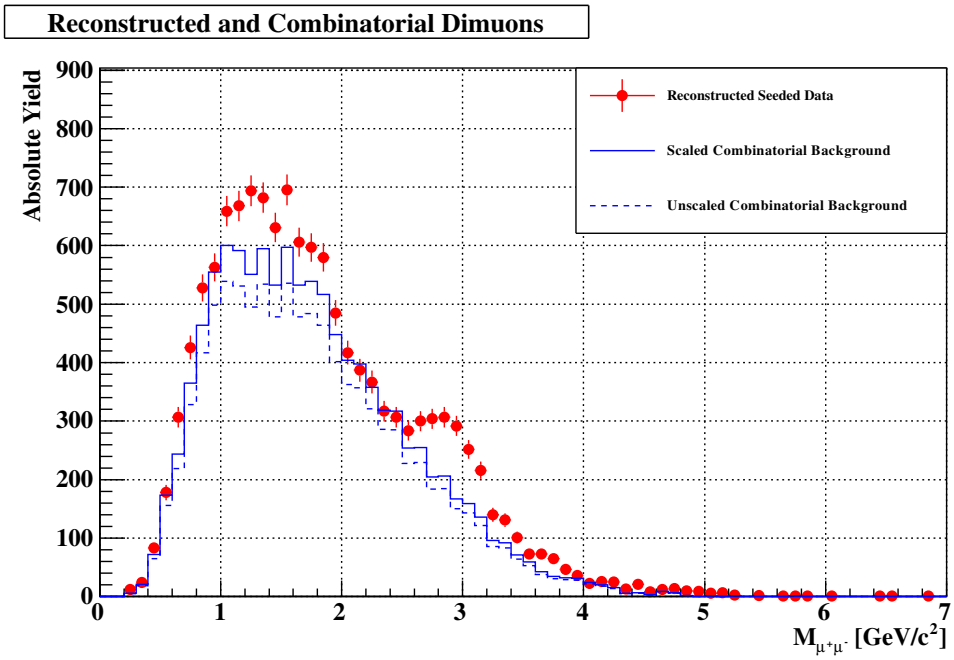

Figure 6.9: Invariant mass spectrum obtained with the seeded sample. The dashed blue line shows the combinatorial background estimation before scaling, the solid blue line after matching the number of events in the range $[1.9\,\mathrm{GeV/c^2}, 2.4\,\mathrm{GeV/c^2}]$.

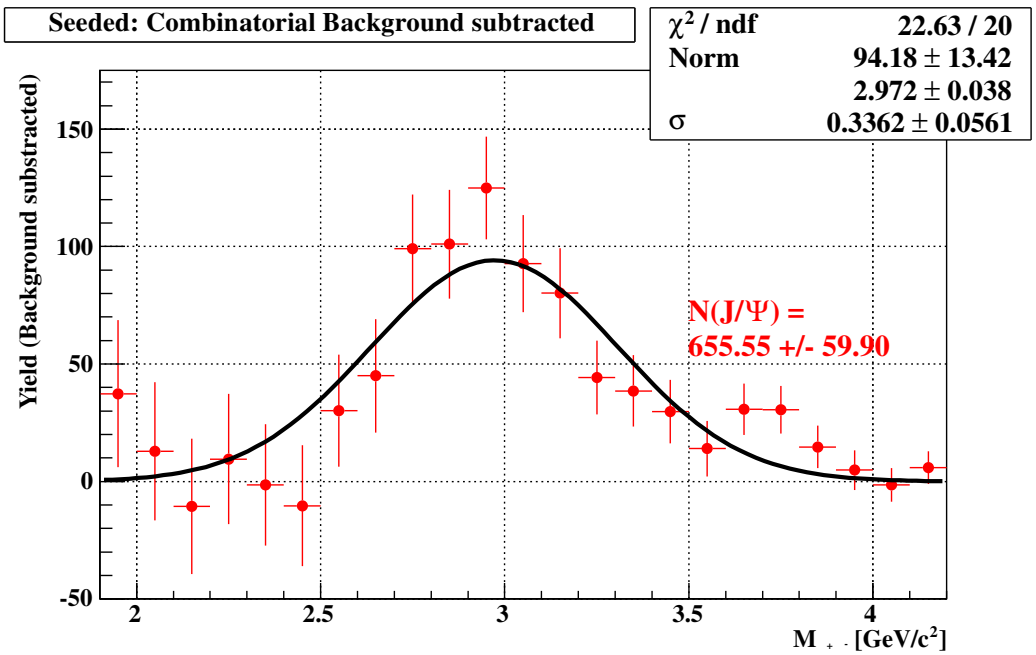

Figure 6.10: Invariant mass spectrum for the seeded sample corrected for combinatorial background. The J/ψ-mass is estimated with a single Gaussian. The number of reconstructed J/ψ's is estimated via a numerical integration in the range $[2.7\,\mathrm{GeV/c^2}, 3.2\,\mathrm{GeV/c^2}]$.

6.3 Background Corrected Distributions

In this Section we present kinematic and spatial distributions of the reconstructed J/ψs. For this purpose, two estimation methods are introduced and used. The first method uses a background estimation based on the combinatorial event-mixing model. This allows us to estimate and compare the signal J/ψ dimuons (=background subtracted) with background dimuons.

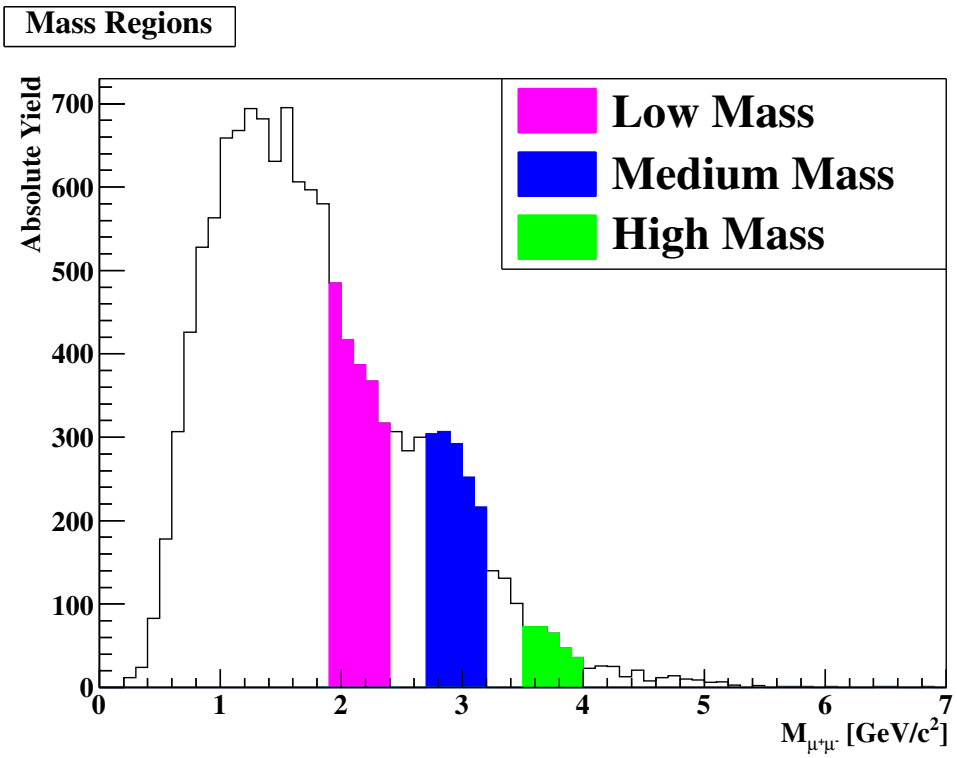

Figure 6.11: The definitions of the low, medium and high mass regions. The corresponding distributions were used to generate a best-guess estimate for the J/ψ signal distributions.

We also introduce a second method to estimate the various J/ψ distributions of the reconstructed data. For this we define the following three mass regions

$$\text{Low Mass B1}: \quad [1.9\,\text{GeV/c}^2, 2.4\,\text{GeV/c}^2], \tag{6.3.1}$$

$$\text{Medium Mass S}: \quad [2.7\,\text{GeV/c}^2, 3.2\,\text{GeV/c}^2], \tag{6.3.2}$$

$$\text{High Mass B2}: \quad [3.5\,\text{GeV/c}^2, 4.0\,\text{GeV/c}^2]. \tag{6.3.3}$$

For the background estimate we take the average of $B1$ and $B2$ as $\frac{B1+B2}{2}$. This approximation only holds if the background decreases linearly with the dimuon mass. The mass spectrum of the combinatorial background in Figure 6.9 suggests

that this linearity holds for the mass region $[1.4\,\mathrm{GeV/c^2}, 4.0\,\mathrm{GeV/c^2}]$. Then the J/ψ-signal is obtained by subtracting the average from S.

The resulting J/ψ dimuons are expected to have different distributions as those arising from (accidental or random) background. The reconstructed J/ψ-distributions are compared to distributions obtained from a GEANT4 based $pFe \rightarrow J/\psi$ Monte Carlo. The Monte Carlo distributions were normalized to match the integrals of the reconstructed J/ψ-distributions.

Figure 6.12 (6.13) shows an overview of the momentum-, transverse momentum and vertex-distributions obtained from the first (second) method. The following observations can be made:

- **p-distributions:** The J/ψ momentum distributions are very similar for both methods. The peak is located at $\approx 75\,\mathrm{GeV/c}$, the distribution falls steeply to zero between $\approx 80\,\mathrm{GeV/c}$ and $\approx 90\,\mathrm{GeV/c}$. The momentum distributions match well with the MC predictions. For the first method the peak for both the combinatorial background and the J/ψ is located at $\approx 85\,\mathrm{GeV/c}$. However, for the second method, the background distributions peak at $\approx, 100\,\mathrm{GeV/c}$.

- **pT-distributions:** The peak of the transverse momentum distributions is located between $\approx 0.5\,\mathrm{GeV/c}$ and $\approx 1.0\,\mathrm{GeV/c}$ for both methods. In contrast to the momentum distributions the pT-distributions' peak positions don't seem to differ very much from the signal J/ψs and the various background estimates. The monotonously decreasing trend of the MC distributions can be reproduced by the measured distributions.

- **Vertex-distributions:** For both methods the reconstructed J/ψs originate from the inside FMAG iron. The peak positions at $\approx 30\,\mathrm{cm}$ match very well with the MC predictions. Accordingly, the vertex-hypothesis of the trigger is confirmed by the reconstructed vertex distributions of the J/ψs. The shape for the vertex distributions of the combinatorial background is a lot wider compared to the J/ψs, whereas the peak positions are unchanged.

In summary, it can be stated that both the first and the second method produce similar momentum, transverse momentum and vertex distributions. Given the low statistics of the measurement, the agreement with Monte Carlo is reasonably good. Thus, it is shown that the dimuons from J/ψ decays behave as expected. The combinatorial background estimates have very distinct distributions from the signal J/ψs.

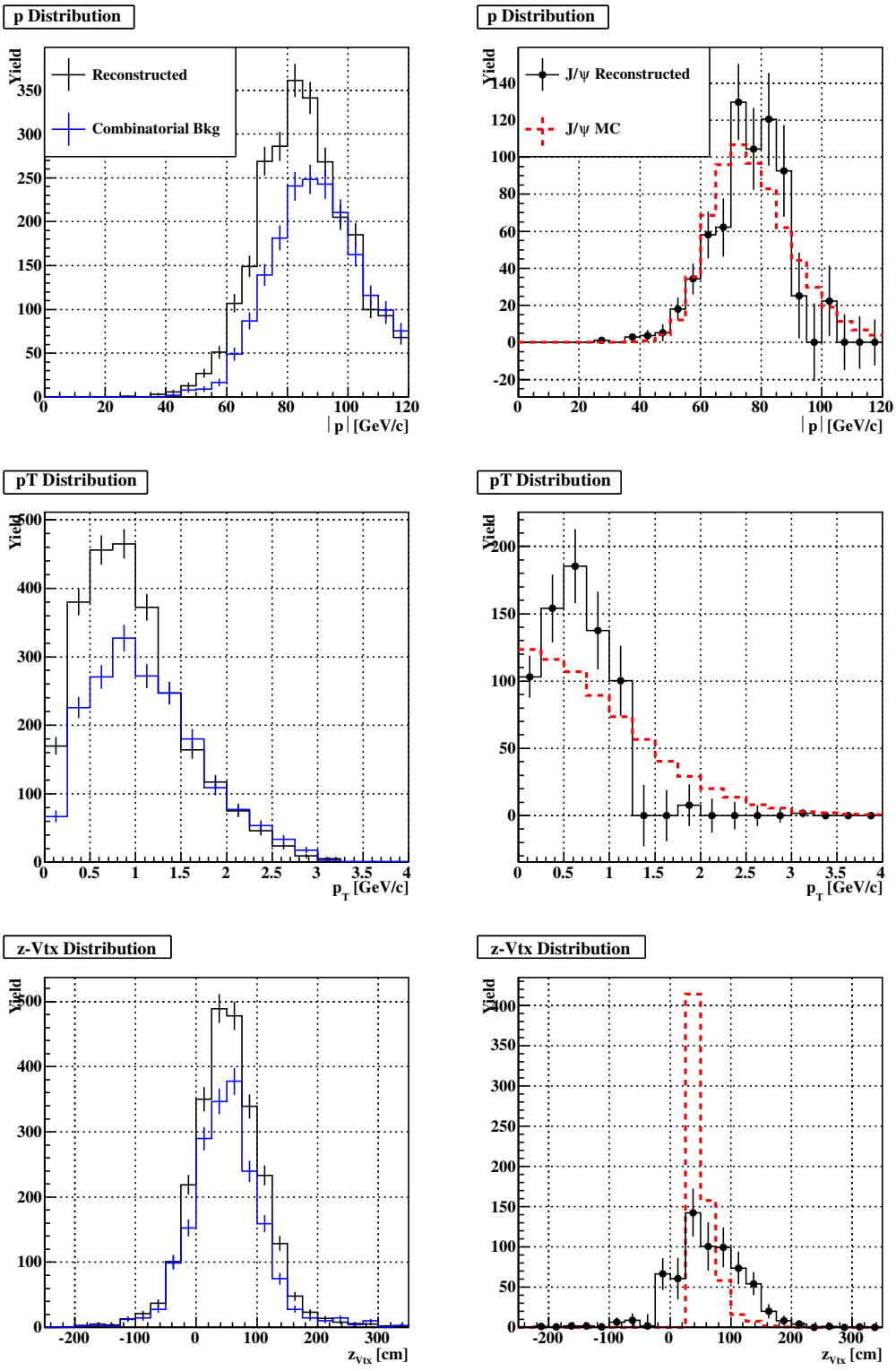

Figure 6.12: J/ψ observables obtained by the first method (details see text). The left column shows the momentum-, transverse momentum and vertex-distributions for reconstructed dimouns (black line) and the combinatorial background (blue line) in the mass range $[2.4\,\mathrm{GeV/c^2}, 3.4\,\mathrm{GeV/c^2}]$. The right column shows the extracted J/ψ-signal (black line). The dashed red line shows a J/ψ Monte Carlo comparison. Details can be found in the text.

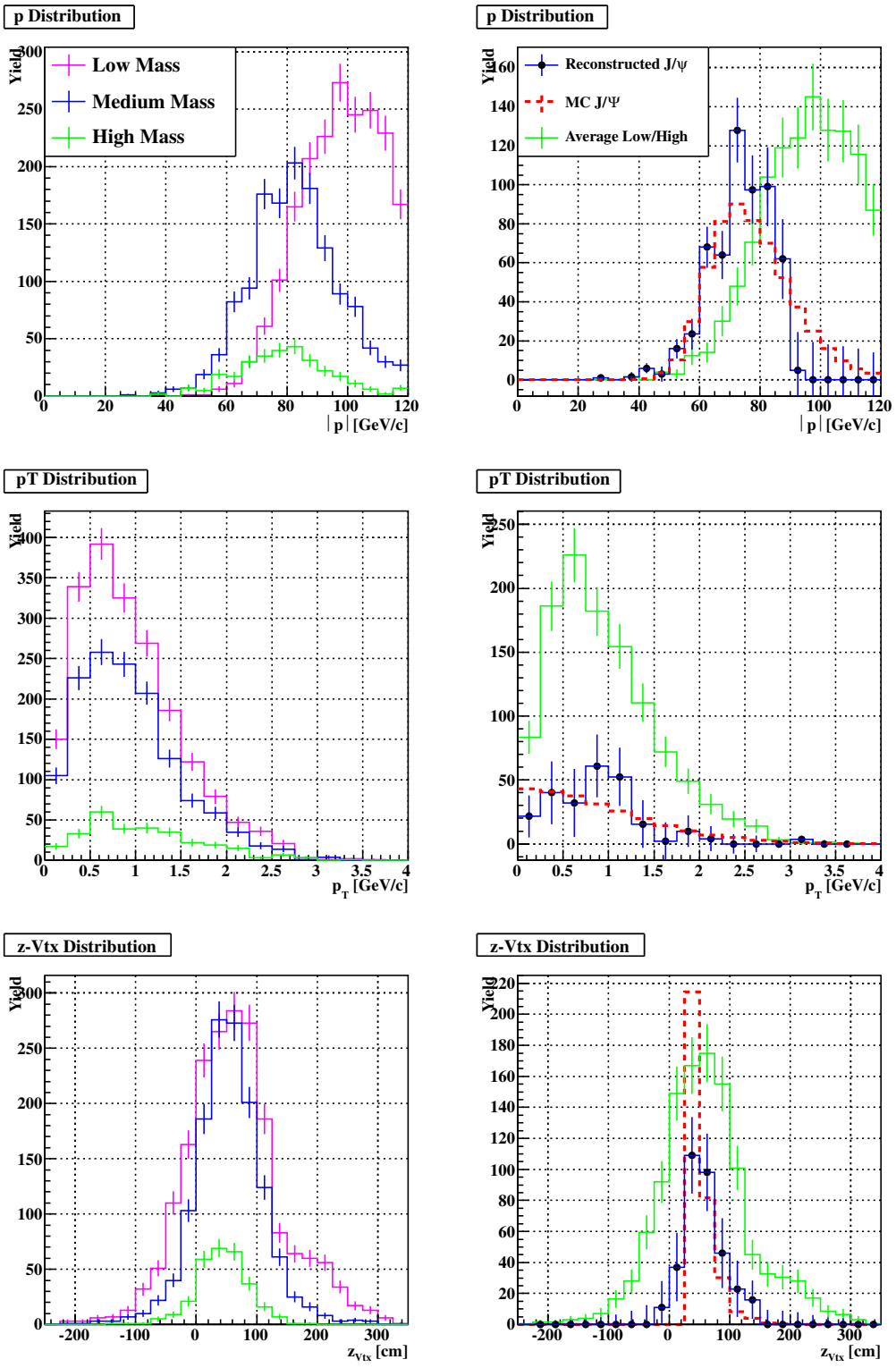

Figure 6.13: J/ψ observables obtained by the second method (details see text). The left column shows the momentum-, transverse momentum and vertex-distributions for different mass regions. The right column shows the average of the high mass and low mass (green line), and the extracted J/ψ-signal (blue line). The dashed red line shows a J/ψ Monte Carlo comparison. Details can be found in the text.

Chapter 7

Conclusion

The SeaQuest experiment is a fixed-target experiment located at Fermi Nation Accelerator Laboratory (Fermilab). It detects Drell-Yan muon pairs from proton-proton collisions induced by a 120 GeV beam ($\sqrt{s} = 11$ GeV). A new method which allows the track reconstruction of dimuons in high multiplicity data recorded during the first commissioning run at the SeaQuest experiment is presented in this thesis.

The SeaQuest spectrometer is a forward spectrometer optimized by a focusing magnet to be particularly sensitive to high-p_T muon pairs. A large iron block is placed inside the focusing magnet to stop hadronic background. Four tracking stations are used for track reconstruction. The first three stations consist of drift chambers, and the fourth station consists of drift tubes. Hodoscope arrays in each tracking station trigger di-muon events. A separate analyzing magnet measures the momenta of muons.

The Drell-Yan process occurs in high-energetic hadron collisions when a quark of one hadron and an antiquark of another hadron annihilate, creating a virtual photon, which then decays into a pair of oppositely charged muons. The dimuon kinematics are directly related to the antiquarks in the proton.

In spring 2012, the first 120 GeV proton beam was successfully extracted from the Fermilab Main Injector Ring to the fixed target beamline of SeaQuest. The average intensity of the protons during the 6 weeks of commissioning run was 7×10^{11} per spill.

The conclusions of this thesis are listed as follows:

- During the commissioning of the SeaQuest spectrometer the beam from the accelerator had a very irregular time structure. Very high drift chamber occupancies were the consequence which made track reconstruction difficult.

- In order to deal with the high occupancies, sophisticated methods for track reconstruction were developed. An innovative track finding algorithm, called `fTrkSeeder` was developed

- `fTrkseeder` is based on a global track model at SeaQuest. Global means a track model which takes correlation of drift chamber hits from the different tracking stations into account. It thus can be called a global track model.

- The track model is represented by a 72×72-correlation matrix. The matrix provides correlation parameters including its uncertainties. Combing this matrix with an intelligent track candidate formation, it has a very powerful tool to identify tracks in a high occupancy environment. Based on Monte-Carlo studies, the di-muon detection efficiencies are above 98 %. By only considering hits which belong to a track candidate, the average drift chamber occupancies could be decreased to 5 %.

- My track finder algorithm was combined with the track fitter at SeaQuest. With the combination of track finder and track fitter, the yield of reconstructed J/Ψ's could was increased by a factor of 2.4.

- The reconstructed J/Ψ-mass was $M(J/\psi) = (2.938 \pm 0.020)\,\mathrm{GeV/c^2}$, its width was $\sigma(J/\psi) = (0.205 \pm 0.019)\,\mathrm{GeV/c^2}$. These values are very important observable of the commissioning run. It suggests that the SeaQuest spectrometer is operational and has a working track reconstruction software.

- The methods developed in this thesis are very useful and can be used for the upcoming physics run of the SeaQuest spectrometer commencing beginning of 2014. The methods could be used in other experiments as well.

- Based on this thesis the first evidence of dimuon kinematics recorded by the SeaQuest spectrometer is shown.

- By the 120 GeV proton beam, the SeaQuest spectrometer is capable to record more Drell-Yan events than other experiment before. 120 GeV is the ideal energy in terms of Drell-Yan corss section and in terms of comparison of data with theory. The thesis suggests that the SeaQuest spectrometer is prepared to record Drell-Yan dimuons. These Drell-Yan dimuons allow to perform the most precise measurement of the $\bar{d}/\bar{u}$ asymmetry of the nucleon sea up-to-date.

- The SeaQuest spectrometer will also be used to measure the first Drell-Yan dimuns from polarized proton-nucleon collisions. These measurements will shed new light on the mechanism of the transverse momentum dependent Boer Moelder function.

Acknowledgements

First and foremost I would like to thank my supervisor Prof. Toshi-Aki Shibata of Tokyo Tech who gave me the opportunity to write this thesis. Since he invited me to Tokyo in summer 2009 he triggered my interest in experimental particle physics. I am very grateful that he gave me the chance to work in such an international project between Tokyo and Chicago. He was a great support to me, without his advice I could have never finished this work. His advice based on his experience in deep inelastic scattering and hadron reaction was very useful.

I also want to thank Prof. Kenichi Nakano for advising me throughout this thesis. He introduced me to the alchemy of repairing and commissioning drift chambers. Also his advice concerning software development was very fruitful to me.

I would like to thank all staff members of the SeaQuest-J collaboration: Dr. Shin'ya Sawada, Dr. Yuji Goto and Dr. Yoshiyuki Miyachi. The discussions with you and your advice were indispensable for the completion of the thesis.

This work was financially supported by the Research Fellowship of the Japan Society for the Promotion of Science (JSPS) for Young Scientists. It was partially supported also by the Global-COE program of our institute in the years 2010 and 2011. During the first year of Doctor Course, I was supported by a Postgraduate-PhD fellowship by the German Academic Exchange Service (DAAD).

Special thanks goes to Dr. Lamiaa Al Fassi (Old Dominion University) who supported me in all the bad and good times of the thesis. She always succeeded in giving me hope and motivation for this work. Especially during the first two years of my Doctor Course, during the seemingly never ending restoration and setup of the drift chambers in Lab-6. Thank you so, so much, Lamiaa!

I would like to also express special thanks to Dr. Markus Diefenthaler (University of Illinois in Urbana-Champaign). Thank you for the great time on 9th floor in Wilson Hall, which was full of stimulating discussions about both physics and everything beyond physics. It was great to share my concerns, hopes, frustrations, thoughts of any kind and Turbojugend moments with you!

I would like to express my gratitude to Dr. Paul Reimer and Dr. Donald Geesaman, the two spokes-persons of the SeaQuest collaboration. Thank you for all the support and your efforts to make this experiment happen. I want to thank Dr. David Christian for introducing me to the details of chamber read-out electronics. Also the idea about `fTrkSeeder` is based on discussions with Dave. Finally, I want to thank Dr. Charles Brown. I was amazed by his profound knowledge of physics and his profound hands-on experience on all kinds of hardware or physics related problems.

I want to thank Tom O'Connor and Kevin Bailey for technical drawings of the SeaQuest spectrometer. It was always great to work with you.

I want to thank Dr. Kazutaka Nakahara, Arun Tadepalli, Bryan Kerns, Bryan Dannowitz, Evan McClellan and Wen-Chen Chang. It was a fun time with you and it was great to collaborate with you at Fermilab.

I also want to express my gratitude to Dr. Kun Liu (Los Alamos National Laboratory) and Dr. Joshua Rubin (University of Michigan). Thank you for the inspiring discussions at the the track seeder workshop in February 2013. Special and great thanks to you, Josh, for providing the `sqerp` reconstruction program and helping me with the details of the code.

I want to thank all members of Shibata-lab who joined my way. I want to thank Noriaki Kobayashi, Yuki Kobayashi, Shunsuke Masuike, Shintaro Takeuchi, Osamu Okamura, Kei Nagai and Shigeki Obata for useful discussions. It was a joyful time together with you fellows!

Dr. Yoshi-mitsu Imazu and Dr. Hideyuki Takei were a very great help for me. First, they introduced me to the Tokyo Tech environment in summer 2009. Second, they supported me with a lot of useful advice for my Doctor Course.

I want to particularly thank Shou Miyasaka for the great time together. It was a great experience and time to share a house in Chicago together. Besides, our white board sessions were so incredibly fruitful to tackle down tough physics problems. I cannot imagine solving a problem without a white board anymore. Shou, thanks for being my friend!

In addition I want to thank all the people making life outside physics in Chicago and Tokyo enjoyable!

The last three years were not always easy for me. I had to manage a life between two foreign countries, I experienced one of the biggest earthquakes recorded in history, started as a Doctor Course student, when the SeaQuest detector was in a preparation stage. I would not have gone all the long way if there wouldn't have

been continuous support and encouragement by my parents. I want to express my deepest gratitude to them for always supporting me during my studies and my life. They gave me power during all up's and down's of my graduate studies. Thank you so much for letting me go abroad and supporting my global life.

Appendix A

Appendix

A.1 Vertex Distribution

For the analysis shown in this thesis, the used reaction were mostly from the beam dump which is an iron block in the first magnet. For future measurements of cross section with the SeaQuest spectrometer (e.g. to obtain $\bar{d}(x)/\bar{u}(x)$), the z-Vertex resolution is essential. It is important to differentiate the origin of the di-muon and to estimate if the muon pair was created in the target flask or in the beam bump of the FMAG iron. The vertex resolution is sensitive to the invariant mass of the di-muon. The resolution is improving with wider opening angles θ of the muon pair. Since the major measurements of SeaQuest will focus on Drell-Yan muons in the future, an invariant mass cut of roughly $M_{\mu^+\mu^-} \approx 3\,\mathrm{GeV/c^2}$ is going to be used.

Thus, it is interesting to check the vertex distribution of muon pairs based on the SeaQuest commissioning data (see dashed lines in Figure A.1). For the data sets which were included in this analysis, the di-muon trigger was used. The matrix roads used by the di-muon trigger were generated by Monte-Carlo J/ψ events originating from the dump ($z = 0\,\mathrm{cm}$). Figure A.1 suggests that for di-muon mass outside the J/ψ mass region mostly originated from the dump face around $z = 48\,\mathrm{cm} \pm 48\,\mathrm{cm}$. Accordingly, the vertex-hypothesis of the trigger is confirmed by the reconstructed vertex distributions. The shape for the vertex distributions of the default data set and the seeded data set are very similar.

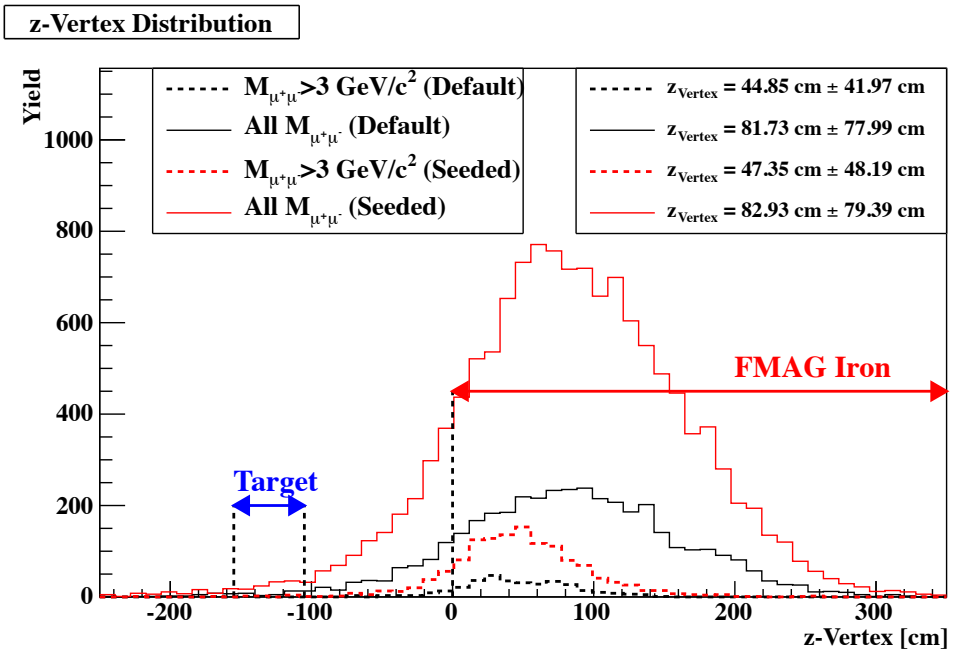

Figure A.1: z-Vertex distribution of reconstructed muon pairs. The distributions for both the seeded (red lines) and default data sample (black line) are shown. The ashed lines represent di-muons excluding the J/ψ mass region.

Bibliography

[1] J. D. Bjorken. Asymptotic Sum Rules at Infinite Momentum. *Phys. Rev.*, 179:1547–1553, 1969.

[2] J. D. Bjorken and Emmanuel A. Paschos. Inelastic Electron Proton and gamma Proton Scattering, and the Structure of the Nucleon. *Phys. Rev.*, 185:1975–1982, 1969.

[3] Richard P. Feynman. Very high-energy collisions of hadrons. *Phys. Rev. Lett.*, 23:1415–1417, 1969.

[4] Murray Gell-Mann. A Schematic Model of Baryons and Mesons. *Phys. Lett.*, 8:214–215, 1964.

[5] D. P. Barber et al. Discovery of Three Jet Events and a Test of Quantum Chromodynamics at PETRA Energies. *Phys. Rev. Lett.*, 43:830, 1979.

[6] J. Christenson, G. Hicks, L. Lederman, P. Limon, B. Pope, and E. Zavattini. Observation of massive muon pairs in hadron collisions. *Physical Review Letters*, 25(21):1523–1526, Nov 1970.

[7] J. Christenson, G. Hicks, L. Lederman, P. Limon, B. Pope, and E. Zavattini. Observation of muon pairs in high-energy hadron collisions. *Physical Review D*, 8(7):2016–2034, Oct 1973.

[8] Sidney Drell and Tung-Mow Yan. Massive lepton-pair production in hadron-hadron collisions at high energies. *Physical Review Letters*, 25(5):316–320, Aug 1970.

[9] R. Towell, P. McGaughey, T. Awes, M. Beddo, M. Brooks, C. Brown, J. Bush, T. Carey, T. Chang, W. Cooper, and et al. Improved measurement of the $\bar{d}/\bar{u}$ asymmetry in the nucleon sea. *Physical Review D*, 64(5), Aug 2001.

[10] A. Baldit, C. Barrire, J. Castor, T. Chambon, A. Devaux, B. Espagnon, J. Fargeix, P. Force, G. Landaud, P. Saturnini, and et al. Study of the isospin symmetry breaking in the light quark sea of the nucleon from the drell-yan process. *Physics Letters B*, 332(1-2):244–250, Jul 1994.

[11] Jonathan Pumplin, Daniel Robert Stump, Joey Huston, Hung-Liang Lai, Pavel Nadolsky, and Wu-Ki Tung. New generation of parton distributions with uncertainties from global qcd analysis. *Journal of High Energy Physics*, 2002(07):012–012, Jul 2002.

[12] H. L. Lai, J. Huston, S. Kuhlmann, F. Olness, J. Owens, D. Soper, W. K. Tung, and H. Weerts. Improved parton distributions from global analysis of recent deep inelastic scattering and inclusive jet data. *Physical Review D*, 55(3):1280–1296, Feb 1997.

[13] A.D Martin, R.G Roberts, and W.J Stirling. Parton distributions: a study of the new hera data, α_s, the gluon and $p\bar{p}$ jet production. *Physics Letters B*, 387(2):419–426, Oct 1996.

[14] A.D. Martin, R.G. Roberts, W.J. Stirling, and R.S. Thorne. Uncertainties of predictions from parton distributions i: Experimental errors. *The European Physical Journal C - Particles and Fields*, 28(4):455–473, Jun 2003.

[15] A. D. Martin, R. G. Roberts, W. J. Stirling, and R. S. Thorne. Uncertainties of predictions from parton distributions ii: theoretical errors. *The European Physical Journal C*, 35(3):325–348, Jun 2004.

[16] M. Glück, E. Reya, and A. Vogt. Dynamical parton distributions revisited. *The European Physical Journal C*, 5(3):461–470, Sep 1998.

[17] P. Amaudruz, M. Arneodo, A. Ardivson, B. Badelek, G. Baum, J. Beaufays, I.G. Bird, M. Botje, C. Broggini, W. Brückner, and et al. The ratio f2n/f2p in deep inelastic muon scattering. *Nuclear Physics B*, 371(1-2):3–31, Mar 1992.

[18] M. Arneodo, A. Arvidson, B. Badelek, M. Ballintijn, G. Baum, J. Beaufays, I. Bird, P. Björkholm, M. Botje, C. Broggini, and et al. Reevaluation of the gottfried sum. *Physical Review D*, 50(1):R1–R3, Jul 1994.

[19] E. Hawker, T. Awes, M. Beddo, C. Brown, J. Bush, T. Carey, T. Chang, W. Cooper, C. Gagliardi, G. Garvey, and et al. Measurement of the light

antiquark flavor asymmetry in the nucleon sea. *Physical Review Letters*, 80(17):3715–3718, Apr 1998.

[20] A. D. Martin, R. G. Roberts, W. J. Stirling, and R. S. Thorne. Parton distributions incorporating qed contributions. *The European Physical Journal C*, 39(2):155–161, Feb 2005.

[21] M. E. Peskin and D. V. Schroeder. *An Introduction to Quantum Field Theory*. Westview Press, 1995.

[22] F. Halzen and A. D. Martin. *Quarks and Leptons: An Introductory Course in Modern Particle Physics*. John Wiley & Sons, 1984.

[23] A. V. Manohar. An Introduction to Spin Dependent Deep Inelastic Scattering. *arXiv:hep-ph/9204208v1*, 1992.

[24] M. Anselmino, A. Efremov, and E. Leader. The theory and phenomenology of polarized deep inelastic scattering. *Phys. Rept.*, 261:1–124, 1995.

[25] D. Gabbert. *Determination of the structure function F2 at Hermes*. PhD thesis, Universität Hamburg, 2008.

[26] A. Airapetian et al. Precise determination of the spin structure function g(1) of the proton, deuteron and neutron. *Phys. Rev.*, D75:012007, 2007.

[27] C. G. Callan and D. J. Gross. High-energy electroproduction and the constitution of the electric current. *Phys. Rev. Lett.*, 22:156–159, 1969.

[28] Y. L. Dokshitzer. Calculation of the Structure Functions for Deep Inelastic Scattering and e+ e- Annihilation by Perturbation Theory in Quantum Chromodynamics. *Sov. Phys. JETP*, 46:641–653, 1977.

[29] V. N. Gribov and L. N. Lipatov. e+ e- pair annihilation and deep inelastic e p scattering in perturbation theory. *Sov. J. Nucl. Phys.*, 15:675–684, 1972.

[30] L. N. Lipatov. The parton model and perturbation theory. *Sov. J. Nucl. Phys.*, 20:94–102, 1975.

[31] Guido Altarelli and G. Parisi. Asymptotic Freedom in Parton Language. *Nucl. Phys.*, B126:298, 1977.

[32] A. D. Martin, W. J. Stirling, R. S. Thorne, and G. Watt. Parton distributions for the LHC. *The European Physical Journal C*, 63(2):189–285, Sep 2009.

[33] Kurt Gottfried. Sum rule for high-energy electron-proton scattering. *Physical Review Letters*, 18(25):1174–1177, Jun 1967.

[34] M. Adams, S. Aid, P. Anthony, D. Averill, M. Baker, B. Baller, A. Banerjee, A. Bhatti, U. Bratzler, H. Braun, and et al. Extraction of the ratio f2n/f2p from muon-deuteron and muon-proton scattering at small x and q2. *Physical Review Letters*, 75(8):1466–1470, Aug 1995.

[35] J. Zhao, R. Abegg, A. Berdoz, J. Birchall, J. Campbell, C. Davis, P. Delheij, L. Gan, P. Green, L. Greeniaus, and et al. Precision measurement of charge symmetry breaking in np elastic scattering at 347 MeV. *Physical Review C*, 57(5):2126–2141, May 1998.

[36] G.A. Miller, B.M.K. Nefkens, and I. Slaus. Charge symmetry, quarks and mesons. *Physics Reports*, 194(1-2):1–116, Oct 1990.

[37] Paul Reimer (Fermilab E866/NuSea). Unpublished, 2007.

[38] J. Kubar, M. Le Bellac, J.L. Meunier, and G. Plaut. Qcd corrections to the drell-yan mechanism and the pion structure function. *Nuclear Physics B*, 175(2):251 – 275, 1980.

[39] I R Kenyon. The drell-yan process. *Reports on Progress in Physics*, 45(11):1261–1315, Nov 1982.

[40] W J Stirling and M R Whalley. A compilation of drell-yan cross sections. *Journal of Physics G: Nuclear and Particle Physics*, 19(D):D1–D102, Dec 1993.

[41] John Collins and Davison Soper. Angular distribution of dileptons in high-energy hadron collisions. *Physical Review D*, 16(7):2219–2225, Oct 1977.

[42] G. Altarelli, R.K. Ellis, and G. Martinelli. Large perturbative corrections to the drell-yan process in qcd. *Nuclear Physics B*, 157(3):461–497, Oct 1979.

[43] W.L. van Neerven and E.B. Zijlstra. The o(α^2) corrected drell-yan k-factor in the dis and schemes. *Nuclear Physics B*, 382(1):11–62, Aug 1992.

[44] J. C. Peng, G. T. Garvey, T. C. Awes, M. E. Beddo, M. L. Brooks, C. N. Brown, J. D. Bush, T. A. Carey, T. H. Chang, W. E. Cooper, and et al. $\bar{d}/\bar{u}$ asymmetry and the origin of the nucleon sea. *Physical Review D*, 58(9), Nov 1998.

[45] A.D. Martin, W.J. Stirling, and R.G. Roberts. Parton distributions, the gottfried sum rule and the w charge asymmetry. *Physics Letters B*, 252(4):653–656, Dec 1990.

[46] R. Field and R. Feynman. Quark elastic scattering as a source of high-transverse-momentum mesons. *Physical Review D*, 15(9):2590–2616, May 1977.

[47] D.A. Ross and C.T. Sachrajda. Flavour symmetry breaking in antiquark distributions. *Nuclear Physics B*, 149(3):497–516, Mar 1979.

[48] F. Steffens and A. Thomas. Flavor asymmetry of the nucleon sea. *Physical Review C*, 55(2):900–908, Feb 1997.

[49] W. Melnitchouk, J. Speth, and A. Thomas. Dynamics of light antiquarks in the proton. *Physical Review D*, 59(1), Dec 1998.

[50] K. Ackerstaff, A. Airapetian, N. Akopov, I. Akushevich, M. Amarian, E. Ashenauer, H. Avakian, R. Avakian, A. Avetissian, B. Bains, and et al. Flavor asymmetry of the light quark sea from semi-inclusive deep-inelastic scattering. *Physical Review Letters*, 81(25):5519–5523, Dec 1998.

[51] S. Kumano. Effects of πnn form factor on pionic contributions to $\bar{d} - \bar{u}$ distribution in the nucleon. *Physical Review D*, 43(9):3067–3070, May 1991.

[52] Estia Eichten, Ian Hinchliffe, and Chris Quigg. Flavor asymmetry in the light-quark sea of the nucleon. *Physical Review D*, 45(7):2269–2275, Apr 1992.

[53] Antoni Szczurek, Alfons J Buchmann, and Amand Faessler. On the flavour structure of the constituent quark. *Journal of Physics G: Nuclear and Particle Physics*, 22(12):1741–1750, Dec 1996.

[54] A.E. DOROKHOV and N.I. KOCHELEV. Instantons AND EMC-effect for spin-dependent function. *Modern Physics Letters A*, 05(01):55–60, Jan 1990.

[55] A.E. Dorokhov and N.I. Kochelev. Instanton-induced asymmetric quark configurations in the nucleon and parton sum rules. *Physics Letters B*, 304(1-2):167–175, Apr 1993.

[56] Paul Geiger. Strange hadronic loops of the proton: A quark model calculation. *Physical Review D*, 55(1):299–310, Jan 1997.

[57] S. Kumano. Nucleon structure with pion clouds in a flux-tube quark model. *Physical Review D*, 41(1):195–202, Jan 1990.

[58] A.D. Martin, R.G. Roberts, W.J. Stirling, and R.S. Thorne. Mrst2001: partons and α_s from precise deep inelastic scattering and tevatron jet data. *The European Physical Journal C - Particles and Fields*, 23(1):73–87, Mar 2002.

[59] Y. Miyachi. Private communication. 2013.

[60] M Guanziroli et al. (NA10). *Z. Phys.*, C37:545, 1988.

[61] S Falciano et al. (NA10). *Z. Phys.*, C31:513, 1986.

[62] J. Conway, C. Adolphsen, J. Alexander, K. Anderson, J. Heinrich, J. Pilcher, A. Possoz, E. Rosenberg, C. Biino, J. Greenhalgh, and et al. Experimental study of muon pairs produced by 252-GeV pions on tungsten. *Physical Review D*, 39(1):92–122, Jan 1989.

[63] L. Zhu, J. Peng, P. Reimer, T. Awes, M. Brooks, C. Brown, J. Bush, T. Carey, T. Chang, W. Cooper, and et al. Measurement of angular distributions of drell-yan dimuons in p+d interactions at 800gev/c. *Physical Review Letters*, 99(8), Aug 2007.

[64] K. Gottfried and J. D. Jackson. On the connection between production mechanism and decay of resonances at high energies. *Il Nuovo Cimento*, 33(2):309–330, Jul 1964.

[65] C. Lam and Wu-Ki Tung. Parton-model relation without quantum-chromodynamic modifications in lepton pair production. *Physical Review D*, 21(9):2712–2715, May 1980.

[66] K. Nakano. Expected accuracy on angular distributions with e906/seaquest data. SEAQUEST-doc-832-v1, 2013.

[67] Daniel Boer. Investigating the origins of transverse spin asymmetries at bnl rhic. *Physical Review D*, 60(1), Jun 1999.

[68] Daniel Boer and P. J. Mulders. Time-reversal odd distribution functions in leptoproduction. *Phys. Rev.*, D57:5780–5786, 1998.

[69] John C. Collins. Fragmentation of transversely polarized quarks probed in transverse momentum distributions. *Nucl. Phys.*, B396:161–182, 1993.

[70] Zhun Lu and Bo-Qiang Ma. Azimuthal asymmetry in unpolarized drell-yan process. *Physics Letters B*, 615(3-4):200–206, Jun 2005.

[71] Tom O'Connor. Private Communication.

[72] J. Beringer, J. F. Arguin, R. M. Barnett, K. Copic, O. Dahl, D. E. Groom, C. J. Lin, J. Lys, H. Murayama, C. G. Wohl, and et al. Review of particle physics. *Physical Review D*, 86(1), Jul 2012.

[73] Rob Veenhof. Garfield - simulation of gaseous detectors. http://garfield.web.cern.ch/garfield/.

[74] Jefferson Lab Data Acquisition Group. The coda data acuisition system. http://coda.jlab.org.

[75] Experimental Physics and Industrial Control System. http://www.aps.anl.gov/epics.

[76] ROOT A Data Analysis Framework. http://root.cern.ch/.

[77] The VME bus (VERSAModule Eurocard) architecture. http://www.caen.it/csite/CaenProd.jsp?parent=11&idmod=705.

[78] W.M. Bokhari, J.G. Heinrich, N.S. Lockyer, and F.M. Newcomer. *The ASDQ ASIC [Central Outer Tracker CDF upgrade application]*, pages 445–446. Institute of Electrical and Electronics Engineers, 1998.

[79] K. Nakano. Chamber performance requirement. SEAQUEST-doc-827-v1, 2013.

[80] D. Geesaman. Simple analysis of resolution. SEAQUEST-doc-90-v1, 2008.

[81] S. Agostinelli, J. Allison, K. Amako, J. Apostolakis, H. Araujo, P. Arce, M. Asai, D. Axen, S. Banerjee, G. Barrand, and et al. Geant4 - a simulation toolkit. *Nuclear Instruments and Methods in Physics Research Section A: Accelerators, Spectrometers, Detectors and Associated Equipment*, 506(3):250–303, Jul 2003.